2007-12-21

# Sound Transmission Through A Fluctuating Ocean: A Modal Approach

Ilya A. Udovydchenkov
*University of Miami*, iudovydchenkov@rsmas.miami.edu

UNIVERSITY OF MIAMI

# SOUND TRANSMISSION THROUGH A FLUCTUATING OCEAN: A MODAL APPROACH

By

Ilya A. Udovydchenkov

A DISSERTATION

Submitted to the Faculty
of the University of Miami
in partial fulfillment of the requirements for
the degree of Doctor of Philosophy

Coral Gables, Florida

December 2007

UNIVERSITY OF MIAMI

A dissertation submitted in partial fulfillment of
the requirements for the degree of
Doctor of Philosophy

# SOUND TRANSMISSION THROUGH A FLUCTUATING OCEAN: A MODAL APPROACH

Ilya A Udovydchenkov

Approved:

| | |
|---|---|
| Dr. Michael G. Brown<br>Professor of Applied Marine Physics | Dr. Terri A. Scandura<br>Dean of the Graduate School |
| Dr. Francisco J. Beron-Vera<br>Assistant Scientist | Dr. Thomas R. Hahn<br>Professor of Applied Marine Physics |
| Dr. Harry A. DeFerrari<br>Professor of Applied Marine Physics | Dr. Huseyin Koçak<br>Professor of Computer Science and Mathematics |

UDOVYDCHENKOV, ILYA A. (Ph.D., Applied Marine Physics)
Sound transmission through a fluctuating ocean: a modal approach (December 2007)

Abstract of a dissertation at the University of Miami.

Dissertation supervised by Professor Michael Brown.
No. of pages in text. (138)

Sound transmission through a fluctuating deep ocean environment is considered. It is assumed that the environment consists of a range-independent background, on which a small-scale perturbation, due for example to internal waves, is superimposed. The modal description of underwater sound propagation is used extensively. The temporal spread of modal group arrivals in weakly range-dependent deep ocean environments is considered. The phrase "modal group arrival" refers to the contribution to a transient wavefield corresponding to a fixed mode number. It is shown that there are three contributions to modal group time spreads which combine approximately in quadrature. These are the reciprocal bandwidth, a deterministic dispersive contribution, and a scattering-induced contribution. The latter two contributions are shown to be proportional to the waveguide invariant $\beta$, a property of the background sound speed profile. The results presented are based mostly on asymptotic theory. Some extensions of the asymptotic modal theory are developed. These theoretical results are shown to agree well with full-wave numerical wavefield simulations and available exact mode theoretical results. Theoretical predictions of modal group time spreads are compared to estimates derived from data that was collected during the 2004 LOAPEX experiment. The effects of deficiencies in the receiving array on estimates of modal group time spreads are discussed. It is shown that in spite of array

deficiencies in the LOAPEX measurements it is possible to estimate modal group time spreads for almost all propagating modes and these estimates agree well with results obtained from numerical simulations and the developed theory. The effect of ocean internal waves on sound speed fluctuations is also considered, motivated by the observation that the amount of energy being scattered along the propagation path is sometimes greater in the experimental data than predicted by numerical simulations and theory. It is shown that the usual assumption that the potential sound speed gradient is proportional to the squared buoyancy frequency is often not a good approximation.

# Acknowledgments

This study was carried out under the supervision of Prof. Michael G. Brown. Deep appreciation is expressed to him for his kind help, great care, valuable assistance, advice, and encouragement during the time of my doctoral work. He provided an excellent scientific guidance for my dissertation research, countless opportunities to interact with other researchers in the field, and wise directions throughout my whole study that significantly broaden my scientific views and experience.

Financial support for this research was mainly provided by ONR through the Ocean Acoustics Program, Code 321.

I would like to thank my other dissertation committee members, Dr. Francisco J. Beron-Vera, Profs. Huseyin Koçak, Thomas R. Hahn and Harry A. DeFerrari for their inputs and discussions.

I would like also to acknowledge other researchers I have had the pleasure to interact with during my doctoral work: Ms. Irina I. Rypina and Dr. Maria J. Olascoaga.

# Table of Contents

# List of Figures

# 1 Introduction

The ocean is an extremely complicated acoustic environment. Underwater acoustics, the science of sound propagation in the ocean, has been developed extensively during the last several decades. The theory now provides a general understanding and a detailed description of how sound travels in the ocean, and of the mechanisms affecting it. The quantitative connection between ocean structure and sound fluctuations has been extensively studied in the past.

In this study we focus on the use of normal mode methods. Some important milestones in the development of this theory are the following. The theory of wave propagation in layered media has been developed in the extensive investigations of Brekhovskikh [1]. A theory of propagation of elastic and electromagnetic waves is presented since the same mathematical methods may be applied in both cases. Pekeris developed the theory for a simple two-layer model of the ocean (constant sound speed water column with semi-infinite homogeneous fluid bottom) – the so-called Pekeris waveguide [2]. The idea of the method is based on the technique of separation of variables for the Helmholtz equation. The normal mode method for the solution of problems in underwater sound propagation is exact in a layered environment and a number of computer codes have been developed [3, 4, 5].

However, the real ocean environment has range dependence and there are a number of ways in which normal mode theory has been extended to apply to range-dependent problems. Pierce [6] used adiabatic invariance which assumes that there is no interchange of energy between modes and that each mode function adjusts itself to the

sound speed profile at each range. Another work on range-dependent normal modes was done by Rutherford and Hawker [7] who used an approximate separation of the wave equation to develop mode coupling coefficients to describe the redistribution of energy as the normal modes propagate in range. Thompson [8] expanded the normal modes in terms of harmonic oscillator functions and solved the wave equation for the range-dependent harmonic oscillator coefficients. Another extension of the normal mode theory to range-dependent problems is the coupled mode theory introduced by Evans [9]. The environment is divided into a number of range-independent sections to give a stepwise approximation to the range-dependent problem. The stepwise problem is solved exactly in each section and solutions are matched at the step boundaries.

A theory of acoustic propagation in a model random ocean based on statistics of normal mode amplitudes, valid in the limit of low acoustic frequency was developed by Dozier and Tappert [10]. Beginning with this work the research done on mode coupling has focused on distributions of modal amplitudes as a function of range. This dissertation focuses on mode coupling but considers, in addition to distributions of modal amplitudes, the question "What is the associated wavefield structure in depth–range or depth–range–time space?".

Over many years the conceptual picture of sound propagation through a fluctuating ocean was as follows (Fig. 1). Suppose in the deep ocean there is a certain background structure of a sound speed profile $c(z)$. Then with the presence of the acoustic source $s(t)$ the pressure field at the receiver location is $p(z, r, t)$ and the details of this pressure field are controlled by the background sound speed structure. Now, suppose there is a depth- and range-dependent small disturbance of the sound

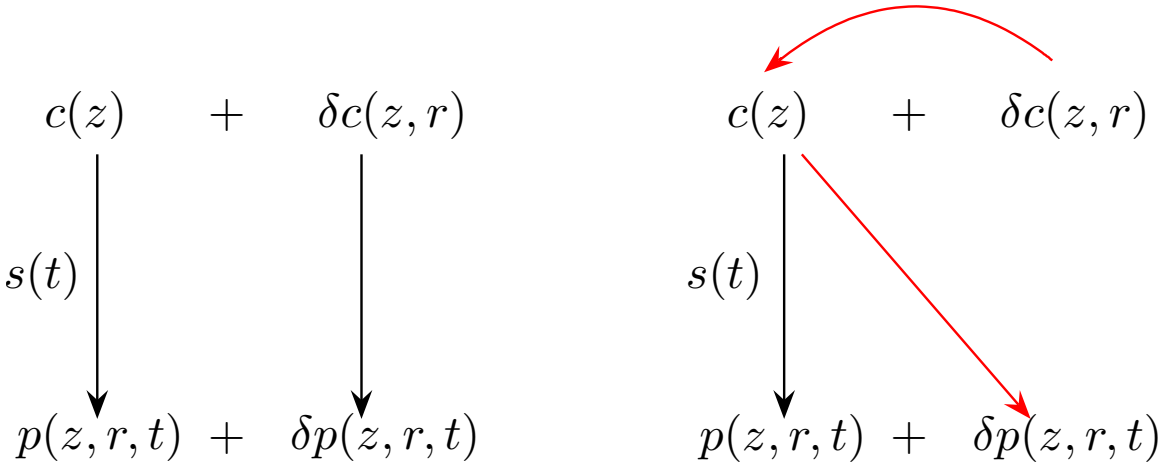


Figure 1. Conceptual picture of traditional (left) and new (right) view of sound propagation through a fluctuating ocean.

speed profile (for example due to the presence of internal waves) $\delta c\,(z,r)$, which creates in turn the disturbance of the pressure field at the receiver location $\delta p\,(z,r,t)$. Much earlier work has assumed that the details of $\delta p\,(z,r,t)$ are controlled by the details of the perturbation of the sound speed profile $\delta c\,(z,r)$. Recent theoretical work, numerical simulations and analysis of experimental data strongly suggest that this assumption is incorrect. This recent work suggests that while $\delta c\,(z,r)$ is the cause of $\delta p\,(z,r,t)$, the structure of $\delta p\,(z,r,t)$ is largely controlled by the background sound speed profile. The objective of this work is to improve our understanding of sound transmission at long-range in the deep ocean by utilizing a coupled-mode-based theoretical model and testing the predictions of such a model against recent measurements.

Another important motivation for this work is to interpret and understand measurements made during the 2004 long-range acoustic propagation experiment (LOAPEX) that was conducted in the eastern North Pacific ocean [11]. Essential elements of the

experiment are that broadband signals in the 50 Hz to 100 Hz band from a submerged compact source were transmitted to a vertical receiving array at ranges of approximately 50, 250, 500, 1000, 1600, 2300 and 3200 km. The propagation path had weak background range-dependence on which smaller scale structure, due mostly to internal waves, was superimposed. The receiving array had several deficiencies (which will be discussed in Sec. 5.2 and Sec. 5.3) but this array still allows some mode filtering to be performed. These comments suggest that a natural way to describe the wavefield and interpret the measurements is to employ a modal description that accounts for the broadband nature of the field and its range evolution in the presence of weak scattering (mode coupling). In this work we present simulated wavefields that correspond approximately to conditions during the LOAPEX experiment and test developed theoretical results. Some analysis of the LOAPEX measurements is presented and discussed.

Previously, simulation and data-based estimates of modal group time spreads for multimegameter transmissions in the eastern North Pacific Ocean have been reported in [12, 13]. In addition, Colosi and Flatté [14] have presented an extensive set of numerical simulations that were designed to investigate the influence of internal-wave-induced mode coupling on modal group time spreads. The questions that motivated their work included understanding the limitations imposed by mode coupling on acoustic tomography and matched field processing, and understanding the limitations of the adiabatic mode approximation. These issues continue to be of interest. Thus, in addition to providing a basis for interpreting the LOAPEX measurements, earlier measurements and simulations, the results presented here have implications

for aspects of broadband signal coherence and stability.

This dissertation is organized as follows. Chapter 2 reviews some traditional approaches to wave propagation in random inhomogeneous media. Chapter 3 discusses some theoretical results, including those obtained by the use of ray methods. A few important aspects of ray-mode duality are outlined in this chapter as well. Chapter 4 is devoted to the theoretical study of wavefield structure and mode coupling in the deep ocean. Dispersion diagrams are introduced and discussed in Sec. 4.3 and a method to improve the accuracy of these diagrams is derived in Sec. 4.4 of this chapter. Chapter 5 presents the analysis of the LOAPEX experimental data set, discusses effects of deficiencies in the receiving array, and reconciles the experimental data with the theory. Chapter 6 considers the quantitative connection between internal-wave-induced fluid particle displacements and sound speed fluctuations. A summary of the results and final conclusions are included in Chapter 7. Possible future work is also outlined.

# 2 Background

In this chapter different approaches to wave propagation in random inhomogeneous media that were developed over past several decades are briefly reviewed. At the beginning the simple homogeneous background problem is briefly discussed. Then some aspects of the more sophisticated $\Phi$–$\Lambda$ theory that accounts for the inhomogeneities of the background sound speed profile are presented. Also classical works on mode coupling and some recent developments on the applicability of the adiabatic approximation for modes are overviewed.

## 2.1 Traditional approaches to wave propagation in random inhomogeneous media

### 2.1.1 The homogeneous background problem

The scattering of radiation in an environment consisting of a homogeneous background on which an inhomogeneous perturbation is superimposed has been treated using both wave and ray theoretical methods in a book by Chernov [15]. This monograph contains a systematic treatment of the theory of wave propagation in a homogeneous background medium with random inhomogeneities and includes a unified general treatment of weak-scattering methods. Another treatment of the homogeneous background problem with a homogeneous isotropic perturbation can be found in the book by Tatarskii [16]. A complete treatment of the weak-scattering regime under the conditions of isotropic turbulence and some progress in the strong-scattering regime are present in this book. But this work and work by most other authors

treat only isotropic cases without specializing to the ocean environment. Their results have been widely applied in ocean acoustics, but their neglect of anisotropy, which is fundamental to the ocean environment, limits the practical utility of their results. A brief discussion of the propagation of signals in a random inhomogeneous medium with isotropic statistical properties can be found in the book by Tolstoy and Clay [17]. These authors represent the ocean as a transmission channel, and describe its properties by certain correlation coefficients that are not readily identifiable with known physical processes.

### 2.1.2 $\Phi$–$\Lambda$ theory

An important contribution to the development of the theory of sound transmission through a fluctuating ocean was made by Flatté *et al.* [18]. An important concept in this theory of sound transmission through a fluctuating ocean is the concept of a $\Lambda$, $\Phi$ space representation which is divided into several regimes; $\Lambda$ is the diffraction parameter that gives a measure of the received volume scattering, and $\Phi$ is the strength parameter that is a measure of the accumulated root mean square (rms) sound speed variations along the path of propagation. In each of these regimes, one can derive expressions for the statistics of acoustic fluctuations in terms of $\Lambda$, $\Phi$ and $D$, the phase structure function. Internal waves are assumed to be the source of sound speed fluctuations and the Garrett-Munk model [19] is used for predictions. The oceanic sound speed as a function of space and time can be expressed as

$$c\left(\mathbf{x},t\right)=c_0\left(1+u_0\left(z\right)+\mu\left(\mathbf{x},t\right)\right), \tag{1}$$

where $\mathbf{x}$ is the coordinate vector and $z$ is the vertical coordinate. The strength parameter $\Phi$ can be regarded as either the sum of rms sound speed fluctuations along the ray or as the rms variation in phase of the received signal [18] in the geometrical optics regime. It is defined as

$$\Phi^2 = k_0^2 \int_0^R dr \int_0^R dr' \rho\left(z\left(r\right), z\left(r'\right), r - r', \theta, 0\right), \tag{2}$$

where $k_0 = \sigma/c_0$ is the acoustic wavenumber (to zeroth order), $R$ is the range, $\rho\left(z\left(r\right), z\left(r'\right), r - r', \theta, \tau\right)$ is the correlation function of the sound speed fluctuations along the path of integration $z\left(r\right)$, which is also the ray path, and $\theta$ is the angle the ray makes with horizontal. The correlation function is related to the sound speed fluctuations and to the vertical displacement of water particles by

$$\rho\left(z\left(r\right), z\left(r'\right), r - r', \theta, \tau\right) = \left\langle \mu\left(z\left(r\right), r, t\right) \mu\left(z\left(r'\right), r', t + \tau\right)\right\rangle_t . \tag{3}$$

Here

$$\mu\left(z, r, t\right) = \frac{\delta c}{c} = c^{-1} \frac{\delta c_p}{\delta z} \xi\left(z, r, t\right), \tag{4}$$

where $c_p$ is the potential sound speed, $c$ is the characteristic sound speed, and $\xi$ is the vertical displacement of a fluid particle (due to internal waves, for instance). The size of a Fresnel zone for particular source–receiver geometry plays an important role in the $\Phi$–$\Lambda$ theory. The concept of a Fresnel zone in ocean sound transmission is complicated by the presence of the sound channel.

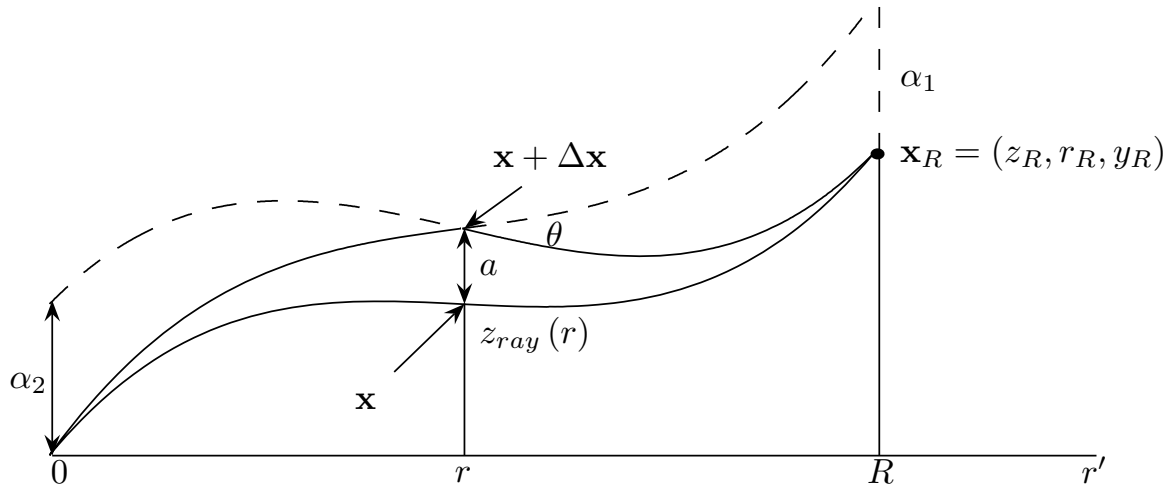


Figure 2. Geometry for defining Fresnel zones and ray tubes in the presence of a deterministic sound channel (after S. M. Flatté *et al.* [18]).

Consider a ray in the deterministic sound channel with no fluctuations from internal waves or other disturbances (Fig. 2). The acoustic path length along the ray is [18]

$$S_0(\mathbf{0},\mathbf{x}_R)=\int_0^{\mathbf{x}_R}\left\{\frac{1}{2}\left(\frac{y_R}{R}\right)^2+\frac{1}{2}\left[z'_{ray}(r)\right]^2-u_0(z)\right\}dr, \tag{5}$$

where the subscript zero indicates the path length undisturbed by fluctuations. The phase curvature, $A(r)$, is defined by

$$A(r)=\partial_{zz}\left[S_0(\mathbf{0},\mathbf{x})+S_0(\mathbf{x},\mathbf{x}_R)\right] \tag{6}$$

so that $A(r)$ is the second derivative of the path length for a small vertical displacement at a range $r$. In [17] it is argued that the radius of the first Fresnel zone $R_F$ is

$$R_F^2 = 2\pi \left(k_0 A\right)^{-1}. \tag{7}$$

Now the diffraction parameter $\Lambda$ is given by

$$\Lambda = \Phi^{-2} k_0^2 \int_0^R dr \int_0^R dr' \rho\left(z\left(r\right), z\left(r'\right), r - r', \theta, 0\right) \left|k_0 A L_v^2\right|^{-1}, \tag{8}$$

where $L_v$ is the vertical correlation length. The diffraction parameter characterizes the diffraction effect caused by the spatial extent of the sound speed fluctuations. A term associated with a Fresnel zone for horizontal displacements of the unperturbed ray is neglected because the correlation length in the horizontal direction is much greater than in vertical in the ocean medium. The behavior of sound signals is characterized in different regions of $\Lambda$–$\Phi$ space. Assume that the path of the perturbed ray is separated from the unperturbed ray by a distance $a$ at the midpoint (Fig. 2), with the unperturbed ray followed from the origin ($\mathbf{0}$) to the receiver ($\mathbf{x}_R$). The full path length from source to receiver can then be written as

$$S\left(\mathbf{0}, \mathbf{x}_R\right) = S_0\left(\mathbf{0}, \mathbf{x}_R\right) + \frac{1}{2} A a^2 - \int \mu dS, \tag{9}$$

where $A$ is the phase curvature and the integral of $\mu$ is taken over the new path. It is convenient to set $\xi = a/L_v$ and define

$$u\left(\xi\right) = -\Phi^{-1} k_0 \int \mu dS. \tag{10}$$

Then the path length can be expressed in terms of dimensionless variables $u\left(\xi\right)$ and

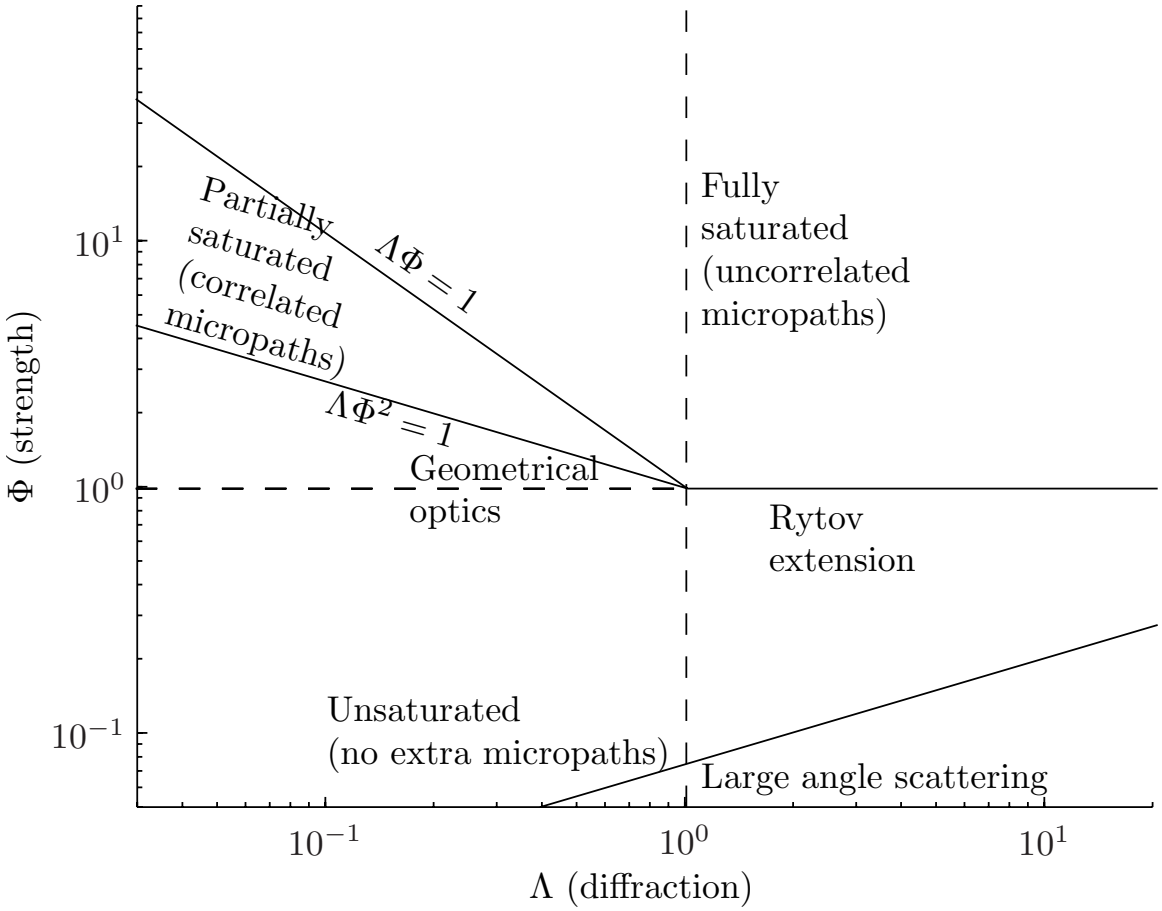


Figure 3. Regions in Λ–Φ space (after S. M. Flatté *et al.* [18]).

$\xi$ and the important parameters $\Phi$ and $\Lambda$:

$$k_0 S\left(\mathbf{0}, \mathbf{x}_R\right) \approx k_0 S_0\left(\mathbf{0}, \mathbf{x}_R\right) + \frac{1}{2}\frac{\xi^2}{\Lambda} + \Phi u\left(\xi\right). \tag{11}$$

The regions of different sound fluctuation behavior can be identified in terms of regions in Φ–Λ space (Fig. 3). In saturated (strong scattering) regions, when $\Phi > 1$ and $\Phi\Lambda > 1$, each unperturbed ray will split up into a number of micropaths. On the average the number of micropaths is $\Phi\Lambda$. The vertical spacing between these paths is typically of order $L_v$. In the diffractive, unsaturated regime ($\Lambda > 1$, $\Phi < 1$) the

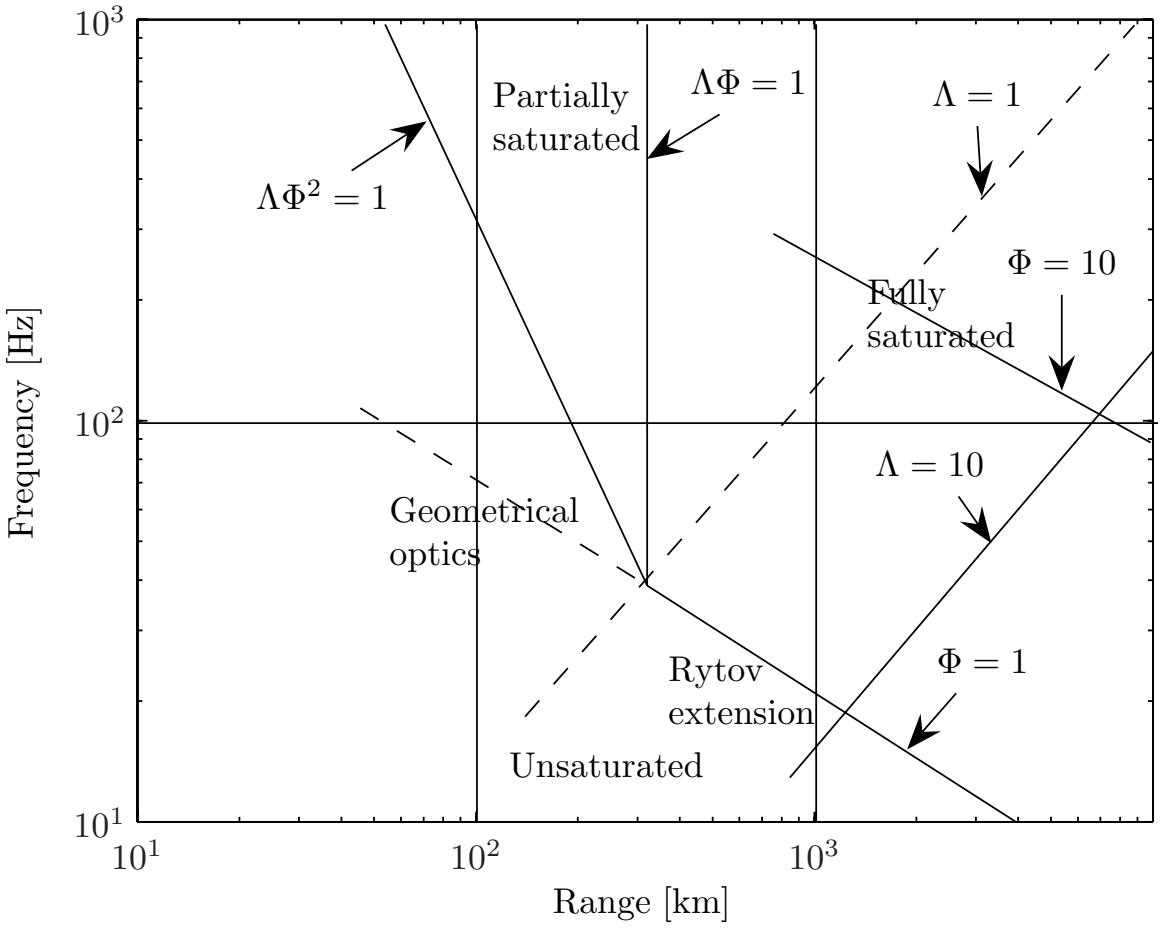


Figure 4. Sound transmission regions translated into range-frequency space (after S. M. Flatté *et al.* [18]).

small scattered wave is not well described by a ray approximation, but because $\Phi$ is small, a perturbation expansion can be made. The result is similar to the formulation in the geometrical optics regime. To determine in which region a particular sound-transmission is operating, one must calculate $\Phi$ and $\Lambda$, which depend on the sound frequency, the range from source to receiver, and on which unperturbed ray is considered. Figure 4 shows the regions translated into range-frequency space. Numerical methods are developed for computation of $\Phi$ and $\Lambda$ for arbitrary vertical sound speed and Brunt-Väisälä frequency profile [20].

The main flaw of this method is probably that the integrals for $\Phi$ and $\Lambda$ (Eqs. (2) and (8)) are computed along the unperturbed ray path and there is no justification for validity of these expressions for the ocean medium with the presence of range-dependent inhomogeneous perturbation of the sound speed. In the paper by Colosi *et al.* [21] it is pointed out that predictions of pulse spread and wave propagation regime were in strong disagreement with the observations during a 3250-km propagation experiment in the eastern North Pacific ocean. Pulse time spread estimates were more than two orders of magnitude too large, and $\Phi$–$\Lambda$ theory predicted full saturation, but experimental results suggested that the propagation was either in the partially saturated or the unsaturated regime.

### 2.1.3 Mode coupling (Dozier-Tappert theory and extensions)

An alternate approach makes use of the modal description of underwater sound propagation. In a range-dependent environment acoustic energy is scattered among modes with different mode numbers. The development of a theory of acoustic propagation in a random ocean based on statistics of normal mode amplitudes is described by Dozier and Tappert [10]. A system of stochastic ordinary differential equations, that are the coupled mode equations, is derived with randomness entering solely through the variation of the sound speed profile $\delta c$ .

The Helmholtz equation in cylindrical coordinates for the acoustic pressure $\bar{u}\,(z, r, \sigma)$ due to a point source with angular frequency $\sigma$ at $r = 0$ is

$$\frac{1}{r}\frac{\partial}{\partial r}\left(r\frac{\partial \bar{u}}{\partial r}\right) + \frac{\partial^2 \bar{u}}{\partial z^2} + k^2 \bar{u} = 0, \tag{12}$$

where $k = \sigma/c\,(z,r)$. The following boundary conditions are imposed: 1) The wave should be outgoing as $r \to \infty$. 2) The flat ocean surface is a pressure release surface: $\bar{u}\,(0,r,\sigma) = 0$. 3) The flat ocean bottom is rigid and totally reflecting: $\frac{\partial \bar{u}}{\partial n}\,(-h,r,\sigma) = \frac{\partial \bar{u}}{\partial z}\,(-h,r,\sigma) = 0$. In a stratified ocean (possibly including a weak perturbation $\delta c\,(z,r,t)$ ) the far field is described by

$$\frac{\partial^2 P}{\partial z^2} + \frac{\partial^2 P}{\partial r^2} + k^2 P = 0, \tag{13}$$

where $P = \sqrt{r}\bar{u}$. Now $P$ can be expanded in terms of normal modes $\phi_n$ of the deterministic background profile $\bar{c}\,(z)$ :

$$\frac{d^2\phi_n}{dz^2} + \frac{\sigma^2}{\bar{c}^2\,(z)}\phi_n = l_n^2\phi_n, \qquad n = 1,2,... \tag{14}$$

$$\phi\,(0) = 0, \qquad \frac{\partial \phi}{\partial z}\,(-h) = 0, \qquad \int dz\phi_n\phi_m = \delta_{nm}. \tag{15}$$

$$P\,(z,r,t) = \mathrm{e}^{-i\sigma t}\sum_{n=1}^{N} A_n\,(r,t)\,\phi_n\,(z)\,. \tag{16}$$

It is shown in [6] that under quasi-static and forward-scattering approximations, the problem can be reduced to the initial value problem and for the scaled amplitude $\xi_n = \sqrt{l_n}A_n$ it becomes:

$$\frac{\partial \xi_n}{\partial r}\,(r,t) - il_n\xi_n\,(r,t) = -i\sum_{m=1}^{N} R_{nm}\,(r,t)\,\xi_m\,(r,t)\,, \tag{17}$$

where

$$R_{nm}(r,t) = \frac{\sigma^2}{c_0^2 (l_n l_m)^{1/2}} \int dz \frac{\delta c(z,r,t)}{c_0} \phi_n(z) \phi_m(z). \tag{18}$$

Removing the oscillations by the substitution $\psi_n = e^{-il_n r}\xi_n$ yields the coupled mode equations:

$$\begin{aligned} \frac{\partial \psi_n}{\partial r}(r,t) &= -i \sum_{m=1}^{N} R_{nm}(r,t)\, \mathrm{e}^{i(l_m - l_n)r} \psi_m(r,t), \\ \psi_n(0,t) &= \psi_n^0(t), \qquad 1 \le n \le N. \end{aligned} \tag{19}$$

A closed system of equations for statistical averages of the solutions of the coupled-mode equations, called the coupled power equations, is derived which describes the transfer of energy between the propagating acoustic normal modes:

$$\begin{aligned} \frac{d}{dr} W_n(r) &= \sum_{\substack{m=1 \\ m \ne n}} a_{nm} [W_m(r) - W_n(r)] \qquad 1 \le n \le N, \\ W_n(0) &= \left|\psi_n^0\right|^2. \end{aligned} \tag{20}$$

Here $W_n(r) = \left\langle |\psi_n(r)|^2 \right\rangle$ . Equation (20) describes an irreversible tendency toward equilibrium, whereas the coupled mode equations (19) are reversible in range for any particular realization. The coefficients $a_{nm}$ in Eq. (20) are the transition probabilities between modes. The coupled power equations are derived under the following assumptions: 1) incoherent modes, i.e. $\langle \psi_n(r)\, \psi_m^*(r) \rangle = \langle |\psi_n(r)|^2 \rangle \delta_{nm}$; 2) random

phase sound speed perturbations, i.e. $\langle \hat{R}_{nm}(k)\,\hat{R}_{nm}(k')\rangle = \langle \left|\hat{R}_{nm}(k)\right|^2 \rangle \delta(k-k')$, (here $\hat{R}_{nm}(k) = \frac{1}{2\pi}\int_{-\infty}^{\infty} dr R_{nm}(r)\,\mathrm{e}^{ikr}$ ); and 3) independence of sound speed perturbation and modes, i.e. $\langle \hat{R}_{nm}(k)\,\psi_n(r)\,\psi_m^*(r)\rangle = \langle \hat{R}_{nm}(k)\rangle\langle \psi_n(r)\,\psi_m^*(r)\rangle$ and $\langle \hat{R}_{nm}(k)\,\hat{R}_{jm}(k')\,\psi_n(r)\,\psi_j^*(r)\rangle = \langle \hat{R}_{nm}(k)\,\hat{R}_{jm}(k')\rangle\langle \psi_n(r)\,\psi_j^*(r)\rangle$.

In addition to the average modal powers, described by the coupled power equations, coupled fluctuations equations are derived in [10]. Finally, the full statistical distribution of normal amplitudes is discussed, with the detailed analysis of its properties.

Another way to derive a mode coupling equations can be found in the work by Virovlyansky *et al.* [22]. The results are obtained for the wave field that obeys the parabolic equation. A monochromatic wave field at a carrier frequency $f$ in a two-dimensional acoustic waveguide with the sound speed $c(z,r)$ is governed by the Helmholtz equation (12), where $\sigma = 2\pi f$. It is convenient to introduce an envelope function $\bar{v}(z,r)$ connected to $\bar{u}(z,r)$ by an expression

$$\bar{u} = \frac{\bar{v}}{\sqrt{r}}\mathrm{e}^{ik_0 r}, \tag{21}$$

with $k_0 = \sigma/c_0$, where $c_0$ is the reference sound speed. In the far field this function is approximately described by the standard parabolic equation:

$$2ik_0\frac{\partial \bar{v}}{\partial r} + \frac{\partial^2 \bar{v}}{\partial z^2} - 2k_0^2 U\bar{v} = 0, \tag{22}$$

where

$$U(z,r) = \frac{1}{2}\left(1 - \frac{c_0^2}{c^2(z,r)}\right). \tag{23}$$

In each cross-section of a range-dependent waveguide the field is decomposed into a sum of the local modes, that is the modes of an imaginary range-independent waveguide whose depth structure coincides with that of a real one at the given range. The normal mode representation of the wave field in a range-dependent waveguide has the form

$$\bar{u}(z,r) = \sum_m a_m(r)\,\phi_m(z,r). \tag{24}$$

Substitution of this expression into Eq. (22) and use of the orthogonality condition for normal modes results in the mode coupling equation

$$\frac{da_m}{dr} + ik_0 H_m a_m = -\sum_{m_1} a_{m_1} \int dz \frac{\partial \phi_{m_1}}{\partial r}\phi_m. \tag{25}$$

Here $H_m$ is the value of the Hamiltonian associated with the $m$-th mode (a relationship between $H_m$ and mode number $m$ will be established in Sec. 4.1 by Eq. (89) or an asymptotic form of this equation, Eq. (100)). For a point source, Eq. (25) should be solved with an initial condition

$$a_m(0) = \phi_m(0, z_0). \tag{26}$$

The derivative $\partial\phi_m/\partial r$ can be written as an expansion

$$\frac{\partial\phi_m}{\partial r} = \sum_{\nu\neq 0} B_{m\nu}\phi_{m+\nu}. \tag{27}$$

Equation (25) now is written as

$$\frac{da_m}{dr} + ik_0 H_m a_m = \sum_{\nu\neq 0} B_{m\nu} a_{m+\nu}. \tag{28}$$

It is shown in [22] that

$$B_{m\nu} = \frac{1}{H_m - H_{m+\nu}} \int dz \phi_m \frac{\partial U}{\partial r} \phi_{m+\nu}. \tag{29}$$

In the high frequency approximation Eq. (29) reduces to

$$B_{m\nu} = -\frac{k_0}{2\nu\omega_m} V_{|\nu|}\left(I_m, r\right). \tag{30}$$

The form of $V_{|\nu|}\left(I_m, r\right)$ is given in Virovlyansky *et al.* [22], and $\omega_m$ is defined by Eq. (35). An important result follows directly from Eq. (29). Since $B_{m\nu} \sim \frac{1}{H_m - H_{m+\nu}}$, it can be concluded that the mode coupling coefficients $B_{m\nu}$ are larger for small absolute values of $\nu$. This means that in the presence of mode coupling the energy from a particular mode will be scattered primarily between neighboring modes. The same can not be easily concluded from Eq. (18).

## 2.2 Adiabatic approximation for modes

An important limiting case of the mode coupling problem is the so-called adiabatic limit. This is an approximation in which the interaction between normal modes is neglected. The amplitude of each mode and its vertical structure at a given section of the waveguide depend only on the distribution of the medium's parameters across this section. The physical meaning of this condition is that mode coupling is negligible. In the adiabatic approximation the right hand side of the mode coupling equation (28) is assumed to be negligible, and Eq. (28) can be integrated to obtain

$$a_m(r) = a_m(0)\,\mathrm{e}^{-ik_0\int_0^r H_m(r')dr'}. \tag{31}$$

The first-order correction can be obtained using a simple perturbation theory. Consider the case when only one mode with number $m_0$ is excited at $r = 0$, that is

$$a_m(0) = \delta_{mm_0.} \tag{32}$$

Substituting Eq. (31) with $a_m(0)$ defined by Eq. (32) into the right hand side of Eq. (28) we find that for $m \neq m_0$

$$a_m(r) = \mathrm{e}^{-ik_0\int_0^r H_{m_0}(r')dr'} q_m, \tag{33}$$

where

$$q_m = \int_0^r dr' B_{m,m_0-m}(r')\,\mathrm{e}^{i(m-m_0)\int_0^{r'}\omega_{m_0}(r'')dr''}. \tag{34}$$

Here

$$\omega_m = \omega_m\left(I_m\right) = \frac{dH\left(I\right)}{dI}|_{I_m} \tag{35}$$

and the quantity $I_m = I\left(H_m\right)$ is the action variable associated with the $m$-th mode. At high frequencies, when Eq. (30) is valid, $q_m$ can be presented in the form

$$q_m = -\frac{k_0}{2\left(m-m_0\right)}\int_0^r \frac{dr'}{\omega_m\left(r'\right)} V_{|m-m_0|}\left(r', I_m\right) \mathrm{e}^{i(m-m_0)\int_0^{r'}\omega_{m_0}(r'')dr''}. \tag{36}$$

The condition

$$|q_m| \ll 1 \tag{37}$$

(or its analog for the Helmholtz equation) is traditionally considered as a starting point for studying the applicability of adiabatic approximation. In particular it turns out that the inequality (37) requires that

$$R/L \ll 1, \tag{38}$$

where $R = 2\pi/\omega$ is the cycle distance of a ray and $L$ is the characteristic scale of the horizontal range dependence. Another criterion involving the dependence on a frequency of the propagating wave that was used by Milder [23] has the form

$$k_0 R^2/L \ll 1.$$

The research work discussed in Chapter 2 has focused on distributions of modal amplitudes as a function of range. In this dissertation we are investigating the as-

sociated wavefield structure in depth-range or depth-range-time space and discussing what properties of the environment control the wavefield structure and stability.

# 3 Some theoretical results

This chapter is devoted to the discussion of some recent important theoretical results that help to understand how the characteristics of the background sound speed structure are related to the wavefield structure and stability. Some connections between ray and normal mode theories are outlined and some results establishing the connection between the background sound speed profile and ray and travel time stability are presented.

## 3.1 The connection between the ray-based stability parameter $\alpha$ and mode-based waveguide invariant $\beta$: an aspect of ray-mode duality

In this section some important aspects of ray–mode duality are discussed. Starting with the Helmholtz equation, the system of ray equations is introduced, and then with the help of the action-angle variables introduced in range-independent environment an important connection between the ray and modal descriptions of the wavefield is derived.

Fixed frequency acoustic wave fields satisfy the Helmholtz equation

$$\nabla^2 \bar{u} + \sigma^2 c^{-2}(z, r)\, \bar{u} = 0, \tag{39}$$

where $\bar{u}(z, r, \sigma)$ is the Fourier transform of the acoustic pressure $u(z, r, t)$, $\sigma = 2\pi f$ is the angular frequency of the wavefield, and $c(z, r)$ is the sound speed. The propagation in a vertical plane $(z, r)$ is considered where $z$ is depth and $r$ is range. The

so-called short wave approximation can be used when $\sigma >> |\nabla c|$ , i.e. when acoustic wavelength is much smaller than all length scales that characterize variations in $c$. It is well known (see e.g.,[24]) that substitution of the geometric ansatz

$$\bar{u}\left(z,r,\sigma\right) = a\left(z,r\right)\mathrm{e}^{i\sigma T(z,r)} \tag{40}$$

into the Helmholtz equation (39) and collecting terms in descending powers of $\sigma$ yields the eikonal and transport equations. The solution to the eikonal equation can be reduced to the solution of ray equations. For guided wave propagation in the direction of increasing $r$ the ray equations may be written as

$$\frac{dz}{dr} = \frac{\partial H}{\partial p}, \qquad \frac{dp}{dr} = -\frac{\partial H}{\partial z}, \tag{41}$$

and

$$\frac{dT}{dr} = p\frac{dz}{dr} - H, \tag{42}$$

where $p = \frac{\partial T}{\partial z}$ is the $z$-component of the slowness vector and

$$H\left(p,z,r\right) = -\sqrt{c^{-2}\left(z,r\right) - p^2} \tag{43}$$

is the Helmholtz Hamiltonian that is equal to the minus $r$-component of the slowness vector. For the range-independent problem ($c = c\left(z\right)$ ) $z\left(r\right)$ and $p\left(r\right)$ (following rays) are periodic functions. The periodic motion is most naturally described using

action-angle variables $(I, \theta)$. The transformed ray equations are [25, 26]

$$\frac{dI}{dr} = -\frac{\partial \bar{H}}{\partial \theta} = 0, \tag{44}$$

$$\frac{d\theta}{dr} = \frac{\partial \bar{H}}{\partial I} = \omega\left(I\right), \tag{45}$$

$$\frac{dT}{dr} = I\omega\left(I\right) - \bar{H}\left(I\right) + \frac{d}{dr}\left(G - I\theta\right), \tag{46}$$

where $\bar{H}\left(I\right)$ is the transformed Hamiltonian and $G$ is the generating function of the canonical transformation

$$G\left(z, I\right) = \pi I \pm \int^{z} d\xi \sqrt{c^{-2}\left(\xi\right) - H^{2}\left(I\right)}, \tag{47}$$

which relates implicitly the new variables $(I, \theta)$ to the original variables $(p, z)$ through

$$p = \frac{\partial G}{\partial z}, \qquad \theta = \frac{\partial G}{\partial I}. \tag{48}$$

The action is defined as

$$I\left(H\right) = \frac{1}{\pi}\int_{\check{z}}^{\hat{z}} p\left(z\right) dz = \frac{1}{\pi}\int_{\check{z}}^{\hat{z}} dz \sqrt{c^{-2}\left(z\right) - H^{2}}, \tag{49}$$

where $\hat{z}$ $(\check{z})$ corresponds to the ray upper (lower) turning depth. The range of a ray cycle (double loop) is

$$R\left(H\right) = 2\pi\frac{dI}{dH} = \frac{2\pi}{\omega\left(I\right)} = -2H\int_{\check{z}}^{\hat{z}} \frac{dz}{\sqrt{c^{-2}\left(z\right) - H^{2}}}. \tag{50}$$

It is also convenient to introduce the corresponding expression for the single-cycle travel time:

$$T(H) = 2\int_{\check{z}}^{\hat{z}} \frac{c^{-2}(z)\,dz}{\sqrt{c^{-2}(z) - H^2}}. \tag{51}$$

Now, the stability parameter $\alpha(I)$, that is a property of a background sound speed profile, is defined as

$$\alpha(I) = \frac{I}{\omega(I)}\frac{d\omega}{dI}. \tag{52}$$

It follows from Eqs. (50) and (52) that $\alpha(I)$ can be expressed in the form

$$\alpha(H) = -2\pi\frac{I(H)}{R^2(I)}\frac{dR(H)}{dH}. \tag{53}$$

A connection between the ray stability parameter $\alpha$, obtained with the use of ray-based description, and the mode based waveguide invariant parameter $\beta$ [27, 28, 29] can be made. The modal description will be discussed in more detail in Sec. 4, where asymptotic expression relating to the normal mode based description will be derived. However, it is important to emphasize here that such a connection exists because the influence of the parameter $\alpha$ is essential in the study of wavefield structure and stability. Consistent with the asymptotic analysis presented here, an asymptotic expression for group slowness is

$$S_g(H) = \frac{T(H)}{R(H)} = \frac{-HR(H) + 2\pi I(H)}{R(H)}. \tag{54}$$

The justification for the latter expression is presented in Sec. 4.1. The waveguide

invariant is defined as [27, 28, 29]

$$\beta = \frac{\partial S_g(H)}{\partial H}. \tag{55}$$

It follows from Eqs. (50), (54) and (55) that $\beta$ can be expressed as

$$\beta = -2\pi \frac{I(H)}{R^2(H)} \frac{dR(H)}{dH}. \tag{56}$$

A comparison of (53) and (56) reveals $\alpha = \beta$. It should be emphasized that this result is based on asymptotic modal analysis, so only the asymptotic equivalence of $\alpha$ and $\beta$ is demonstrated. This result was derived by Brown *et al.* [29] with some relevant discussion of the influence of $\alpha$ (or $\beta$) on the wavefield structure and stability.

## 3.2 Review of results obtained by ray methods relating to the wavefield stability parameter

Ray stability and travel time stability are important characteristics of the wavefield in underwater acoustics. Ray stability was investigated by Beron-Vera and Brown [25] in environments consisting of a range-independent background sound-speed profile on which a range-dependent perturbation is superimposed. The results presented in that work show that ray stability is strongly influenced by the background sound speed structure; ray instability was shown to increase with increasing magnitude of $\alpha$. This conclusion was based largely on numerical simulations, but a very important observation follows directly from the action-angle formalism. Assume that the

sound speed can be split into a background (range-independent) part, $c(z)$, and a small range-dependent perturbation $\delta c(z,r)$. Then, to the lowest order in $\delta c/c$, the Hamiltonian takes the additive form

$$h = H(p,z) + \delta h(p,z,r). \tag{57}$$

By means of the canonical transformation, the ray equations (41) and (42) can be written in action-angle variables

$$\frac{dI}{dr} = -\frac{\partial}{\partial\theta}\delta\bar{h}, \qquad \frac{d\theta}{dr} = \omega + \frac{\partial}{\partial I}\delta\bar{h}, \tag{58}$$

and

$$\frac{dT}{dr} = I\frac{d\theta}{dr} - \bar{H} - \delta\bar{h} + \frac{d}{dr}(G - I\theta), \tag{59}$$

where $h(p,z,r) \rightarrow \bar{H}(I) + \delta\bar{h}(I,\theta,r)$. The action-angle form of the variational equations for the perturbed system strongly suggests that the ray stability and $d\omega/dI$ (or $\alpha$) are closely linked. The mechanism through which $d\omega/dI$ influences ray stability can be seen from the action-angle form of the ray variational equations,

$$\frac{d}{dr}\delta I = -\frac{\partial^2\delta\bar{h}}{\partial I\partial\theta}\delta I - \frac{\partial^2\delta\bar{h}}{\partial\theta^2}\delta\theta, \tag{60}$$

$$\frac{d}{dr}\delta\theta = \frac{d\omega}{dI}\delta I + \frac{\partial^2\delta\bar{h}}{\partial I^2}\delta I + \frac{\partial^2\delta\bar{h}}{\partial I\partial\theta}\delta\theta. \tag{61}$$

Equations (58), (60) and (61) describe the evolution of $(I,\theta,\delta I,\delta\theta)$. If one assumes that the second derivatives of $\delta\bar{h}$ are zero-mean random variables, then when $d\omega/dI =$

0 these terms should lead to slow (power-law) growth of $\delta\theta$ and $\delta I$. But if $|d\omega/dI|$ is large, this term will cause $|\delta\theta|$ to rapidly grow for any nonzero $|\delta I|$. The perturbation terms will then lead to a mixing of $|\delta\theta|$ and $|\delta I|$. The term $d\omega/dI$ will lead, in turn, to further growth of $|\delta\theta|$. As this process repeats itself, both $|\delta I|$ and $|\delta\theta|$ are expected to grow rapidly. Thus ray instability is expected to be significantly enhanced when $|d\omega/dI|$ is large. The importance of $\alpha$ was illustrated with numerical simulations of ray motion in deep ocean environments including internal-wave-induced scattering, and in upward-refracting environments including rough surface scattering.

Another important characteristic of the wavefield in underwater acoustics is the ray travel time. It represents an arrival time of a pulse signal propagating along a ray path connecting the source and the receiver. In field experiments such pulses, especially those propagating through steep ray paths, can sometimes be resolved and identified even at ranges of hundreds of kilometers and longer. In many schemes of acoustic monitoring of ocean structure, ray travel times are the main observables used to reconstruct variations in the environment. Travel time stability was investigated in recent works by Beron-Vera and Brown [26] and Virovlyansky [30]. Three different measures of travel time spreads were considered in [26]: (i) unconstrained spread of ray travel time along the timefront; (ii) unconstrained spread of rays whose turning history and final depth are fixed but whose final range is not; and (iii) scattering-induced broadening of an individual branch of the timefront at a fixed measurement location. All three measures of time spreads were shown to be largely controlled by $\alpha$, a property of the background sound-speed profile. Surprisingly, this is the same property that controls ray spreading and, hence, ray amplitudes. The argument

why travel time spreads should be controlled by the same property comes from the variational equations in the extended phase space $(I, \theta, T)$ (Eqs. (60), (61) together with (58)) and another equation for the variation of travel time:

$$\frac{d}{dr}\delta T = I\frac{d\omega}{dI}\delta I + I\frac{\partial^2 \delta \bar{h}}{\partial I^2}\delta I + I\frac{\partial^2 \delta \bar{h}}{\partial I \partial \theta}\delta\theta - \frac{\partial \delta \bar{h}}{\partial \theta}\delta\theta. \tag{62}$$

For the class of problems considered here the non-zero sound speed perturbation terms on the right hand side of Eqs. (60)-(62) are generally much smaller than the $d\omega/dI$ and $Id\omega/dI$ terms. Thus, one expects that the dominant cause of the growth of $(\delta I, \delta\theta, \delta T)$ is the background sound speed structure via $\alpha$, rather than the small sound speed perturbation terms. Loosely speaking, the perturbation terms provide a seed for the growth of $(\delta I, \delta\theta, \delta T)$, while the subsequent growth of these quantities is largely controlled by $\alpha$.

## 3.3 Theory of spreads of energy in depth-range domain for continuous wave fields. Fresnel zones for modes

All discussions of the wavefield structure and stability up to this point are limited to the analysis in depth-time space. Other important characteristics of the wavefield describe the wavefield structure in depth-range space for a monochromatic source. One such characteristic is the width (in range or in depth) within which most of the energy of a particular mode is contained; this is closely related to the concept of the Fresnel zones for modes. The influence of $\alpha$ on Fresnel zone width is investigated in this section.

The notion of Fresnel zones for modes is analogous to the usual Fresnel zones

introduced for rays. In the ray representation each ray trajectory is governed by Snell's law $\cos\theta = -c(z)\,H$ , where $\theta$ is the current grazing angle and $H$ is constant following a ray when $c = c(z)$. The ray trajectory connecting the lower turning point $\check{z}$ and the point at the depth $z$ has horizontal extent

$$R(z,H) = -H\int_{\check{z}}^{z}\frac{dz}{\sqrt{c^{-2}(z) - H^2}}. \tag{63}$$

The ray cycle distance (double loop) is determined by Eq. (50). For simplicity it is assumed that both turning points are inside the water column and lateral shifts on both boundaries are neglected. A ray path connecting a source at $(z_0, r)$ and receiver at $(z, r)$ satisfies

$$r = r_{N,j}(z,H) = a_j R(z_0,H) + NR(H) + b_j R(z,H), \tag{64}$$

where $N$ is the number of lower turning points, and $a_j$ and $b_j$ are constants equal to $+1$ or $-1$, depending on the sign of the launch and arrival angles. The rays are separated into four groups distinguished by the index $j = 1, 2, 3, 4$, according to whether the trajectory leaves the source in the upward or downward direction and arrives at the point $(z, r)$ from above or below. In the scope of the ray representation the solution of the Helmholtz equation is [31, 32]

$$\bar{u}(z,r) = \sum_{j=1}^{4}\sum_{N} A_{N,j}\mathrm{e}^{i\Psi_{N,j}}\big|_{H=H_{N,j}} \tag{65}$$

with the ray amplitudes

$$A_{N,j} = \frac{(-H)^{1/2} \mathrm{e}^{\frac{i\pi}{4}}}{\sqrt{r \left|\partial r_{N,j}/\partial H\right|}} \frac{1}{\sqrt[4]{\left(c^{-2}\left(z_0\right) - H^2\right)\left(c^{-2}\left(z\right) - H^2\right)}}, \tag{66}$$

and phases

$$\begin{aligned} \Psi_{N,j} &= \sigma\left[a_j J\left(z_0, H\right) + 2\pi N I\left(H\right) + b_j J\left(z, H\right) - Hr\right] - \\ &\quad -N\pi - \frac{\pi}{4}\left(a_j + b_j\right) + \frac{\pi}{4}\mathrm{sgn}\left(\frac{\partial r_{N,j}}{\partial H}\right), \end{aligned} \tag{67}$$

where

$$J\left(z, H\right) = \int_{\check{z}}^{z} \sqrt{c^{-2}\left(\xi\right) - H^2} d\xi, \tag{68}$$

$I\left(H\right)$ is the action given by Eq. (49) and the function sgn is the sign of its argument.

The normal mode solution in the far field can be easily found by the use of the asymptotic form of the Hankel function. Asymptotically, the function $\phi_m\left(z, \sigma\right)$ between the turning points can be expressed as [31, 32]

$$\phi_m\left(z, \sigma\right) = \phi_m^+\left(z, \sigma\right) + \phi_m^-\left(z, \sigma\right), \tag{69}$$

where

$$\phi_m^{\pm}\left(z, \sigma\right) = \frac{1}{\sqrt[4]{c^{-2}\left(z\right) - H_m^2}} \sqrt{\frac{-H_m}{R\left(H_m\right)}} \exp\left[\pm i\left(\sigma J\left(z, H_m\right) - \pi/4\right)\right]. \tag{70}$$

The functions $\phi_m^+$ and $\phi_m^-$ present upgoing and downgoing waves (the so-called Bril-

louin waves) forming the $m$-th mode. Within the context of the WKB approximation the mode representation of the wavefield (the monochromatic problem is considered here) takes the form

$$\bar{u}(z,r) = \sum_{j=1}^{4} \sum_{m} B_{m,j} \mathrm{e}^{i\Phi_{m,j}}|_{H=H_m}, \tag{71}$$

where

$$B_{m,j} = \sqrt{\frac{-2\pi H}{\sigma r}} \frac{1}{R(H)} \frac{1}{\sqrt[4]{\left(c^{-2}(z_0) - H^2\right)\left(c^{-2}(z) - H^2\right)}}, \tag{72}$$

$$\Phi_{m,j} = \sigma \left[a_j J(z_0, H) + b_j J(z, H) - Hr\right] - \frac{\pi}{4}(a_j + b_j) + \frac{\pi}{4}. \tag{73}$$

Here $a_j$ and $b_j$ are the same constants as those in Eq. (67).

Let us now compare the phases of two terms in Eq. (71) having the same index $j$ and corresponding to the $m$-th and $(m+\mu)$-th modes. It is shown in [32] that, along the trajectory of the mode ray, the approximate relation

$$\Phi_{m+\mu,j} - \Phi_{m,j} = -2\pi N\mu - \left(\frac{2\pi}{R(H_m)}\right)^2 \frac{1}{2\sigma} \frac{\partial r_{N,j}(z, H_m)}{\partial H} \mu^2 \tag{74}$$

holds for $|\mu| \ll m$. The value of $|\mu|$ at which the last term becomes equal to $\pi$ can be chosen as an estimation of the number of modes constructively interfering with the $m$-th mode along one of its mode rays. Denoting these estimates as $M_m^{\pm}$ we get

$$M_m^{\pm} = \sqrt{\frac{\sigma R^2(H_m)}{2\pi \left|\partial r_{N,j}(z, H_m)/\partial H\right|}} = \sqrt{R_m(H) \left|\frac{\tan\theta_m^{\pm}}{\partial z_m^{\pm}/\partial m}\right|}. \tag{75}$$

Here $\partial z_m^{\pm}/\partial m = z_{m+1}^{\pm}(r) - z_m^{\pm}(r)$, and $\theta_m^{\pm}$ are the grazing angles of the mode rays.

Equation (75) cannot be used near caustics where $M_m^{\pm}$ goes to infinity. Note that far from caustics the derivatives $|\partial r_{N,j}/\partial H|$ are almost linearly increasing with distance. This means that $M_m^{\pm}$ are decreasing with distance, on average as $r^{-1/2}$, and at large enough ranges each mode ceases to add in phase with neighboring modes.

Now we derive the expression for the width of the Fresnel zones on a cylindrically symmetric surface. Let us consider a surface $r = r_s$ surrounding the point source that produces a monochromatic wave. The total field complex amplitude $\bar{u}(z, r)$ at $r \geq r_s$ is connected with the amplitude at the cylindrical surface by the approximate relations

$$\bar{u}(z, r) = \sum_m U_m \phi_m(z) \, \mathrm{e}^{-i\sigma H_m (r - r_s)}, \tag{76}$$

$$U_m = \int_{-h}^{0} \bar{u}(z, r_s) \, \phi_m(z) \, dz. \tag{77}$$

Dividing $\phi_m(z)$ into two terms according to Eq. (69) and using the ray representation for $\bar{u}(z, r_s)$ (Eq. (65)) we get the following expression for the mode amplitudes $U_m$:

$$U_m = \sum_{N,j} \left( P_{N,j}^{+} + P_{N,j}^{-} \right), \tag{78}$$

where

$$P_{N,j}^{\pm} = \int dz A_{N,j} \mathrm{e}^{iQ_{N,j}^{\pm}}, \tag{79}$$

$$Q_{N,j} = \Psi_{N,j}^{\pm} \pm \left[ \sigma J(z, H_m) - \pi/4 \right]. \tag{80}$$

According to the Huygens–Fresnel principle [33] the field at $r \geq r_s$ is a result of interference of waves generated by secondary (virtual) sources on the surface $r = r_s$.

The contribution from the sources located in the depth interval $z_1 \leq z \leq z_2$ (the difference $z_2 - z_1$ is assumed to be considerably greater than the wavelength) are given by Eqs. (76)-(80) with the integrals in Eqs. (79) and (80) running from $z_1$ to $z_2$. So, as it is shown by Virovlyansky *et al.* [32], the constituent of the total field formed by the secondary sources located in the above range can be approximately represented as

$$\bar{u}\left(z,r\right)=\sum_{m}\sqrt{-\frac{2\pi}{\sigma H_m r}}\left[\xi_m^{+}\phi_m^{+}\left(z_0\right)+\xi_m^{-}\phi_m^{-}\left(z_0\right)\right]\phi_m\left(z\right)\mathrm{e}^{-i\sigma H_m(r-r_s)+i\pi/4}, \tag{81}$$

where

$$\xi_m^{\pm}=\frac{1}{\rho_m^{\pm}}\int_{z_1}^{z_2}dz\exp\left[-i\mathrm{sgn}\left(\frac{\partial r_{N,j}}{\partial H}\right)_{r=r_s}\left(\frac{\pi\left(z-z_m^{\pm}\left(r_s\right)\right)^2}{\left(\rho_m^{\pm}\right)^2}-\frac{\pi}{4}\right)\right]. \tag{82}$$

The radii of the first Fresnel zones in vertical direction are:

$$\rho_m^{\pm}=\sqrt{\frac{1}{f}\left|\frac{\partial r_{N,j}\left(z,H_m\right)}{\partial H}\right|\tan^2\theta_m^{\pm}}=\sqrt{R\left(H_m\right)\left|\frac{\partial z_m^{\pm}}{\partial m}\tan\theta_m^{\pm}\right|}. \tag{83}$$

This result shows that comparatively small intervals surrounding the depths $z_m^{\pm}\left(r_s\right)$ on the surface $r=r_s$ can be indicated, where the secondary sources are located which play the main role in forming the field of an $m$-th mode. It should be noted, however, that the Fresnel zones are not circles, but it is convenient to use the term "radii" to describe their widths. It seems that these widths are largely controlled by the background invariant parameter $\beta$. It is expected that the radii of Fresnel zones to be proportional to $|\beta|^{1/2}$ , because it follows directly from Eq. (83) that for complete

ray cycles, $r = nR$,

$$\rho_m^{\pm} = \sqrt{\frac{2\pi n}{f}\frac{|\beta|}{\omega^2 I}}|_{H=H_m}. \tag{84}$$

# 4 Modal group time spreads in weakly range-dependent deep ocean environments

In this chapter the temporal spread of modal group arrivals in weakly range-dependent deep ocean environments is considered. First, some basic results relating to the modal description of transient underwater sound fields are presented. The main steps of the mode processing technique, which are used for modal analysis of numerical simulations and experimental data are outlined in Sec. 4.1. Then the concept of "modal group time spreads" is introduced and deterministic modal group time spreads in a range-independent environment are discussed in Sec. 4.2. In Sec. 4.3 the notion of a dispersion diagram is presented. A new method to improve the accuracy of modal group time spreads estimates is presented in Sec. 4.4. The scattering-induced contribution to modal group time spreads is discussed in detail in Sec. 4.5. Various numerical results that support theoretical investigations are presented in Sec. 4.7 and Sec. 4.8.

## 4.1 Modal description of underwater sound propagation. Mode processing technique

In this section basic results relating to modal group time spreads are presented. The phrase "modal group arrival" is taken here to mean the contribution to a transient wavefield corresponding to a fixed mode number. The measurement of modal group arrivals requires that the wavefield be measured on a vertical array that is sufficiently long and dense to allow the processing steps described below to be performed. Receiving array deficiencies will be discussed in Sec. 5.2 and 5.3. In Secs. 4.1-4.4 it

is assumed that the sound speed is a function of depth only, $c = c(z)$. Some of the material presented in this section is contained in [34, 29].

It is assumed that the transient acoustic field, where $u(z, r, t)$ denotes acoustic pressure, is generated by a transient point source, with time history $s(t)$, located at $r = 0$, $z = z_0$. Thus $u(z, r, t)$ satisfies

$$\nabla^2 u(z, r, t) - c^{-2}(z) \frac{\partial^2 u(z, r, t)}{\partial t^2} = -\delta(z - z_0) \frac{\delta(r)}{2\pi r} s(t). \tag{85}$$

Let $\bar{s}(\sigma)$ denote the Fourier transform of $s(t)$, and similarly for $\bar{u}(z, r, \sigma)$, where $\sigma = 2\pi f$ is angular frequency. The solution to Eq. (85) can be written as a Fourier integral:

$$u(z, r, t) = \frac{1}{2\pi} \int_{-\infty}^{\infty} \bar{s}(\sigma) \bar{u}(z, r, \sigma) \mathrm{e}^{-i\sigma t} d\sigma, \tag{86}$$

where

$$\bar{u}(z, r, \sigma) = \frac{i}{4} \sum_{m=0}^{\infty} \phi_m(z_0, \sigma) \phi_m(z, \sigma) H_0^{(1)}(\sigma p_m r) / \int \phi_m^2(z, \sigma) dz \tag{87}$$

is a sum of normal modes, and $H_0^{(1)}$ is the zeroth order Hankel function of the first kind. The normal modes $\phi_m(z, \sigma)$ satisfy

$$\frac{d^2 \phi_m}{dz^2} + \sigma^2 \left( c^{-2}(z) - p_m^2 \right) \phi_m = 0, \tag{88}$$

together with a pair of boundary conditions, where $p_m = k_m/\sigma$ is a discrete value of

the horizontal component of the slowness vector $p_r = k_r/\sigma$. (The variables $k_m$ and $p_m$ are discrete samples of the continuous variables $k_r$ and $p_r$.) Imposition of these conditions leads to a quantization condition

$$p_m = p_r\left(m, \sigma\right), \; m = 0, 1, 2, ..., \tag{89}$$

which determines the allowed values of $p_m\left(\sigma\right)$, $m = 0, 1, 2, ....$ The contribution to the wavefield from the mode with frequency $\sigma$ and mode number $m$ can be written

$$\bar{u}_m\left(r, \sigma\right) = \int \bar{u}\left(z, r, \sigma\right) \phi_m\left(z, \sigma\right) dz / \int \phi_m^2\left(z, \sigma\right) dz. \tag{90}$$

The inverse Fourier transform of $\bar{u}_m\left(r, \sigma\right)$ is $u_m\left(r, t\right)$ which has the asymptotic form

$$u_m\left(r, t\right) \approx \frac{1}{2\pi} \int \frac{\bar{a}_m\left(\sigma\right)}{\sqrt{r}} \mathrm{e}^{i\left(k_m(\sigma) r - \sigma t\right)} d\sigma, \tag{91}$$

where

$$\bar{a}_m\left(\sigma\right) = \frac{i}{4} \left(\frac{2}{\pi k_m}\right)^{1/2} \mathrm{e}^{-i\pi/4} \phi_m\left(z_0, \sigma\right) \overline{s}\left(\sigma\right) / \int \phi_m^2\left(z, \sigma\right) dz \tag{92}$$

(here the far-field approximation $\sigma p_m r \gg 1$ is assumed).

Now the main steps of the mode processing technique can be outlined. In order to compute contributions to a given transient wavefield from each mode number, one has to apply direct Fourier transform to the given transient wavefield to obtain the frequency spectrum of this wavefield. Then this frequency domain field is substituted instead of $\bar{u}\left(z, r, \sigma\right)$ into Eq. (90) to compute individual modal contributions in

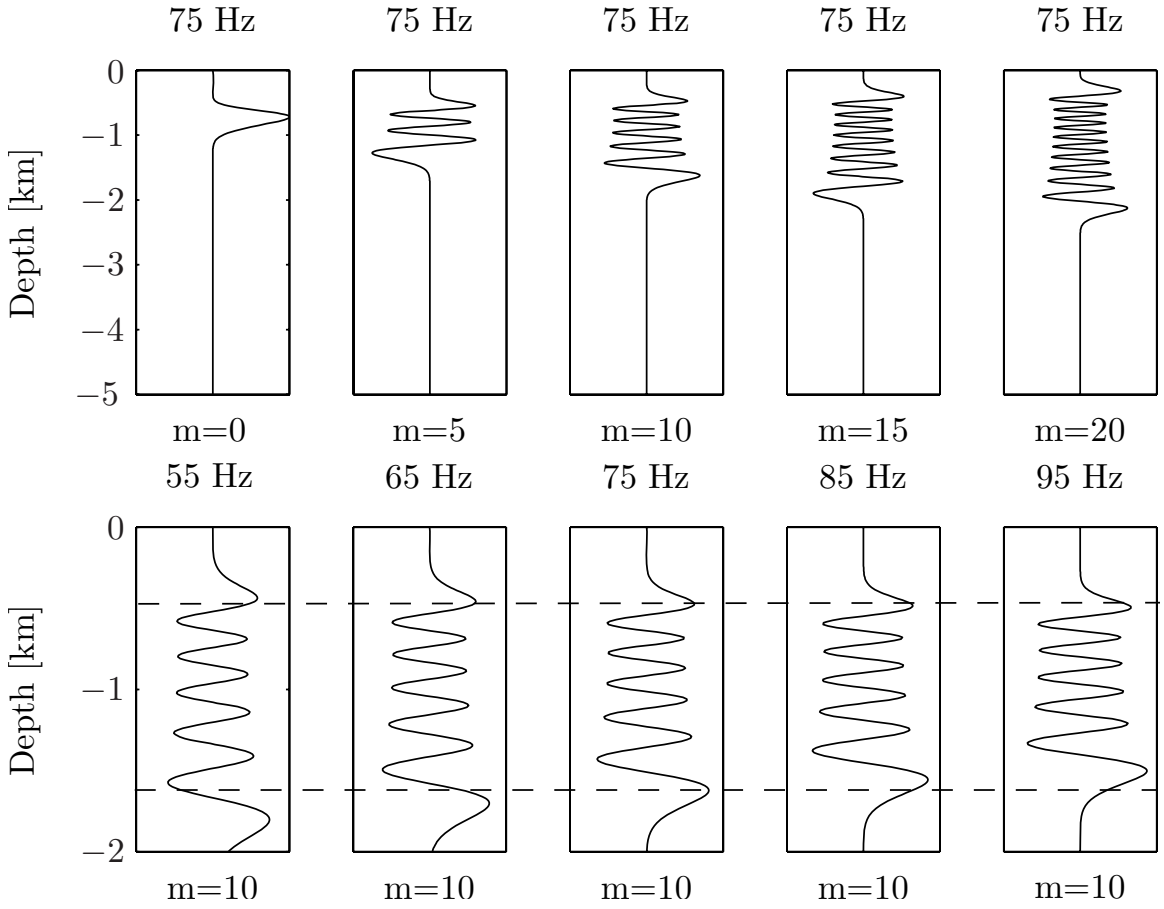


Figure 5. The structure of normal modes in a typical midlatitude ocean environment. The upper panels are different mode numbers $m = 0, 5, 10, 15$, and 20 computed for the same frequency of the acoustic source, $f = 75$ Hz. The lower panels are for the same mode number $m = 10$, computed for different frequencies of the acoustic source $f = 55, 65, 75, 85$, and 95 Hz.

frequency domain, and then application of the inverse Fourier transform allows the computation of contributions to the transient wavefield in time domain for each mode number. This technique is based on orthogonality of normal modes and sometimes called the direct projection technique. It requires that the acoustic field is recorded on a vertical array that is both dense and long.

The conceptual picture (Fig. 5) that shows different modal structures helps to understand how the mode processing should be performed. It is necessary to compute

the complete set of propagating modes in the given environment for the full frequency band of interest. The number of propagating modes is different at different frequencies (increases with increasing frequency). In a typical midlatitude ocean environment the number of propagating non-surface-reflecting modes generated by a 75 Hz acoustic source is approximately 70. The five upper panels in Fig. 5 show modal structure for different mode numbers ($m = 0, 5, 10, 15$, and 20) computed for 75 Hz frequency. Note that the number of zero-crossings of each mode is equal to the mode number. The five lower panels show modal structure for fixed mode number ($m = 10$) computed for five different frequencies ($f = 55, 65, 75, 85$, and 95 Hz). Though the structure of the mode looks similar, it is changing with frequency: the distance between neighboring maxima and minima decreases with increasing frequency. This frequency dependence is crucial for correct application of the mode processing technique when individual modal contributions in frequency domain are computed with the use of Eq. (90).

## 4.2 Deterministic modal group time spreads

Under the assumption of a narrow-band signal (i.e., that the spectral content of the source is sharply peaked around the center frequency $\sigma_0 = 2\pi f_0$) a Taylor series expansion of $k_m(\sigma)$ about $\sigma_0$ gives

$$k_m(\sigma) \approx k_m(\sigma_0) + S_g(m, \sigma_0)(\sigma - \sigma_0) + \frac{1}{2}\frac{dS_g}{d\sigma}(m, \sigma_0)(\sigma - \sigma_0)^2, \qquad (93)$$

where $S_g(m, \sigma) = dk_m/d\sigma$ is the group slowness. Consistent with the narrow-band assumption and Eq. (93) we shall assume that $\bar{a}_m(\sigma)$ can be approximated by a

Gaussian $\bar{a}_m(\sigma) = A\mathrm{e}^{\left(-\frac{\pi(f-f_0)^2}{(\Delta f)^2}\right)}$ that is peaked at the center frequency $\sigma_0$. This assumption allows the Fourier integral (91) to be evaluated analytically. The result is

$$u_m(r,t) = |A| \sqrt{\frac{\Delta f}{r\Delta t_m^0(r)}} \exp\left(-\frac{\pi\left(t - S_g(m,\sigma_0)\, r\right)^2}{\left(\Delta t_m^0(r)\right)^2}\right) \exp\left(i\left(k_m(\sigma_0)\, r - \sigma_0 t + \gamma\right)\right). \tag{94}$$

This represents a slowly-varying dispersive wavetrain whose envelope moves at the group slowness $S_g(m,\sigma_0)$, under which surfaces of constant phase move at the phase slowness $p_m$. Note that this statement remains valid even if higher order terms are retained in the Taylor series expansion (93). The point to emphasize here is that energy propagates at the group slowness, and the time of arrival of modal energy is $t = S_g r$. The exact form of the phase term $\gamma$ in (94) is not important for our purposes. The temporal width of the envelope, i.e., the modal group time spread, is

$$\Delta t_m^0(r) = \sqrt{\Delta t_{bw}^2 + \Delta t_d^2}. \tag{95}$$

Here

$$\Delta t_{bw} = (\Delta f)^{-1} \tag{96}$$

and

$$\Delta t_d = -2\pi r \Delta f \beta(m,\sigma_0) \frac{\partial p_r}{\partial \sigma}(\sigma_0), \tag{97}$$

where

$$\beta(m,\sigma) = -\frac{\partial S_g}{\partial p_r} \tag{98}$$

is the waveguide invariant [27, 28, 29]. The product $-\beta(m,\sigma)\,\partial p_r(\sigma)/\partial\sigma$ is the derivative $\partial S_g(m,\sigma)/\partial\sigma$. Partial derivatives are used here to emphasize that $m$ is held constant. Simplification of (97) and (98) is generally possible if the quantization condition (89) is known. These expressions have a particularly simple form when a simple asymptotic form of the quantization condition is used. These expressions will be derived at the end of this section. Another asymptotic approximation will be discussed in the Sec. 4.4. The superscript 0 is used in $\Delta t_m^0$ in Eq. (95) to distinguish this quantity from $\Delta t_m$, defined below, which includes a scattering contribution.

It should be emphasized that the validity of Eqs. (95)-(98) is not limited to asymptotic analysis. These results do, however, require that $\beta(m,\sigma_0) \neq 0$ (so the quadratic term in the Taylor series expansion (93) does not vanish) and that the bandwidth is sufficiently narrow that across this band $\beta(m,\sigma)$ is approximately constant. The geometric interpretation of these constraints is that the slope of the dispersion curve – discussed in the following section – for mode number $m$ is finite and nearly constant across the relevant frequency band $\Delta f$.

The widths $\Delta f$ and $\Delta t$ are defined as the half-widths of the Gaussian distributions at the point where the amplitude of the distribution (in $f$ or in $t$) is reduced by a factor of $\mathrm{e}^{-\pi}$ relative to the peaks. Equivalently, $\Delta f$ and $\Delta t$ are the full widths of the Gaussian at the points where the amplitude is reduced by a factor of $\mathrm{e}^{-\pi/4} \approx 0.456 \approx 0.5$. Thus, for distributions that can be approximated as Gaussians, to a good approximation $\Delta f$ and $\Delta t$ can be defined as the full width of the distributions at the half-amplitude points.

Equation (97) can be written as $\Delta t_d = r\left(\partial S_g(\sigma_0)/\partial\sigma\right)\Delta\sigma$, where $\Delta\sigma = 2\pi\Delta f$.

Note that the validity of the truncated Taylor series expansion (93) rests on the assumption that the curvature of $S_g(\sigma)$ in the $\Delta\sigma$ band centered at $\sigma = \sigma_0$ is small. If this condition is satisfied, then an equivalent expression is $\Delta t_d = r|S_g(m, \sigma_0 + \Delta\sigma/2) - S_g(m, \sigma_0 - \Delta\sigma/2)|$. The correctness of the latter expression is an obvious consequence of the negligible curvature assumption together with the observation that the time of arrival of modal energy is $t = S_g(m, \sigma) r$. An immediate consequence of the latter observation is the general result

$$\Delta t_d = r \left[ \max_{|\sigma - \sigma_0| \leq \Delta\sigma/2} S_g(m, \sigma) - \min_{|\sigma - \sigma_0| \leq \Delta\sigma/2} S_g(m, \sigma) \right] \tag{99}$$

which holds even when $S_g(m, \sigma)$ is not a monotonic function of $\sigma$ for a fixed $m$. Note that according to (99) $d\Delta t_d / d\Delta\sigma \geq 0$, but that this derivative is generally not constant, as assumed in (97). Equation (99) is a generalization of (97). Note that we have shown that (95), (96) and (99) are consistent with each other only in the limit of small bandwidth, where (99) reduces to (97). But (95), (96) and (99) predict the correct behavior in the limits of small and large $r$, so it is natural to assume that (95) remains approximately valid when (99) replaces (97). Finally, we emphasize that the validity of the results presented so far is not limited to asymptotic validity.

In an environment in which $c(z)$ has a single minimum, it is well known [31, 35] that modes with two internal (nonreflecting) turning points asymptotically satisfy the quantization condition

$$\sigma I(p_r) = m + \frac{1}{2}, \; m = 0, 1, 2, ..., \tag{100}$$

where the classical action

$$I(p_r) = \frac{1}{\pi} \int_{\check{z}(p_r)}^{\hat{z}(p_r)} \left( c^{-2}(z) - p_r^2 \right)^{1/2} dz \tag{101}$$

with $c(\hat{z}(p_r)) = c(\check{z}(p_r)) = 1/p_r$, where $\check{z}$ and $\hat{z}$ are lower and upper turning points, respectively. Note that these equations define $p_m = p_r(m, \sigma)$. For the class of problems for which (100) is valid

$$S_g(p_r) = \frac{T(p_r)}{R(p_r)}. \tag{102}$$

Here $R(p_r) = -2\pi dI/dp_r$ and $T(p_r) = 2\pi I(p_r) + p_r R(p_r)$ are the range and travel time, respectively, of a ray double loop. Use of Eqs. (100)-(102) leads to a simple explicit expression for $\Delta t_d$ (97),

$$\Delta t_d = -2\pi r \Delta f \frac{I}{R(I) f_0} \beta(I), \tag{103}$$

where $I$ and $R(I)$ are those values corresponding to the relevant $(m, \sigma_0)$ pair and $\beta(I) = \frac{2\pi I}{R^2} \frac{\partial R}{\partial p_r}$.

## 4.3 Dispersion diagrams

The dispersion diagram [34] shows the dependence of group slowness on frequency and mode number. The asymptotic quantization condition (100) and asymptotic expression for the group slowness (102) provide a very simple connection between phase slowness, group slowness, acoustic frequency, and mode number. This connection

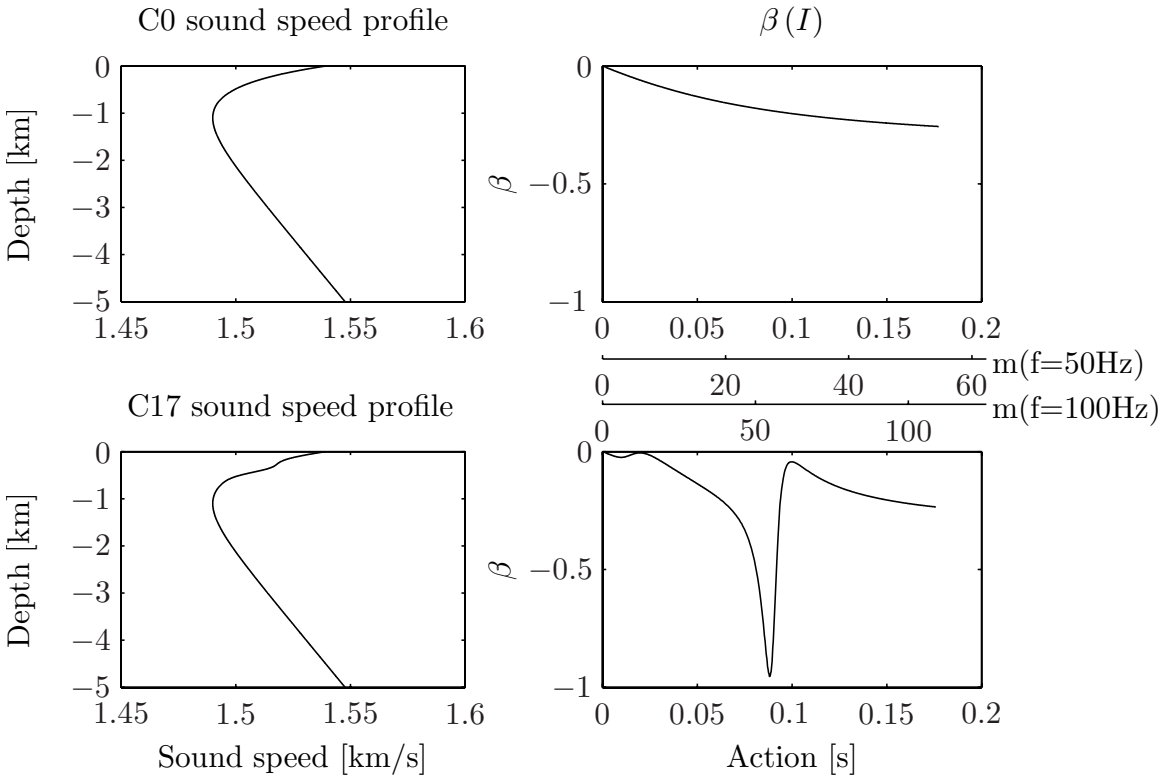


Figure 6. Sound speed profiles: C0 (upper left) and C17 (lower left) and $\beta$ curves as functions of action for C0 profile (upper right) and for C17 (lower right). The two axes in the middle of right panel are mode number axes.

allows the construction of dispersion diagram that supplies important information about the structure of modal arrivals in time. Dispersion curves are most naturally plotted as a family of curves, each corresponding to a fixed value of $m$, in $(f, S_g)$ space. Here we have produced these diagrams for two different environments: canonical environment derived by Munk [36] (C0) and slightly modified canonical profile with a small Gaussian disturbance added in the upper ocean (C17) (Fig. 6).

Figure 6 shows two different sound speed profiles (left panels). Upper left panel is the canonical profile C0 [36], $c_M(z)$, and lower left panel is the perturbed canonical profile C17, $c(z) = c_M(z) + dc \exp\left(-\frac{1}{2}\left((z - z_c)/z_w\right)^2\right)$, $c_M = c_a\left(1 + \varepsilon\left(\mathrm{e}^{\eta} - \eta - 1\right)\right)$ with $\eta = 2\left(z - z_a\right)/b$. Here $z$ increases upwards, $z_a = -1.1$ km is the sound channel

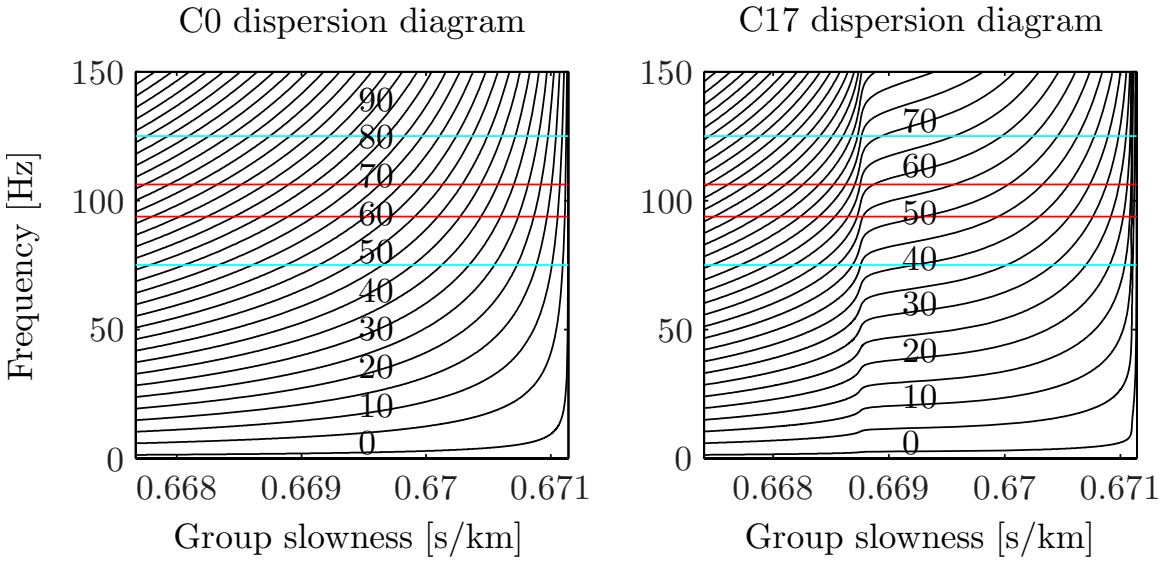


Figure 7. Dispersion diagrams for canonical profile C0 (left panel) and modified canonical profile C17 (right panel). Two pairs of hotizontal lines on each diagram correspond to the acoustic source with central frequency $f_0 = 100$ Hz and frequency bandwidth $\Delta f = 50$ Hz (cyan) and $\Delta f = 12.5$ Hz (red).

axis depth, $c_a = 1.49$ km/s is the sound speed on the channel axis, $b = 1.0$ km is the thermocline depth scale, $\varepsilon = 0.0057$ is a dimensionless constant, $z_w = 0.1$ km is the width of the Gaussian sound speed perturbation that is centered at depth $z_c = -0.35$ km, and $dc = 0.008$ km/s is the amplitude of the Gaussian perturbation. The two right panels show $\beta(I)$ for the two profiles. The two axes in the middle are mode number axes plotted for two different choices of frequency ($f = 50$ Hz and $f = 100$ Hz) using the simple quantization condition (100). It is clear that the choice of the frequency in this quantization condition does not change the structure of $\beta(I)$, but leads only to the rescaling of the horizontal mode number axis.

Consider a horizontal strip corresponding to a hypothetical energy-containing frequency band, $|f - f_0| \leq \Delta f/2$ (Fig. 7). The two red lines on each diagram correspond to the source with the central frequency $f_0 = 100$ Hz and frequency bandwidth

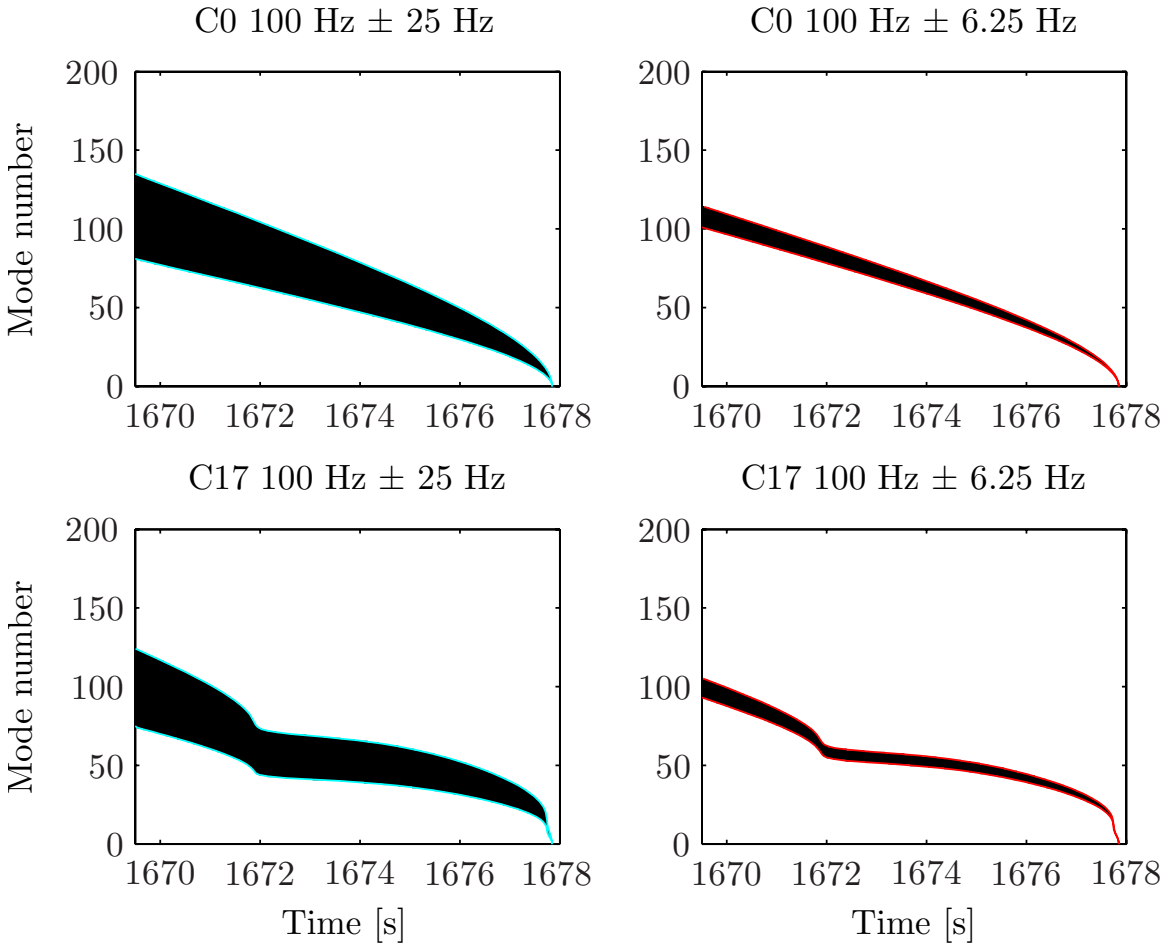


Figure 8. Modal group time spread estimates (simple asymptotic normal mode theory) for C0 profile (upper panels) and C17 profile (lower panels) for the central frequency of the source $f_0 = 100$ Hz and two different bandwidths of 50 Hz (left panels) and 12.5 Hz (right panels).

$\Delta f = 12.5$ Hz; the two cyan lines on each diagram correspond to the frequency bandwidth $\Delta f = 50$ Hz. Assuming the slopes of the dispersion curves are nearly constant across the frequency band of interest, the temporal width of modal group arrival is

$$\Delta t_d = r \left| \frac{\partial S_g}{\partial f} \right|_m \Delta f, \tag{104}$$

in agreement with (103) after one makes use of (98) and (100).

Equation (99) provides a more accurate estimate of $\Delta t_d$. In order to use that

expression one has to find two group slowness values corresponding to intersections of each dispersion curve with lower and upper bound of the frequency band of interest. In order to convert these values into arrival time bounds one has to multiply them by the final range of interest. Figure 8 was constructed in this way for two different environments (C0 and C17), $f_0 = 100$ Hz central frequency of the acoustic source and two different bandwidths $\Delta f = 50$ Hz (left panels) and $\Delta f = 12.5$ Hz (right panels). Note that frequency bounds shown on the dispersion diagram (Fig. 7) by cyan line (for $\Delta f = 50$ Hz) and by red line ($\Delta f = 12.5$ Hz) transform into cyan and red lines, respectively, on modal group time spread diagrams (Fig. 8). The results shown illustrate that the modal group time spread increases with increasing bandwidth and the dependence of the modal group time spread on mode number is largely controlled by the background sound speed structure via the parameter $\beta$. Another example of the dispersion diagram is constructed in Sec. 4.4.

## 4.4 Asymptotic approximations

In this section full wave numerical simulations in a range-independent environment are presented and compared to the wavefield structure predicted by Eqs. (94-98). In particular, we focus on the modal group time spread (95). For numerical simulations C17 profile (Fig. 9) was chosen. Asymptotic analysis is exploited, particularly in the evaluation of $\beta(m, \sigma)$ (98).

The exact expression for the group slowness is [37, 38]

$$S_g(m,\sigma) = \frac{\int \phi_m^2(z,\sigma)\, c^{-2}(z)\, dz}{p_m(\sigma) \int \phi_m^2(z,\sigma)\, dz}. \tag{105}$$

Both this expression and the derivative $dS_g(m,\sigma)/d\sigma$ can be evaluated numerically. Then, using (96) and (97), the modal group time spread (95) can be computed. While this process is not difficult to carry out, it offers no computational advantage over numerically evaluating (90)-(92) directly. In the following we show that the approximate theoretical results (94)-(98) provide an accurate description of modal energy distributions provided $\beta(m,\sigma_0) \neq 0$ and that under most circumstances simple asymptotic expressions for $\beta(m,\sigma_0)$ and $\partial p_r/\partial\sigma$ provide very good approximations.

Using the sound speed profile shown in Fig. 9 the simulations shown in Figs. 10, 11 and 12 were performed to illustrate some important features of the results described above, and to test the validity of some of the approximations made.

Under commonly encountered experimental conditions $\Delta t_d \gg \Delta t_{bw}$. With this assumption dispersion diagrams provide a complete picture of the modal group arrival structure. For the sound speed profile shown in Fig. 9, the dispersion diagram is shown in Fig. 10. That figure was constructed using the asymptotic results (100)-(102); those equations parametrically define a family of curves $S_g(m,\sigma)$. Because Eqs. (100) and (102) are approximate the dispersion diagram shown in Fig. 10 contains some errors which will be discussed below. The reason this diagram differs slightly from the diagram shown before (Fig. 7) is that the surface reflections in the new diagram were treated accurately, that lead to the presence of cusps on this diagram. On the diagram shown in the previous section, the ocean domain was

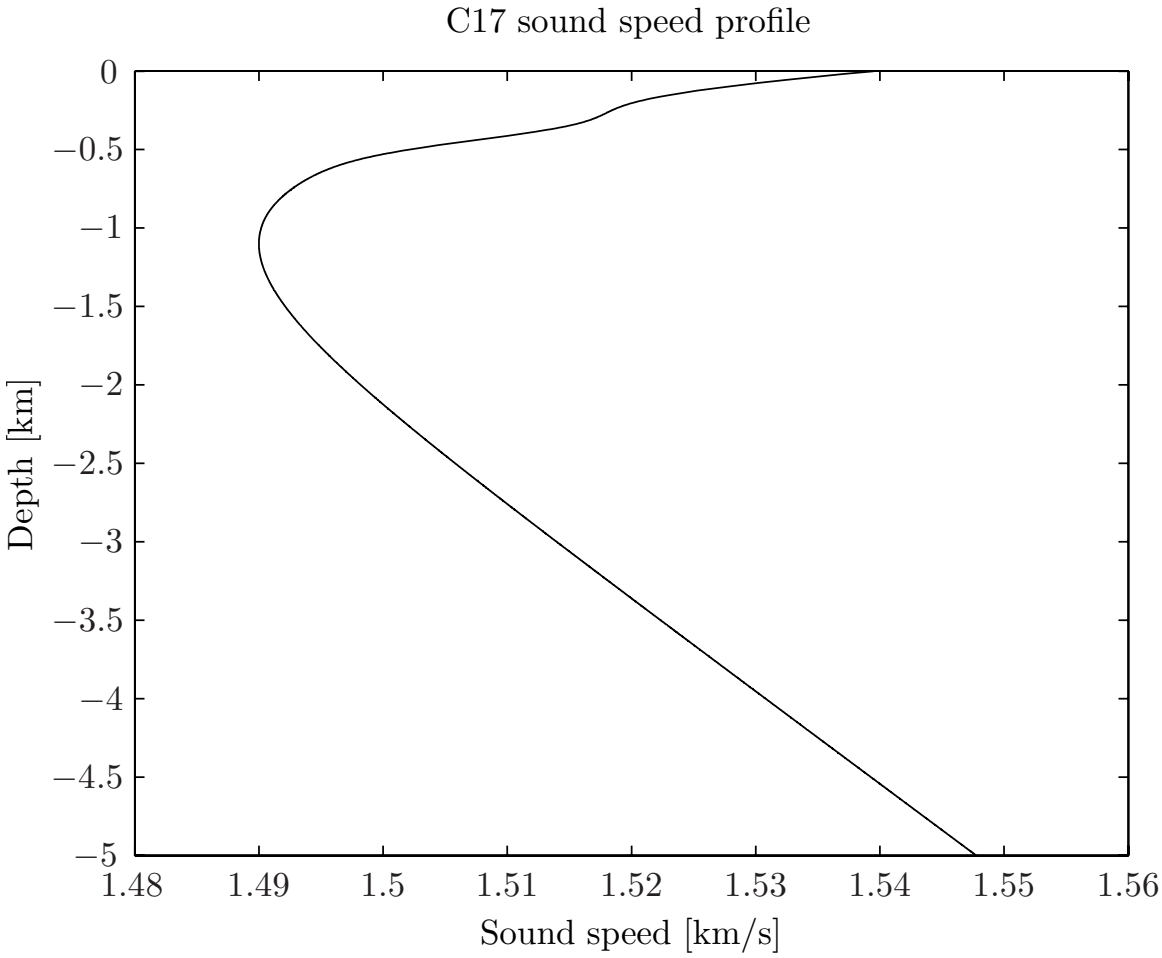


Figure 9. Sound speed profile used in the simulations shown in Figs. 10, 11 and 12.

assumed to be unbounded. An exact dispersion diagram can be constructed from the exact quantization condition (89) (which in general must be found numerically) and (105). Because energy associated with mode number $m$ at frequency $\sigma$ arrives at time $t = S_g(m, \sigma)\, r$, the dispersion diagram shows the temporal structure of the wavefield for all mode numbers in the frequency band of interest.

The upper panel of Fig. 11 shows full wave numerical simulations at $r = 2500$ km with $|f - f_0| \leq \Delta f_c/2$, $f_0 = 75$ Hz, $\Delta f_c = 18.75$ Hz, that correspond to conditions shown in Fig. 10. Here $\Delta f_c$ is the full computational bandwidth. The source spectrum $\bar{s}(\sigma)$ had the shape of a Hanning window, for which $\Delta f \approx \Delta f_c/2$. The simulations

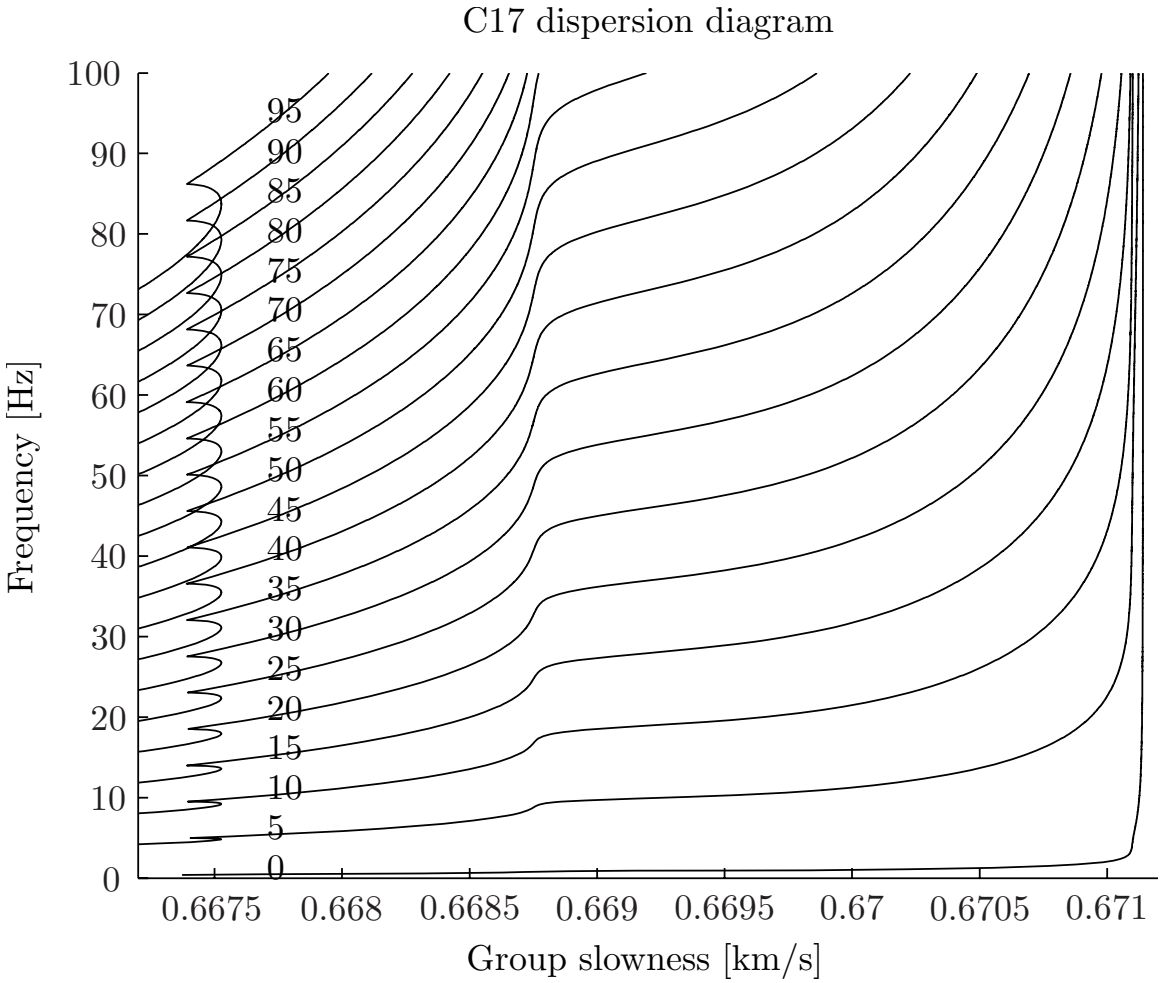


Figure 10. Dispersion diagram for mode numbers $m = 0, 5, 10, ..., 95$ in the environment shown in Fig. 9, computed using the simple asymptotic results, Eqs. (100)-(102).

shown in Fig. 11 were performed by solving the standard parabolic wave equation in a transformed environment $\bar{c}(\bar{z})$ as described in [39, 40]. Loosely speaking, the transformation from $c(z)$ to $\bar{c}(\bar{z})$ is constructed in such a way that the solution to the standard parabolic wave equation in $\bar{c}(\bar{z})$ is the same as the solution to the Helmholtz equation in $c(z)$. In particular, we note that $I(p_r)$, $R(p_r)$ and $T(p_r)$ that appear in (102) and (103) are preserved under the transformation. The reason for making use of this transformation is that it provides a relatively simple means to construct accurate

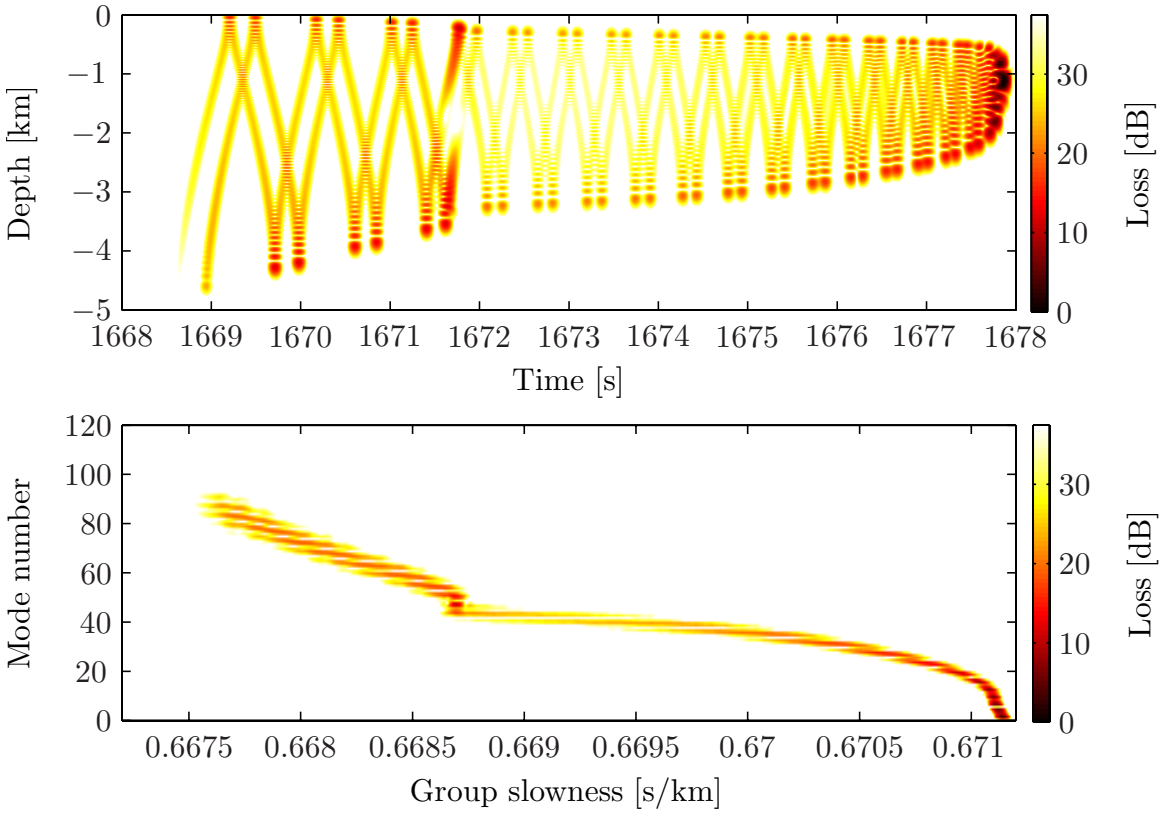


Figure 11. (upper panel) Wavefield intensity, shown on a logarithmic scale, computed in the environment shown in Fig. 9 using an axial source with $f_0 = 75$ Hz and a full computational bandwidth of 18.75 Hz at a range of 2500 km. (lower panel) The corresponding mode-processed wavefield shown using the same time axis $t = S_g r$.

approximate solutions to the Helmholtz equation in a range-dependent environment; simulations in range-dependent environments will be presented in Sec. 6. The lower panel of Fig. 11 shows the mode-processed wavefield $|u_m(t)|^2$ corresponding to the wavefield $|u(z,t)|^2$ shown in the upper panel. Note that the time axis is the same in both plots, $t = S_g r$ with $r = 2500$ km.

An estimate of $\Delta t_m^0$, derived from the wavefield shown in Fig. 11, is plotted as a function of mode number $m$ in Fig. 12. Also on this figure, $\Delta t_{bw}$ (96) and $\Delta t_m^0$, constructed using (95), (96) and (103), are plotted as a function of $m$. The latter curve is labelled simple asymptotic estimate. Note that according to (95) a lower bound on

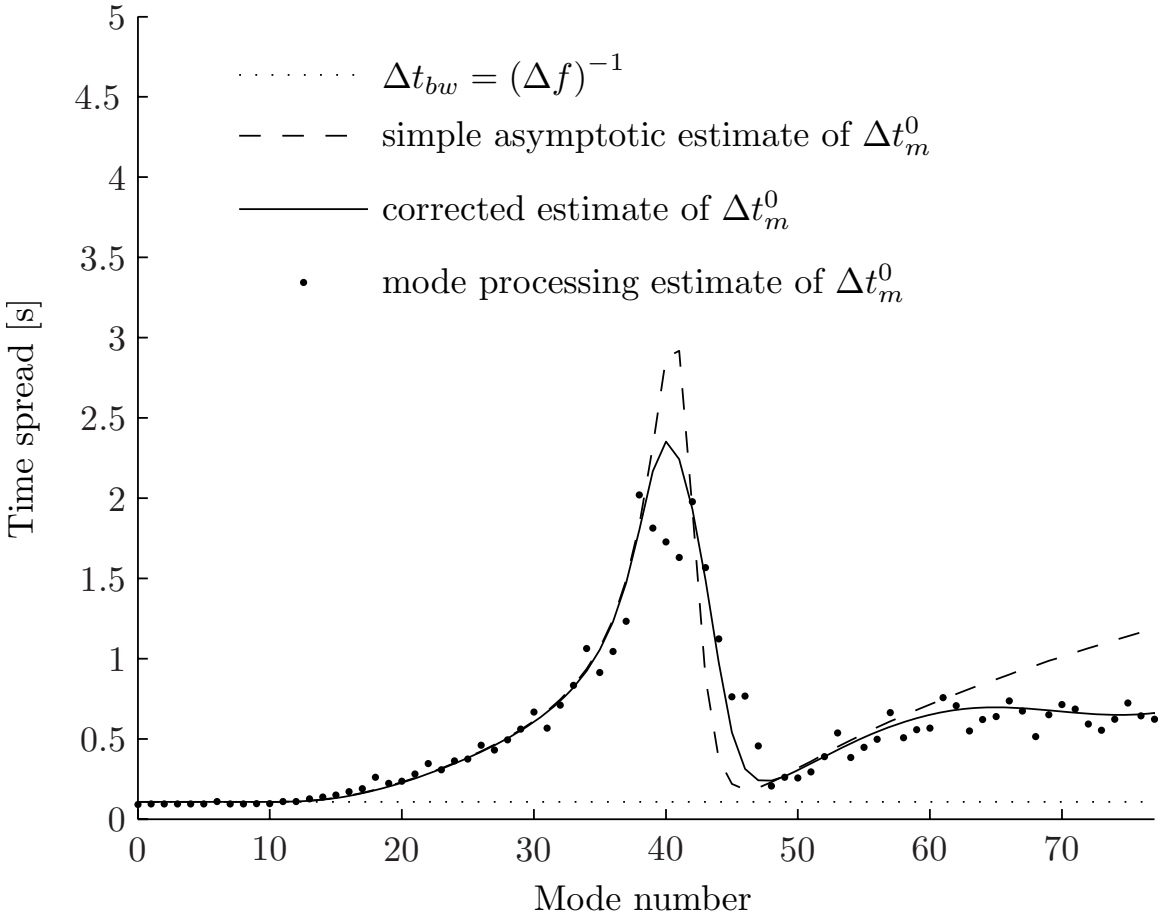


Figure 12. Theoretical and simulation-based estimates of modal group time spreads $\Delta t_m^0$ for the wavefield shown in Fig. 11, corresponding to the dispersion diagram shown in Fig. 10. Theoretical estimates make use of Eqs. (95) and (96). In the simple asymptotic estimate of $\Delta t_m^0$, Eq. (103) was used to compute $\Delta t_d$. Eqs. (99), (109) and (110) were used to compute $\Delta t_d$ in the corrected estimate of $\Delta t_m^0$.

$\Delta t_m^0$ is predicted to be $(\Delta f)^{-1}$. Overall, the agreement between simple theory ((95), (96) and (103)) and estimates of $\Delta t_m^0$ derived from simulations is seen to be good, but a systematic deviation between simulation-based estimates of $\Delta t_m^0$ and the simple theoretical prediction of $\Delta t_m^0$ is seen in two bands of mode numbers. First, consider $39 \lesssim m \lesssim 46$. For this band of $m$ the slopes of the dispersion curves in the 65 Hz to 85 Hz frequency band seen in Fig. 10 are seen to be nonconstant. As a result, Eqs. (97) and (103), which assume a constant slope, give a poor approximation to $\Delta t_d$. To

correct this problem one needs only replace Eq. (103) by Eq. (99), which gives good agreement with simulation-based estimates of $\Delta t_m^0$ even when the simple asymptotic expression (102) is used to compute $S_g$. The second band of mode numbers where a systematic deviation between theory and simulation-based estimates of $\Delta t_m^0$ is seen in Fig. 12 is $60 \lesssim m \lesssim 75$. This range of $m$ corresponds to modes with upper turning depths near the surface. The cause of the misfit between simulations and the simple theory for these mode numbers is the use of (103) which, in turn, depends on (100)-(102). Those equations do not correctly describe near-surface-reflecting modes. It is possible, however, to derive corrections within an asymptotic framework to those equations. This issue will now be addressed.

Corrections to (100)-(102) for near-grazing (surface and/or bottom) modes have previously been described by many authors. A straightforward and quite general approach to addressing problems of this type is to note that (100) is a special case of a general expression (see e.g., [22])

$$\sigma J\left(p_m\right) = m - \frac{\varphi_u + \varphi_l}{2\pi}. \tag{106}$$

Here $J\left(p_m\right)$ has the same form as $I\left(p_m\right)$ in (101) except that the lower and upper bounds on the integral coincide with the modal turning depths, which may coincide with one or both of the boundaries, while $\varphi_u$ and $\varphi_l$ are the phases of the upper and lower reflection coefficients, $R_u$ and $R_l$, respectively. For modes with upper and lower turning depths far from the boundaries $R_u = R_l = -i$, and (106) reduces to (100).

In the following we focus on near-surface-grazing modes in an environment with

a deep sound speed excess, so $R_l = -i$ and $R_u$ transitions smoothly from $-i$ ($c(\hat{z}) \ll c(0)$, non-surface-reflecting modes) to $-1$ ( $c(\hat{z}) \gg c(0)$, surface-reflecting modes). For the latter class of modes (106) reduces to $\sigma J(p_m) = m + \frac{3}{4}$. The desired reflection coefficient, with the properties just described was derived originally by Murphy and Davis [41]. For $c(\hat{z}) < c(0)$ (RR modes with upper turning depths close to the surface)

$$R_u = \exp\left[i\left(-\frac{\pi}{2} - 2\tan^{-1}\frac{\mathrm{Ai}(S)}{\mathrm{Bi}(S)}\right)\right], \tag{107}$$

where

$$S = \left[\frac{3}{2}\sigma\int_{\hat{z}}^{0}\sqrt{p_r^2 - c^{-2}(z)}dz\right]^{2/3}. \tag{108}$$

(These equations require some modification for surface-reflecting modes, $c(\hat{z}) > c(0)$, but this will not be discussed here.) With $R_l = -i$ and $R_u$ given by (107), (106) becomes

$$\sigma I(p_m) = m + \frac{1}{2} + \frac{1}{\pi}\tan^{-1}\left[\frac{\mathrm{Ai}(S)}{\mathrm{Bi}(S)}\right]. \tag{109}$$

Note that (109) reduces to (100) for large $S$ (upper turning depth many wavelengths away from the surface) and to $\sigma I = m + \frac{2}{3}$ for a surface grazing mode ($S = 0$). We note also that Eq. (109) is a special case of Eq. (5.21) in reference [31] with the assumption that ocean bottom is many wavelengths away from the lower modal turning depth. Noting that $k_m = \sigma p_m$ and $S_g = \partial k_m / d\sigma$, differentiation of (109) with

respect to $\sigma$ (with $m$ fixed) gives

$$S_g\left(p_m,\sigma\right)=\frac{T\left(p_m\right)+2\left(\frac{3}{2}\right)^{-1/3}\kappa\sigma^{-1/3}\left(\int_{\hat{z}}^{0}\sqrt{p_m^2-c^{-2}\left(z\right)}dz\right)^{-1/3}\int_{\hat{z}}^{0}\frac{c^{-2}(z)dz}{\sqrt{p_m^2-c^{-2}(z)}}}{R\left(p_m\right)+2p_m\left(\frac{3}{2}\right)^{-1/3}\kappa\sigma^{-1/3}\left(\int_{\hat{z}}^{0}\sqrt{p_m^2-c^{-2}\left(z\right)}dz\right)^{-1/3}\int_{\hat{z}}^{0}\frac{dz}{\sqrt{p_m^2-c^{-2}(z)}}}, \tag{110}$$

where

$$\kappa=-\frac{1}{\pi\left(\mathrm{Ai}^2\left(S\right)+\mathrm{Bi}^2\left(S\right)\right)}. \tag{111}$$

Elimination of $p_m$ from (109) and (110) allows the construction of a dispersion diagram.

An estimate of $\Delta t_m^0$, constructed using (109) and (110) is plotted as a function of mode number $m$ in Fig. 12 with solid line. The agreement between the corrected theory and estimates of $\Delta t_m^0$ derived from simulations is seen to be excellent even for modes with turning depths close to the pressure release surface. Equations (108)-(111) generalize Eqs. (100)-(102) for near-surface-grazing modes with lower turning depths far from the water/bottom interface. Modes of this type are observed in most single-minimum deep ocean sound channels with a deep sound speed excess, including the LOAPEX environment. Although the validity of Eqs. (108)-(111) is restricted to this class of modes, the type of analysis that we have presented can easily be generalized to treat other classes of modes for which Eqs. (100)-(102) are invalid.

The modal group time spread diagrams constructed with the use of simple asymptotic theory (Fig. 8) can also be improved by making use of Eqs. (108)-(111). Fig-

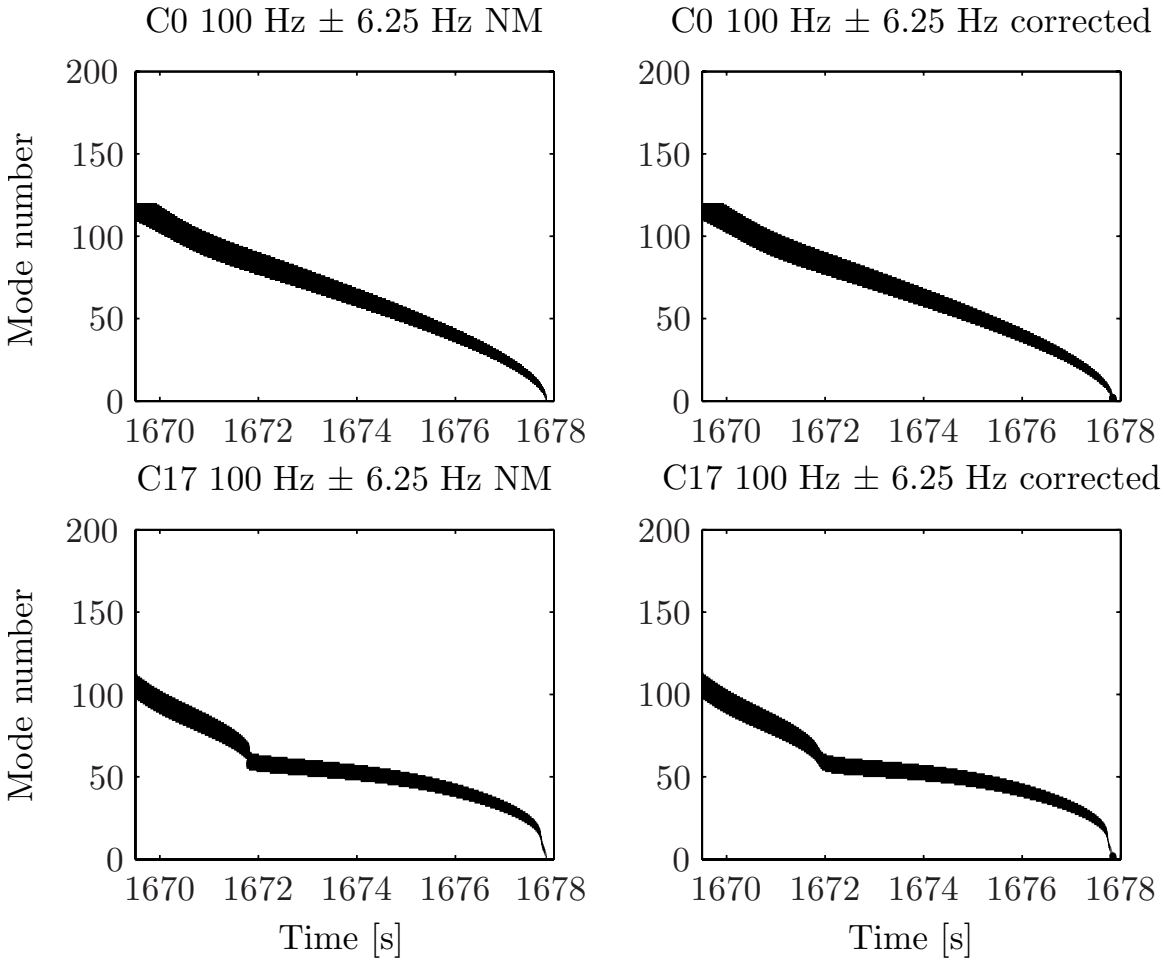


Figure 13. Modal group time spread estimates for C0 profile (upper panels) and C17 profile (lower panels) with the central frequency of the source $f_0 = 100$ Hz and bandwidth of 12.5 Hz computed from full wave normal mode simulations (left panels) and corrected asymptotic normal mode theory (right panels).

ure 13 compares the dispersion diagrams constructed in two environments (C0 and C17), obtained by two different methods. The left panels were produced from a full wave normal mode solution computed using normal mode code PROSIM [5]; the right panels were computed using improved theoretical estimates with the use of Eqs. (108-111). It is seen that the agreement between modal group time spreads computed from dispersion diagrams constructed with the use of simple asymptotic theory (Fig. 8) and exact full wave numerical simulations (left panels of Fig. 13)

is not very good for modes with turning depth close to the ocean surface. However, the agreement between full wave simulations and results obtained from asymptotic theory with correction derived in this section (right panels of Fig. 13) is significantly improved.

## 4.5 The scattering-induced contribution to modal group time spreads

The results presented in the previous section need to be amended to account for the mode coupling that occurs in realistic range-dependent ocean environments. We focus here on environments consisting of a range-independent background on which a highly structured range-dependent perturbation, due for example to internal waves, is superimposed. Mode coupling is then predominantly local in mode number. The predominance of nearest neighbor mode coupling is discussed in [22]. In [42] the same authors show that to an excellent approximation ray scattering can be described by a diffusion process in action $I$. But the quantization condition (100) (or some generalization thereof, such as (109)) shows that as acoustic energy diffuses in action in the ray description it diffuses (taking discrete steps) in mode number in the mode description. This is an aspect of ray-mode duality that, like other aspects, is particularly transparent when asymptotic mode results, such as (100), are used. With the above comments as background, we will treat $m$ and $I$ as interchangeable labels in the following discussion, keeping in mind that a quantization condition connects $m$ and $I$. In the presence of mode coupling the total group delay of modal energy

that has been scattered among mode numbers $m_i$, $i = 1, ..., n$ can be written

$$t_g = \sum_{i=1}^{n} S_g\left(m_i, \sigma_0\right) \Delta r_i, \tag{112}$$

where $\sum_{i=1}^{n} \Delta r_i = r$, the total range. Expanding $S_g$ in a Taylor series, making use of (98) and $R = -2\pi dI/dp_r$, gives

$$t_g \approx S_g\left(m_0, \sigma_0\right) r + 2\pi \frac{\beta\left(I_0\right)}{R\left(I_0\right)} \sum_{i=1}^{n} \left(I_i - I_0\right) \Delta r_i. \tag{113}$$

Convenient choices for $I_0$ are the action at $r = 0$ or the action at the final range, and $I_0 = \left(m_0 + 1/2\right)/\sigma_0$ (or some generalization thereof). If $\Delta r_i$ is taken to be constant (so $n\Delta r = r$), then

$$\delta t_s = 2\pi \frac{\beta\left(I_0\right)}{R\left(I_0\right)} \Delta r \sum_{i=1}^{n} \left(I_i - I_0\right) \tag{114}$$

is the scattering-induced arrival time perturbation for acoustic energy whose forward or reversed action history is $I_0, I_1, ..., I_n$. (The action history is more convenient than the mode number history.) In (114) $I_i$ is the action after the $i$-th scattering event

$$I_i = I_0 + \sum_{j=1}^{i} \delta I_j. \tag{115}$$

Assume that $\delta I_j$ is a delta-correlated zero-mean random variable,

$$\langle \delta I_j \rangle = 0, \langle \delta I_j \delta I_k \rangle = \langle \left(\delta I\right)^2 \rangle \delta_{jk}. \tag{116}$$

Let $\Delta I_n = I_n - I_0$. Then $\langle (\Delta I_n)^2 \rangle = n \langle (\delta I)^2 \rangle$ and, for large $n$, $\langle \left( \sum_{i=1}^{n} \Delta I_n \right)^2 \rangle \approx n^3 \langle (\delta I)^2 \rangle / 3$. Thus, it follows from (114) with $\Delta t_s = 2\sqrt{\pi} \langle (\delta t_s)^2 \rangle^{1/2}$ that

$$\Delta t_s = 4\pi^{3/2} \frac{|\beta(I_0)|}{R(I_0)} \left( \frac{B}{3} \right)^{1/2} r^{3/2}, \tag{117}$$

where $B = \langle (\delta I)^2 \rangle / \Delta r$. Note also that, in terms of $B$, $\langle (\Delta I(r))^2 \rangle = Br$, which can be taken as the definition of $B$ in the continuum limit. It is important to keep in mind that in a scattering environment of the type considered, any wavefield contains scattered energy corresponding to many action histories. Assuming each such action history is independent, $\langle (\delta t_s)^2 \rangle^{1/2}$ is the rms value of the corresponding distribution of travel time perturbations at range $r$. The quantity $\Delta t_s$ is taken to be $2\sqrt{\pi}$ times the standard deviation of this distribution so that this quantity, like $\Delta f$ and $\Delta t_m^0$, is defined as the full width of the $\delta t_s$ distribution at the half-amplitude points. (Recall that 0.5 is an approximation to $e^{-\pi/4} \approx 0.456$ and note that wavefield intensity is assumed to be proportional to the action distribution.) We shall refer to (117) as the scattering-induced contribution to a modal group time spread. It should be noted that a formula similar to Eq. (117) was derived in a different way by Virovlyansky [43] and by Virovlyansky *et al.* [44].

The assumption of delta-correlated action scattering events has been shown [45, 42] to be an excellent approximation at long-range in deep ocean environments. Using results from the study of stochastic differential equations, scattering in the continuum limit was treated directly in those studies. An advantage of that approach is that it allowed the authors to correctly treat near-axial (where $I$ is close to 0) scattering.

The authors solved this problem by pointing out that the relevant Fokker–Planck equation for $\Delta I\,(r)$ admits an exact solution for a reflecting boundary at $I = 0$. It is important to emphasize that the results presented above – Eqs. (116) and (117), in particular – are not valid for $I$ close to zero (near-axial modes) as they fail to enforce the condition $I \geq 0$.

At the end of Sec. 4.5 an extension of Eq. (117) that accounts for modes with turning depths close to the sound channel axis will be discussed. For this purpose it is instructive to present another derivation of Eq. (117) with the approach used in [43]. This derivation is based on the continuous model of scattering of action $I$ along the propagation path. The underlying assumption of this model is that value of action $I$ is described by a Brownian motion (or random walk) process along the propagation path. The statistics of this process is well-known and application of these results allows to obtain an estimate for the scattering-induced contribution to the modal group time spreads in the simplest case.

Let $P\,(I, r|I_0, r_0)$ be the probability density function (pdf) of the distribution of action as a function of range with the condition that at range $r_0$ the value of action was $I_0$. Then according to [43, 46]

$$P\,(I, r|I_0, r_0) = \frac{1}{\sqrt{2\pi B\,(r - r_0)}} \mathrm{e}^{-\frac{(I-I_0)^2}{2B(r-r_0)}}. \tag{118}$$

Let $x = I - I_0$ and assume that $r_0 = 0$, then

$$P\,(x, r) = \frac{1}{\sqrt{2\pi Br}} \mathrm{e}^{-\frac{x^2}{2Br}}. \tag{119}$$

Consider two random processes $x_1(r_1)$ and $x_2(r_2)$ with the probability density function given by (119). The joint pdf of these two processes can be expressed as

$$P(x_1, r_1, x_2, r_2) = P(x_1, r_1) P(x_2 - x_1, r_2 - r_1) = \frac{1}{2\pi B\sqrt{r_1(r_2 - r_1)}} \mathrm{e}^{\frac{-x_1^2(r_2-r_1)-r_1(x_2-x_1)^2}{2Br_1(r_2-r_1)}}. \tag{120}$$

The usefulness of the last expression is that it allows one to compute the covariance function of the Brownian motion,

$$C(r_1, r_2) = \int_{-\infty}^{\infty}\int_{-\infty}^{\infty} x_1 x_2 P(x_1, r_1, x_2, r_2) = B\min(r_1, r_2). \tag{121}$$

The variance of this process is then simply

$$\sigma_I = \sqrt{C(r, r)} = \sqrt{Br}. \tag{122}$$

The total group delay of modal energy can be written (recall (112))

$$t_g = \int_0^r S_g(m(I(r')); \sigma_0)\, dr'. \tag{123}$$

Making use of the Taylor series expansion, $S_g(I) \approx S_g(I_0) + \frac{2\pi\beta(I_0,\sigma_0)}{R(I_0)}x$, the expression for the group delay of modal energy is

$$t_g \approx t_{g_0} + \frac{2\pi\beta(I_0, \sigma_0)}{R(I_0)} \int_0^r x(r')\, dr'. \tag{124}$$

The first term in the latter expression is the average arrival time of a modal group.

The second term, which is a correction to the modal group arrival time is recognized as the so-called integrated Brownian motion process. A modal group time spread is equal to the variance of the process described by the second term in the Eq. (124). It can be shown that covariance of this integrated Brownian motion process is

$$\tilde{C}\left(r_1, r_2\right) = B \int_0^{r_1} \int_0^{r_2} \min\left(r_1, r_2\right) = B\left(\frac{r_1^2 r_2}{2} - \frac{r_1^3}{3}\right). \tag{125}$$

The variance of this process is

$$\sigma_t = \sqrt{B/3} r^{3/2}, \tag{126}$$

and therefore for the modal group time spread we obtain

$$\Delta t_s = 2\sqrt{\pi}\langle(\delta t_s)^2\rangle^{1/2} = \frac{2\sqrt{\pi} \times 2\pi \left|\beta\left(I_0\right)\right|}{R\left(I_0\right)}\sigma_t = \frac{2\sqrt{\pi} \times 2\pi \left|\beta\left(I_0\right)\right|}{R\left(I_0\right)}\left(\frac{B}{3}\right)^{1/2} r^{3/2}, \tag{127}$$

which is identical to the Eq. (117).

A final remark concerning Eq. (117) is that this expression is expected to be a good approximation only when $\beta\left(I_0\right)$ is representative of $\beta$-values for all scattered energy that at range $r$ has $I = I_0$. This condition will be satisfied if $\beta\left(I\right)$ (or $\beta\left(m\right)$ in the relevant frequency band) is a slowly varying function. When this assumption is not satisfied, an improved – relative to (117) – estimate of $\delta t_s$ should result from replacing (114) by

$$\delta t_s = \frac{2\pi}{R\left(I_0\right)} \Delta r \sum_{i=1}^{n} \beta\left(I_i'\right)\left(I_i - I_0\right). \tag{128}$$

This comment follows from the observations that: 1) equation (113) is exact – by the mean value theorem – if, for each term in the sum, $\beta(I_0)/R(I_0)$ is replaced by $\beta(I_i')/R(I_i')$ for some $I_i'$ between $I_0$ and $I_i$; and 2) variations in $R(I)$ are negligible compared to variations in $\beta(I)$. The value of $I_i'$ is not known a priori, but it might be possible to parameterize $\beta(I_i')$ in such a way that (128) can be simplified in cases where (114) is a poor approximation.

Because $\Delta t_s$ (117) is independent of the deterministic contributions, $\Delta t_{bw}$ and $\Delta t_d$, it is natural to assume that the deterministic and stochastic contributions combine in quadrature, so with the aid of (95) the total modal group time spread is

$$\Delta t_m(r) = \sqrt{\Delta t_{bw}^2 + \Delta t_d^2 + \Delta t_s^2}. \tag{129}$$

The assumption that the three contributions to $\Delta t_m$ combine in quadrature will be revisited below.

As was discussed above, Eqs. (116) and (117) are not valid for $I$ close to zero (near-axial modes). However, using results from the study of stochastic differential equations, scattering in the continuum limit was treated directly by Virovlyansky [43] and Virovlyansky *et al.* [42]. The random walk description of the scattering process remains valid in the presence of the reflecting boundary at $I = 0$, however, the pdf of $I$ changes to

$$P(I, r|I_0, r_0) = \frac{1}{\sqrt{2\pi B(r - r_0)}} \left\{ \mathrm{e}^{-\frac{(I-I_0)^2}{2B(r-r_0)}} + \mathrm{e}^{-\frac{(I+I_0)^2}{2B(r-r_0)}} \right\}. \tag{130}$$

Again we assume $r_0 = 0$, and then the pdf becomes

$$P\left(I, r|I_0, 0\right) = \frac{1}{\sqrt{2\pi Br}} \left\{ \mathrm{e}^{-\frac{(I-I_0)^2}{2Br}} + \mathrm{e}^{-\frac{(I+I_0)^2}{2Br}} \right\}. \tag{131}$$

Similarly, the joint probability density function for two random processes $I_1\left(r_1\right)$ and $I_2\left(r_2\right)$ is

$$P\left(I_1, r_1, I_2, r_2, I_0\right) = P\left(I_2, r_2|I_1, r_1\right) P\left(I_1, r_1\right), \tag{132}$$

and the correlation function is

$$C\left(r_1, r_2\right) = \left\langle I\left(r_1\right) I\left(r_2\right)\right\rangle = \int_0^\infty \int_0^\infty dI_1 dI_2 I_1 I_2 P\left(I_1, r_1, I_2, r_2, I_0\right) \tag{133}$$

As was shown before, the second moment of the integrated random walk process is directly related to the scattering-induced modal group time spreads. The second moment can be written as

$$\tilde{\sigma}_t^2 = \int_0^r dr_1 \int_0^r dr_2 C\left(r_1, r_2\right). \tag{134}$$

Unfortunately, it does not seem possible to obtain any simple analytic expression for modal group time spreads in the presence of the reflecting boundary at $I = 0$. Therefore, the estimates have to be done numerically. Virovlyansky *et al.* [42] offered an elegant way to avoid this problem by solving the original stochastic equations numerically; if at some step $I < 0$, then $I$ is replaced by $-I$.

## 4.6 Sensitivity of modal group time spreads to the details of the perturbation field and background sound speed structure

It is useful to discuss the relative importance of the background sound speed profile structure and of the perturbation field on modal group time spreads. For this purpose two different sound speed perturbation fields were constructed. The first one is a homogeneous isotropic field (HIS) which is a single-scale gaussian perturbation field. This field is completely unrealistic in the ocean environment. Another perturbation field is constructed with the use of internal-wave model (IW), which is a realistic model that accounts for anisotropy, inhomogeneity and the multiple scale (power law) spectrum. The details of this field will be discussed further in this section.

Figure 14 shows the statistics of the HIS and IW perturbation fields. These fields were constructed in such a way that the total perturbation energy in them is the same. The main qualitative difference between the two is that the IW field is mostly present in the upper few hundred meters in the ocean, whether HIS perturbation field is distributed uniformly throughout the ocean column.

Figure 15 shows modal group time spreads computed from numerically simulated fields with two different background sound speed profiles used (C0 and C17) with two different range-dependent fields (HIS and IW) superimposed. The transmission range was chosen to be 2500 km and the acoustic source was placed on the sound channel axis at 1.1 km depth. It is clear from these simulations that the scattering-induced contribution to modal group time spreads is largely controlled by the background sound speed structure via mode based waveguide invariant parameter $\beta$, which is

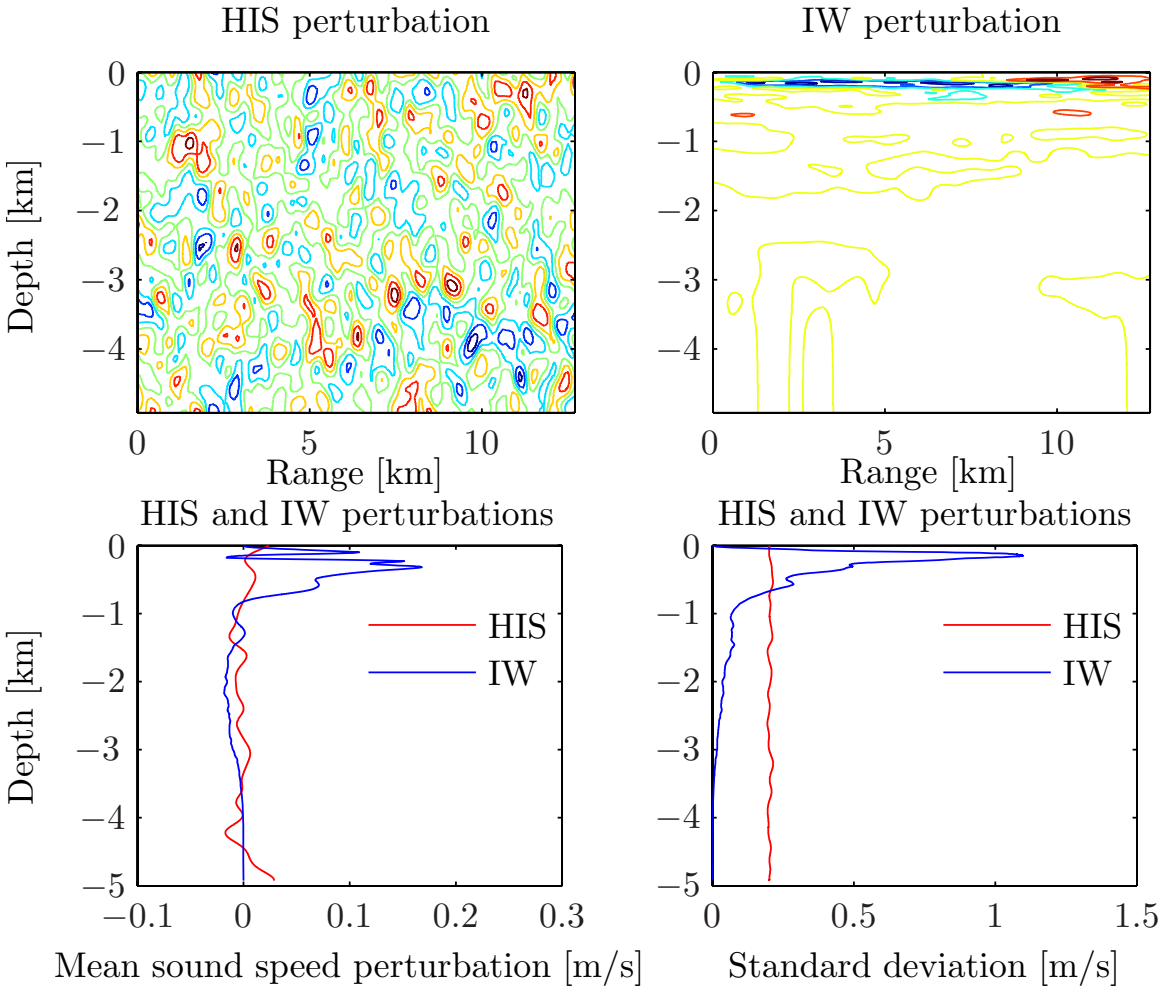


Figure 14. Homogeneous isotropic perturbation structure (upper left panel), internal-wave-induced perturbation structure (upper right panel), mean sound speed value in both perturbations (lower left panel) and standard deviation of the sound speed in both perturbations (lower right panel).

consistent with the results obtained in the prevous section (Eq. (117)), while these diagrams show very little sensitivity to the details of the perturbation field.

## 4.7 Simulations of modal group time spreads for an axial acoustic source

Now full-wave numerical simulations in an environment similar to the LOAPEX environment are presented. The purpose of presenting these simulations is both to test the approximate theoretical predictions that we have presented and to provide

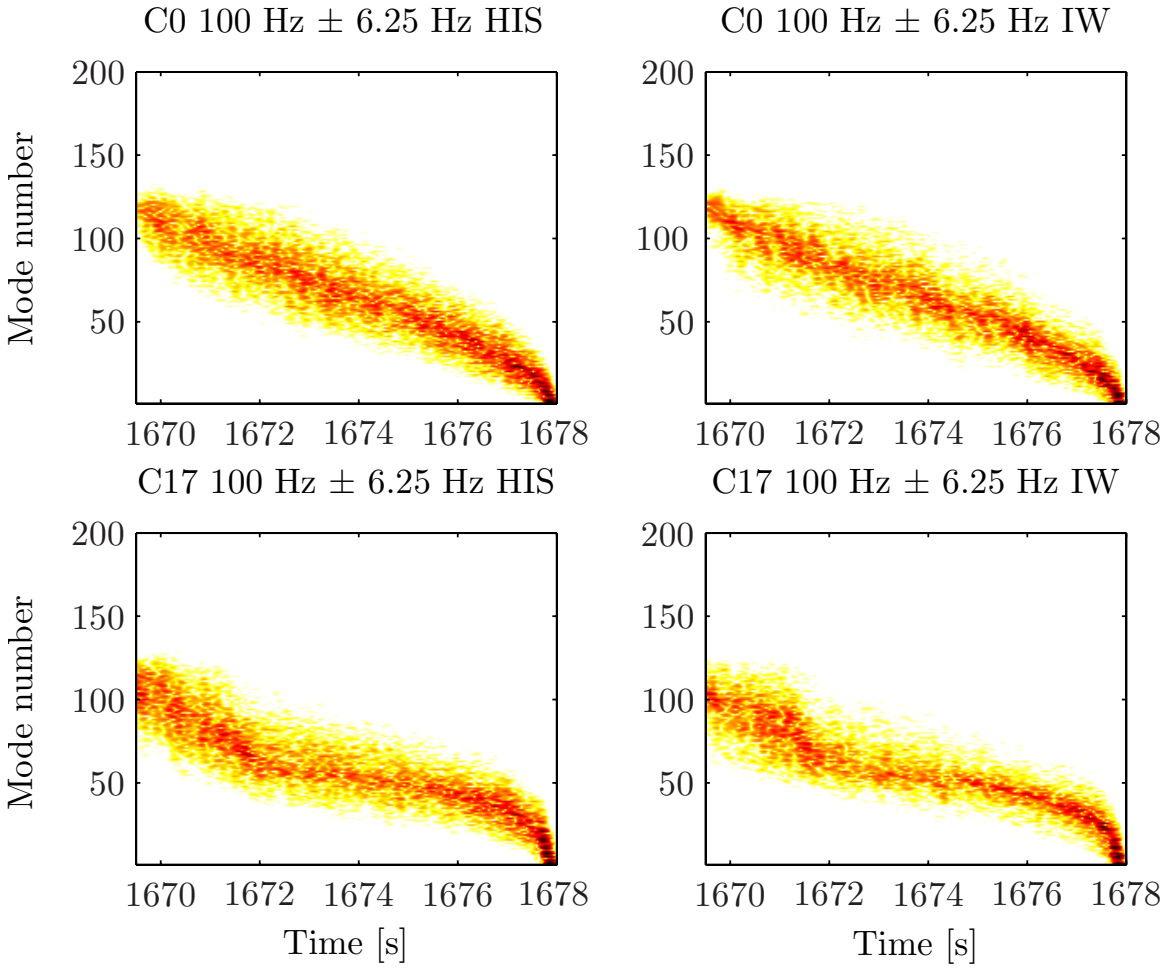


Figure 15. Distribution of energy among the modes obtained from PE simulations for C0 profile (upper panels) and C17 profile (lower panels) with two different perturbations superimposed: HIS (left panels) and IW (right panels).

a foundation for the interpretation of the LOAPEX measurements (which will be presented later). The LOAPEX measurements were made at ranges between approximately 50 km and 3200 km. For this reason we emphasize in this section the evolution in range of modal group time spreads.

Before presenting wavefield simulations we note that a simple consequence of Eq. (129) and the observation that $\Delta t_{bw}$, $\Delta t_d$ and $\Delta t_s$ grow like $r^0$ (96), $r$ (97), (103) or (99) and $r^{3/2}$ (117), respectively, is that plots of $\Delta t_m\,(r)$ are of one of two types, as

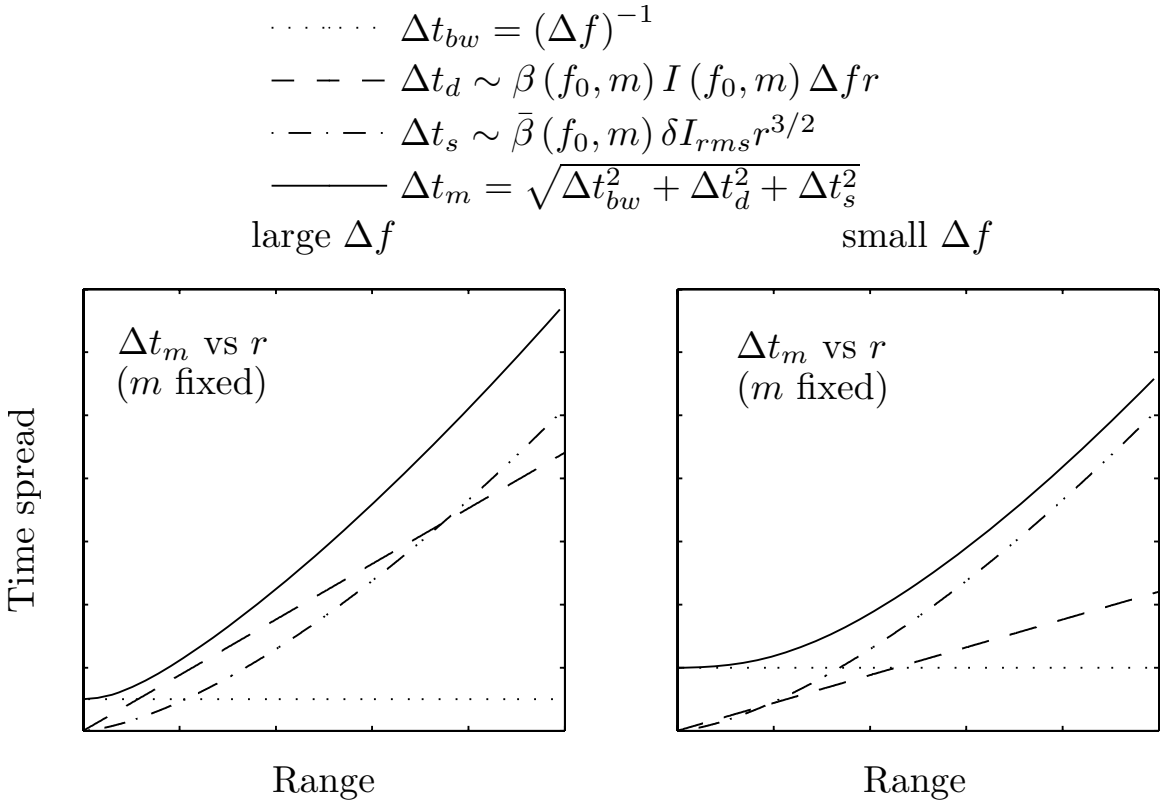


Figure 16. Schematic diagram showing $\Delta t_{bw}$, $\Delta t_d$, $\Delta t_s$ and $\Delta t_m$ vs $r$ under conditions for which there is (left panel) and is not (right panel) a range of $r$ values over which $\Delta t_d$ is the dominant term. The following parameter values, which are typical of deep ocean conditions, were used to construct these plots: $f_0 = 75$ Hz, $m = 56$, $\beta = -0.117$, $I = 0.12$ s, $R = 53.37$ km, $B = 3.3 \times 10^{-7}\,\mathrm{s}^2/\mathrm{km}$, large $\Delta f = 20$ Hz (left panel) and small $\Delta f = 10$ Hz (right panel). The maximum range and time spread are 1000 km and 0.7 s, respectively.

illustrated in Fig. 16. At short ranges $\Delta t_{bw}$ is always the dominant contributor to $\Delta t_m$ and at large ranges $\Delta t_s$ is always the dominant contributor. There may, but need not, be an intermediate range of $r$ values where $\Delta t_d$ is the dominant contributor. Whether this regime is present is controlled largely, but not exclusively, by $\Delta f$: large $\Delta f$ favors small $\Delta t_{bw}$ and large $\Delta t_d$. Thus large $\Delta f$ favors the presence of $\Delta t_d$-dominant regime. A signal processing option is to reduce $\Delta f$, but this is generally not desirable, as reducing $\Delta f$ reduces the relative importance of the deterministic dispersive contribution $\Delta t_d$ to the total time spread. The deterministic dispersive

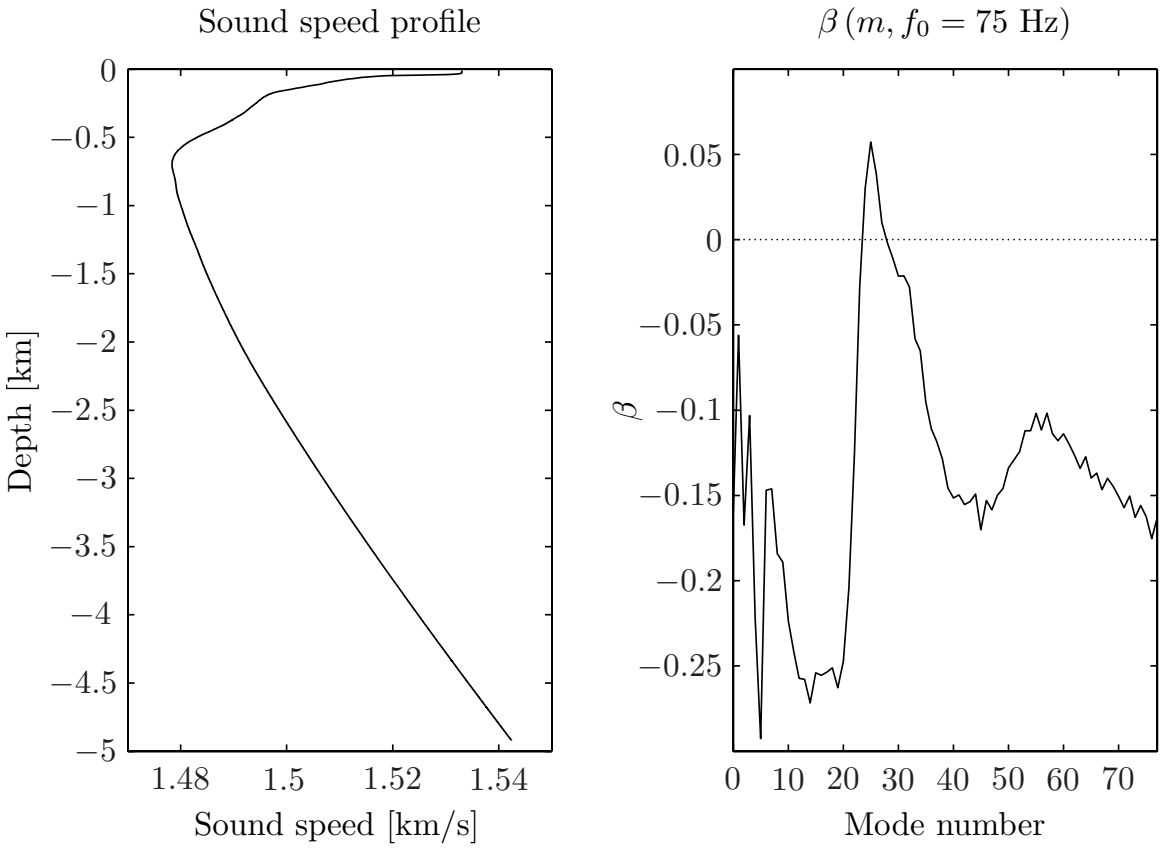


Figure 17. (left panel) Background sound speed profile used in the wavefield simulations shown in Figs. 18-20. (right panel) Corresponding plot of $\beta\,(m; \sigma_0)$ with $\sigma_0/2\pi = f_0 = 75$ Hz.

and the scattering-induced contributions depend on the environment and are mode number dependent. Thus, it is possible that in the same wavefield both types of behavior seen in Fig. 16 are simultaneously present for different groups of mode numbers.

To test our theoretical prediction, and the validity of the associated approximations, wavefield simulations have been performed at many ranges in an environment similar to the LOAPEX environment. The source center frequency was $f_0 = 75$ Hz and the computational bandwidth was $\Delta f_c = 37.5$ Hz, corresponding to an effective bandwidth of $\Delta f = 18.75$ Hz. In this section we focus on axial source transmissions,

so the source depth used in the simulations was 800 m. The background sound speed profile $c(z)$ and corresponding plot of $\beta(m, f_0)$ are shown in Fig. 17. A fairly realistic internal-wave-induced sound speed perturbation $\delta c(z, r)$ [47] was superimposed on the background $c(z)$ in the simulations. The parameters of the IW model are the following: maximum IW mode number $j_{\max} = 30$, maximum horizontal wavenumber $k_{\max} = \frac{2\pi}{1.0}$ km$^{-1}$ $\approx 6.28$ km$^{-1}$, and the minimum horizontal wavenumber $k_{\min} = \frac{2\pi}{3276.8}$ km$^{-1}$ $\approx 2 \times 10^{-3}$ km$^{-1}$. The sound speed perturbation has a sharp peak at 50 m depth where $\delta c \approx 2.3$ m/s, and then decays rapidly to $\delta c \approx 0.5$ m/s at 200 m depth and $\delta c \approx 0.1$ m/s at 1 km. The assumed strength of the internal wave field used in the simulations shown was the nominal Garrett-Munk value, $E = E_{GM}$. Figure 18 shows sample wavefields in $(z, t)$ at three ranges, together with the corresponding mode-processed fields in $(m, t)$ where $t = S_g r$. By performing similar processing on wavefields at many ranges, $\Delta t_m(r)$ for all mode numbers can be estimated. Three such plots for $m = 17$, 25 and 56 are shown in Fig. 19. For the simulations shown in Figs. 18 and 19 the source was located on the sound channel axis.

The construction of Fig. 19 requires some explanation. Consistent with the full width at half-amplitude criterion used earlier to define the widths of approximately Gaussian distributions, $\Delta t_m$ was estimated from wavefields of the type shown in Fig. 18 as the half-difference in time between the latest and earliest points whose intensity is 27 dB below the peak intensity (which is equivalent to the reduction by $e^{-\pi}$ in the amplitude relative to the peak). As noted earlier, $\Delta f$ was estimated in the same way giving, to a good approximation $\Delta f = \Delta f_c/2$. The dispersive contribution was computed using Eq. (99). (For mode numbers $20 \lesssim m \lesssim 30$ Eq. (99) is a much better

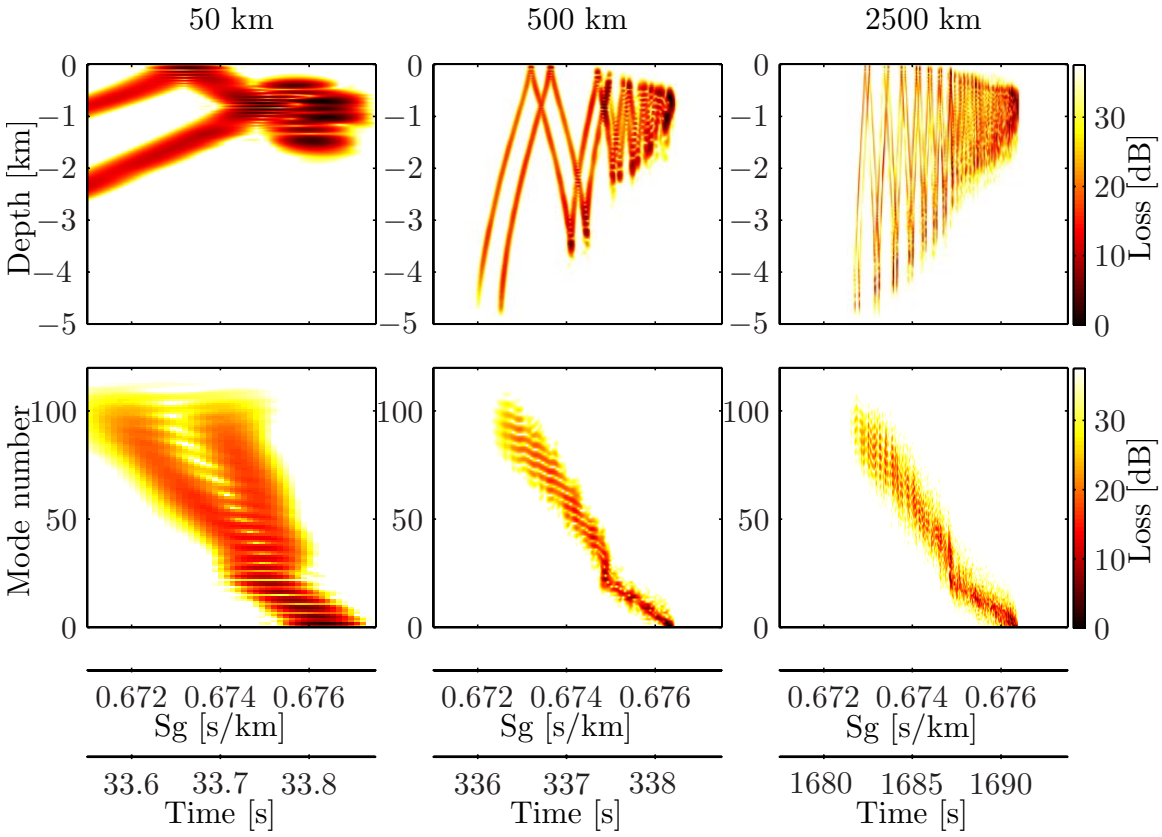


Figure 18. Simulated wavefields with $f_0 = 75$ Hz, $\Delta f_c = 37.5$ Hz at three ranges in the environment shown in Fig. 17, with an internal-wave-induced sound speed perturbation superimposed. (upper panels) Wavefield intensity in $(z, t)$. (lower panels) Corresponding mode-processed fields in $(m, t)$ where $t = S_g r$.

estimate of $\Delta t_d$ than Eq. (103). Outside of this band Eq. (103) gives essentially the same estimate. Only for mode numbers greater than approximately 70 is the near-surface-grazing correction discussed in Sec. 4.4 important.) The scattering-induced contribution $\Delta t_s$ was computed using Eq. (117). The parameter $B$ in (117) was estimated numerically using continuous wave (cw) parabolic equation simulations using a single mode starting field. The spreading of energy in mode number (and thus also in $I$, making use of Eq. (100)) was found to be well approximated by a gaussian whose variance grew like a constant - our estimate of $B$ - times range. These simulations gave the estimates $B = 6.7 \times 10^{-8}$ s$^2$/km for $m = 17$, $B = 1.3 \times 10^{-7}$

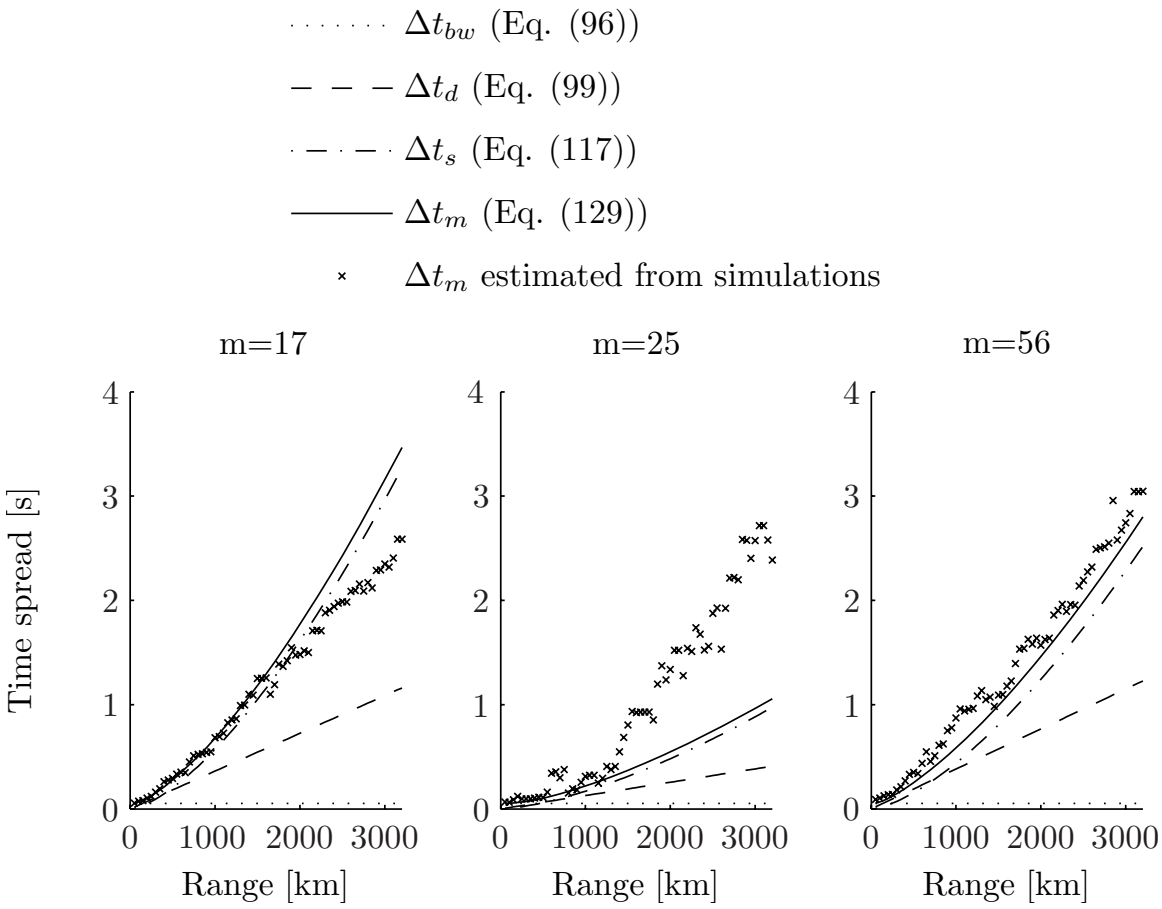


Figure 19. Predicted and simulated estimates of modal group time spreads $\Delta t_m$ vs range for three values of $m$. The simulated estimates of $\Delta t_m$ were extracted from wavefield simulations of the type shown in Fig. 18.

$s^2$/km for $m = 25$ and $B = 2.7 \times 10^{-7}$ $s^2$/km for $m = 56$. These values are in approximate agreement with the estimates of $B$ reported in [42] and [48].

The agreement between simulations and theory-based estimates of $\Delta t_m$ in Fig. 19 is seen to be good for $m = 17$ and $m = 56$. Agreement is not good for $m = 25$, however, where the predicted estimate of $\Delta t_s$ – and hence also $\Delta t_m$ – is too small. The reason for this discrepancy is that, as discussed above, for $m$-values near $m = 25$, $\beta(I)$ is not a slowly-varying function. This is clear from the $\beta(m, f_0 = 75 \text{ Hz})$ structure shown in Fig. 17. In order to account for this nonuniform $\beta$-weighting, Eq. (117)

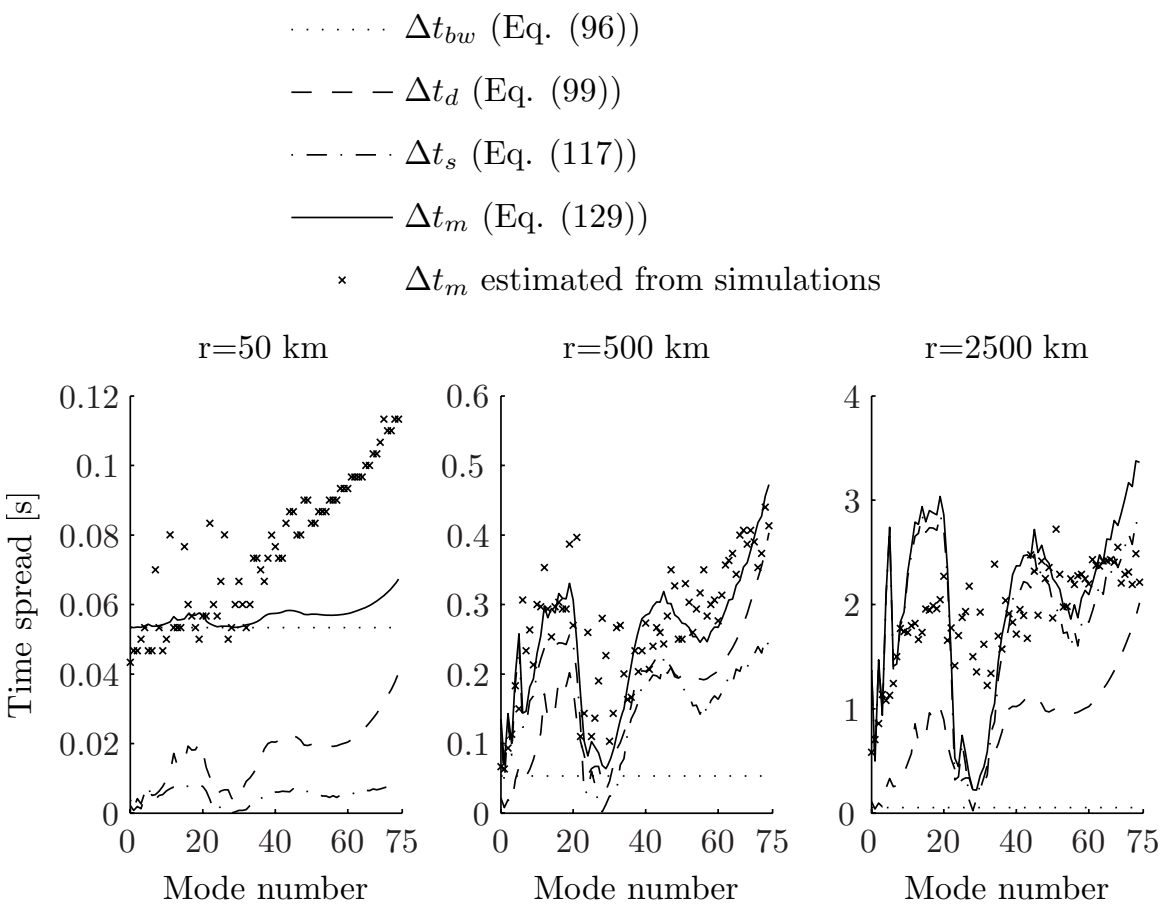


Figure 20. Predicted and simulated estimates of modal group time spreads $\Delta t_m$ vs mode number at $r = 50$ km, $r = 500$ km and $r = 2500$ km. The simulated estimates were extracted from the mode-processed wavefields shown in Fig. 18. Note that the time axes are different in the three subplots.

must be replaced by an estimate based on (128) rather than (114), as discussed above. Nonuniform $\beta$-weighting of scattered energy also explains why agreement between theory and simulations in Fig. 19 is better at short range than at long range for $m = 17$ and $m = 25$. For $m = 17$ scattered energy at long range has $|\beta| < |\beta\,(m = 17)|$ (see Fig. 17), so Eq. (117) predicts a value of $\Delta t_s$ that is too large. Similarly, for $m = 25$ scattered energy at long range has $|\beta| > |\beta\,(m = 25)|$ (see Fig. 17), so Eq. (117) predicts a value of $\Delta t_s$ that is too small.

Figure 20 shows a comparison of predicted and simulation-based estimates of

$\Delta t_m$ as a function of mode number at three ranges: 50 km, 500 km and 2500 km. The corresponding wavefields are shown in Fig. 18. The theoretical prediction of $\Delta t_m$ is based on Eqs. (96), (99), (117) and (129). The value of $B$ used in Eq. (117) was an empirical $m$-dependent fit to simulations of the type mentioned above: $B\,(m) = 0.44 \times (0.5 + m/10) \times 10^{-7}$ s$^2$/km. Agreement between the simple theoretical estimates and simulations is generally good. Note, however, that our estimate of $\Delta t_s$, based on Eq. (117), is clearly too low for $20 \leq m \leq 30$, especially at $r = 500$ km and $r = 2500$ km. This behavior is consistent with our explanation of the error associated with $\Delta t_s$ for $m = 25$ in Fig. 19. Also, note that at $r = 50$ km theoretical estimates of $\Delta t_m$ are clearly too small for $m \gtrsim 40$. The cause of this discrepancy is that Eqs. (95), (96) and (99) underpredict the nonscattered energy; this is linked to the bimodal (and highly nongaussian) distribution of energy in $(m, t)$ (see Fig. 18 at $r = 50$ km).

## 4.8 Simulations of modal group time spreads for an off-axial acoustic source

In this section we also present numerical simulations in an environment similar to the LOAPEX environment. There are three main differences from the simulations performed in the previous section: 1) The carrier frequency of the acoustic source was $f_0 = 68.2$ Hz and the computational bandwidth was $\Delta f_c = 34.1$ Hz, corresponding to an effective bandwidth of $\Delta f = 17.05$ Hz; 2) The depth of the source was 350 m which is far from the sound channel axis; and 3) Because the range-dependent environmental data was not available for all transmission ranges up to T3200 station, the range-independent background sound speed profile was chosen for numerical simulations,

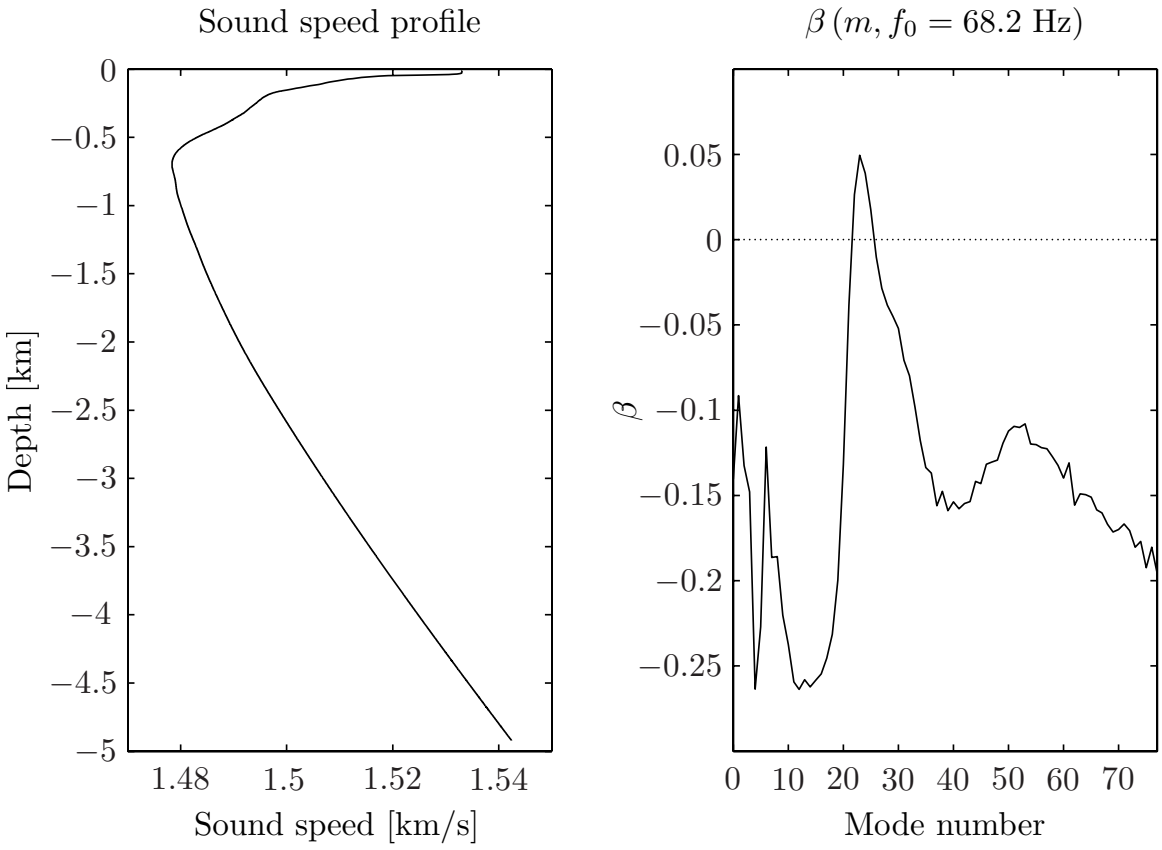


Figure 21. (left panel) Background sound speed profile used in the wavefield simulations shown in Figs. 22-24. (right panel) Corresponding plot of $\beta\,(m; \sigma_0)$ with $\sigma_0/2\pi = f_0 = 68.2$ Hz.

which is the profile computed from the environmental data at the SVLA location.

Figure 21 shows the background sound speed profile $c\,(z)$, which is the same as shown on the left panel of Fig. 17, and corresponding plot of $\beta\,(m, f_0)$. As was discussed above, the choice of center frequency in the asymptotic quantization condition (100) leads only to a rescaling of the mode number axis. Note that the structure of $\beta\,(m, f_0)$ differs slightly for $f_0 = 75$ Hz and $f_0 = 68.2$ Hz, because in both cases $\beta\,(m, f_0)$ was computed from cw normal mode simulations. The same internal-wave-induced sound speed perturbation $\delta c\,(z, r)$ was superimposed on the

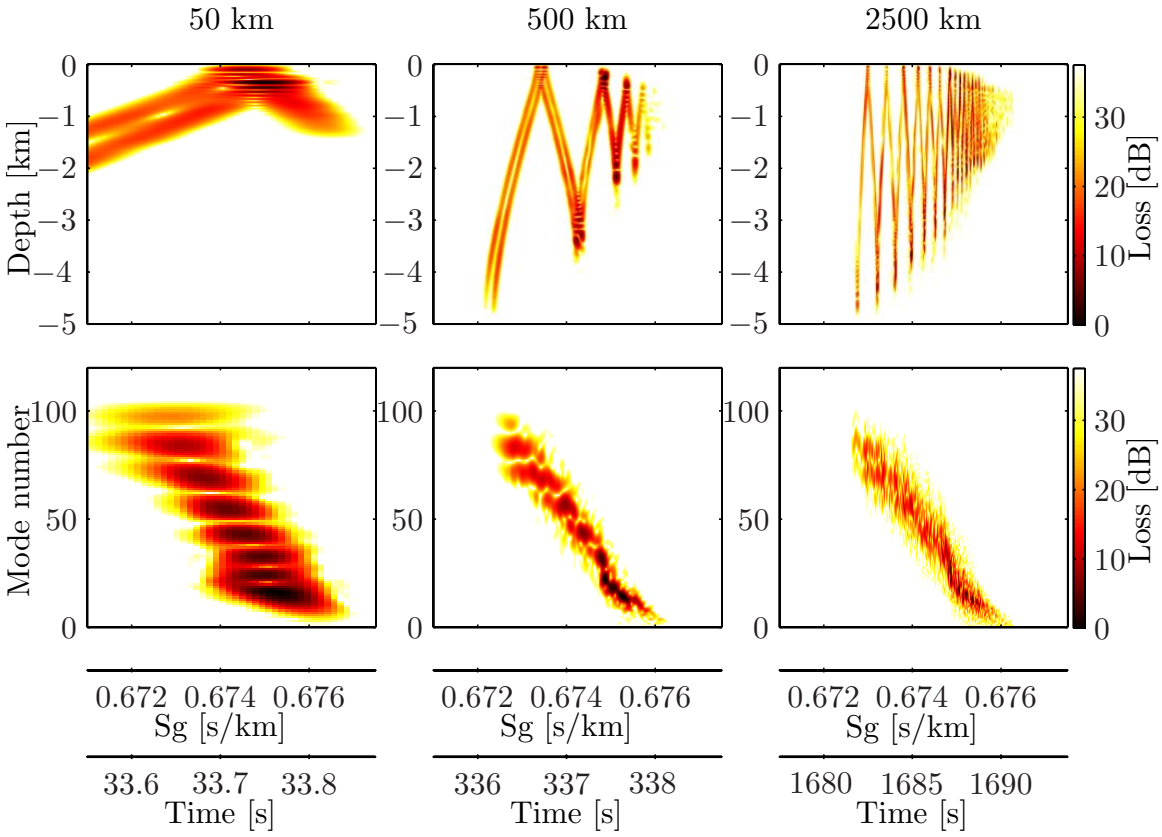


Figure 22. Simulated wavefields with $f_0 = 68.2$ Hz, $\Delta f_c = 34.1$ Hz at three ranges in the environment shown in Fig. 21, with an internal-wave-induced sound speed perturbation superimposed. (upper panels) Wavefield intensity in $(z, t)$. (lower panels) Corresponding mode-processed fields in $(m, t)$ where $t = S_g r$.

background $c(z)$ in these simulations.

Figure 22 shows sample wavefields in $(z, t)$ at three ranges, together with the corresponding mode-processed fields in $(m, t)$. The main difference from Fig. 18 is that the shallow acoustic source located far from the sound channel axis does not initially excite modes with small mode numbers (modes with both turning depths below the location of the source). This feature is clearly seen at all three transmission ranges and is expressed as the absence of the strong late near-axial arrival. However, because of mode coupling along the propagation path some energy is being scattered from large mode numbers into low mode numbers. Estimation of the modal group

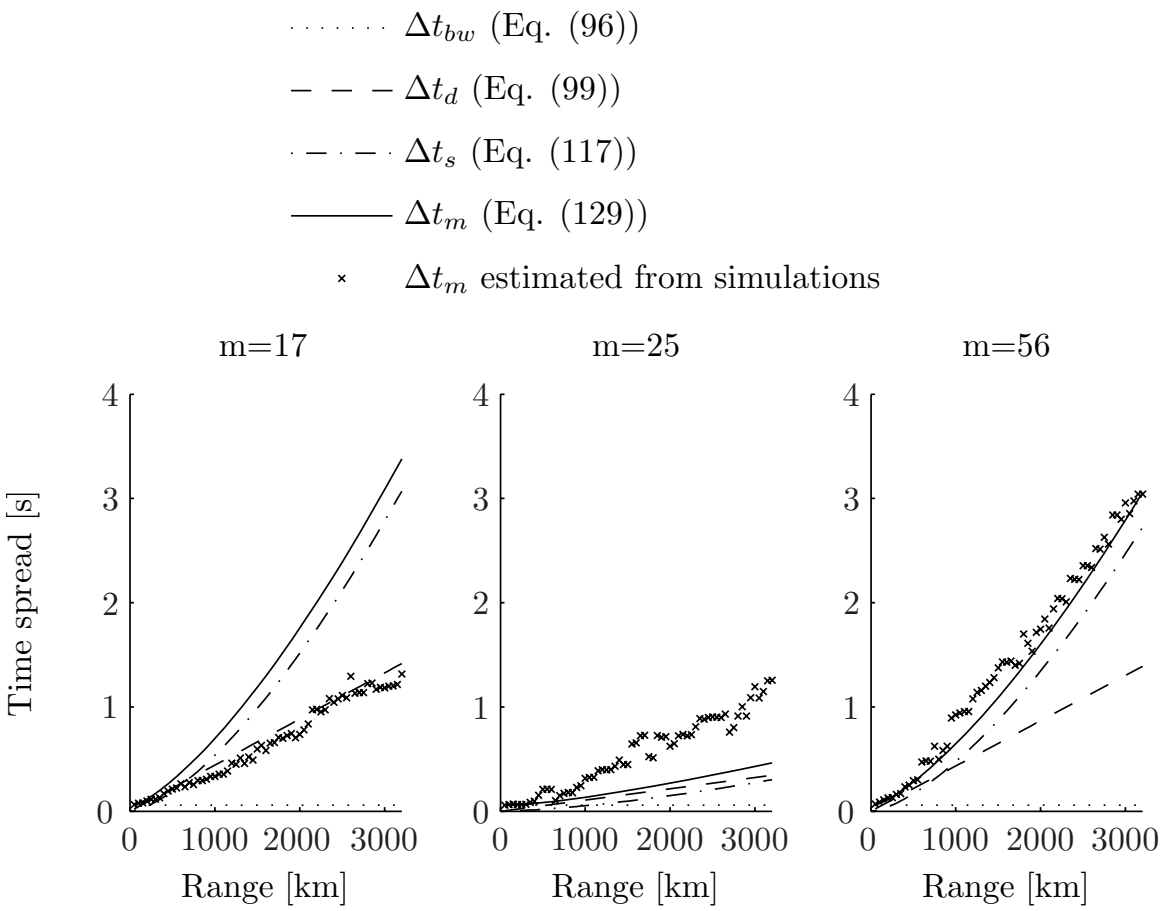


Figure 23. Predicted and simulated estimates of modal group time spreads $\Delta t_m$ vs range for three values of $m$. The simulated estimates of $\Delta t_m$ were extracted from wavefield simulations of the type shown in Fig. 22.

time spreads for near-axial arrivals in this situation is difficult and sometimes impossible, because in practice the intensity of the signal contained in low mode numbers may be significantly below the noise level. This issue will be discussed in more detail in Sec. 5.4. Also it is expected that corrections to the main arrival time and modal group time spreads discussed at the end of Sec. 4.5 are important.

By performing the mode processing on wavefields at many ranges, $\Delta t_m(r)$ for all mode numbers can be estimated. As in the Sec. 4.7, three such plots for $m$ =17, 25 and 56 are shown in Fig. 23. The main difference from Fig. 19 is that the agreement

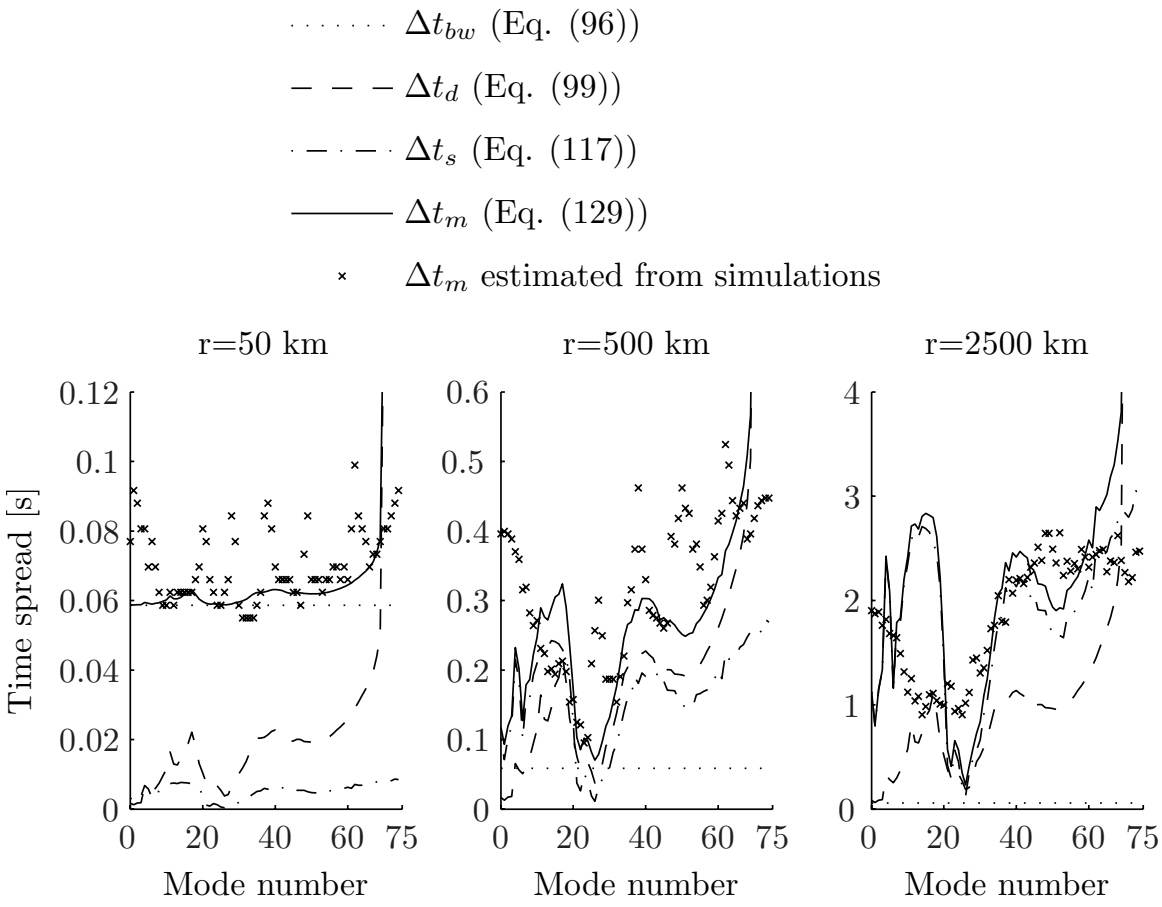


Figure 24. Predicted and simulated estimates of modal group time spreads $\Delta t_m$ vs mode number at $r = 50$ km, $r = 500$ km and $r = 2500$ km. The simulated estimates were extracted from the mode-processed wavefields shown in Fig. 22. Note that the time axes are different in the three subplots.

for $m = 17$ between theoretical predictions and numerical simulations is not good. The most likely explanation for the disagreement is that $|\beta\,(m = 17, \sigma_0)|$ has sharp local maximum, therefore the effective value of $|\beta|$ is should be significantly smaller. Also, as in Fig. 19, the agreement is not good for $m = 25$. The predicted estimate of $\Delta t_s$ is too small. The reason for this discrepancy is that $\beta\,(I)$ is not a slowly-varying function.

Figure 24 shows a comparison of predicted and simulation-based estimates of $\Delta t_m$ as a function of mode number at three ranges: 50, 500, and 2500 km. The theoretical

prediction of $\Delta t_m$ is based on Eqs. (96), (99), (117) and (129). Agreement between theoretical estimates and simulations is generally good. The estimates of modal group time spreads for small mode numbers are too large at short ranges. This behavior is consistent with our explanation of the difficulty of estimating modal group time spreads for modes that are not originally excited by the source.

# 5 Analysis of the LOAPEX experimental data set

In this chapter the analysis of the experimental data collected during the 2004 NPAL experiment is presented. An attempt to reconcile the experimental data analysis results with theoretical results from previous sections is made. Different challenges associated with analysis of the collected data are discussed.

## 5.1 Experimental setup and collected data

The 2004 NPAL (North Pacific Acoustic Laboratory) long-range ocean acoustic propagation experiment consists of three closely related components, or sub-experiments, named SPICE04, LOAPEX (Long-range Ocean Acoustic Propagation EXperiment), and BASSEX (Basin Acoustic Seamount Scattering EXperiment). In this work only one part of the experiment, the LOAPEX part, will be considered. During the LOAPEX phase of experiment the acoustical data was continuously recorded with long array of hydrophones deployed in the eastern North Pacific ocean. The experimental geometry is shown in Fig. 25. The location of a vertical line array (VLA) of hydrophones that was used to record transmitted acoustic signals is shown with a yellow dot in Fig. 25. The VLA consists of two moorings: shallow VLA (SVLA) and deep VLA (DVLA) which were deployed approximately 5 km apart from each other. This common set of hydrophones was used to record SPICE04 and LOAPEX transmissions. The SVLA is 1400 m long, has 40 hydrophones on it (two segments, upper SVLA and lower SVLA with 20 hydrophones on each segment) with 35 m spacing between hydrophones and was deployed to cover the ocean depths from 350

m to 1750 m nominally. The placement of the SVLA was chosen in such a way that it was centered approximately on the sound channel axis and designed to optimize the resolution of acoustic modes 1–10 at 75 Hz transmission frequency. The DVLA is 2100 m long, has 60 hydrophones on it (three segments, upper DVLA, middle DVLA and lower DVLA with 20 hydrophones on each segment) with 35 m spacing between hydrophones and was deployed to cover the ocean depths from 2150 m to 4270 m nominal. The main purpose of such a placement was to sample the acoustic field near the lower steep ray turning depths.

Signal transmissions were made using a ship suspended acoustic source. Eight transmission stations are shown as red dots in Fig. 25 and seven of them are on the main LOAPEX propagation path indicated by the black solid line, which was chosen to be a geodesic line with little variations in the ocean depth. The ocean depth was approximately 5 km along the propagation path. These seven stations were nominally 50, 250, 500, 1000, 1600, 2300, and 3200 km away from the VLAs. These distances provided the range dependence sought in this experiment. At each of the seven stations, the LOAPEX acoustic source was suspended from the ship for several hours. Two source depths were typically used at each of the seven stations: 350 m and 500 m or 800 m.

Signals of different types were transmitted; in this work we will focus only on the analysis of the m-sequence receptions [49]. Two center frequencies were chosen: 75 Hz for 800 m source depth transmissions and 68.2 Hz for 350 m or 500 m source depth transmissions. In both cases the digit length of the m-sequence was 1023, two cycles of the carrier per digit were used, which lead to slightly different sequence lengths,

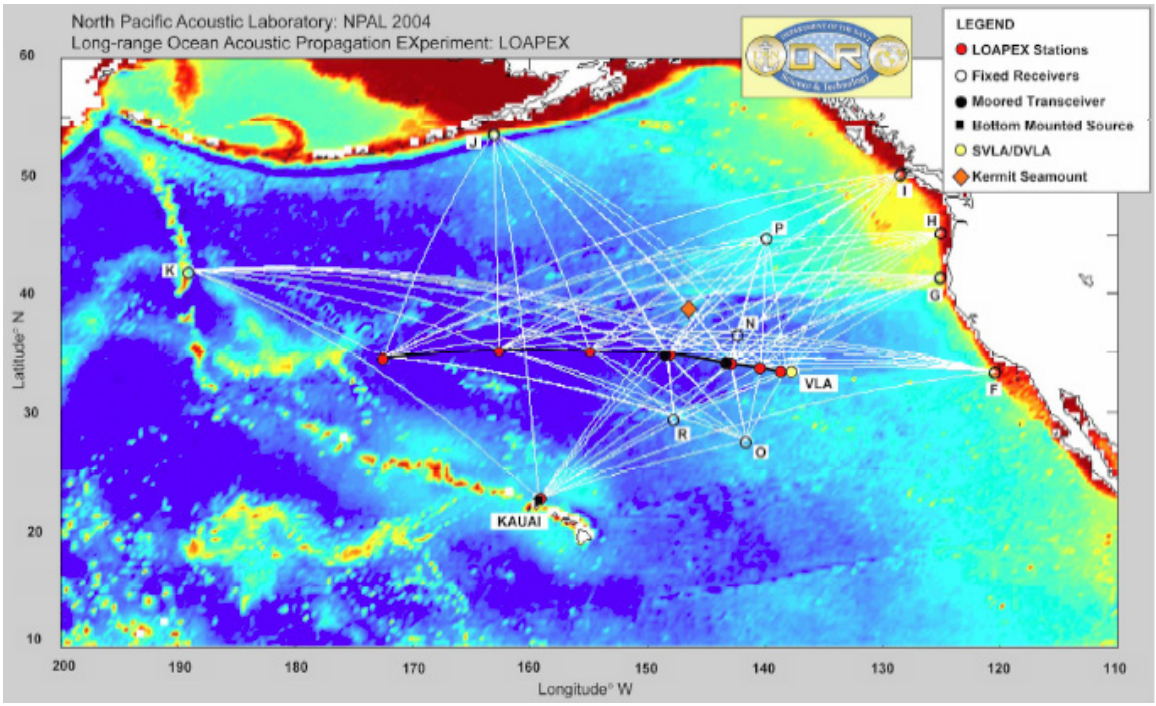


Figure 25. LOAPEX assets and geometry

27.28 sec in the first case and 30 sec in the second case. The detailed description of the signal type used can be found in [50].

LOAPEX transmissions were made in the period September 14, 2004 to October 10, 2004 covering transmission ranges from 50 km to 3200 km. The recovery cruise on the research vessel "Thomas G. Thompson" took place from June 6, 2005 to June 26, 2005. The acoustical data was available shortly after the recovery cruise.

## 5.2 Experimental data deficiencies

Even before the data became available it was clear that analysis of this data would present several challenges. First, the implementation of mode processing technique uses orthogonality of normal modes and in practice requires a dense sampling of acoustic receptions at the receiver location throughout the whole water column. A very

dense sampling means that ideally the distance between neighboring hydrophones should be much less than the distance between adjacent zeros of the highest propagating mode. If this condition is satisfied, the energy contained in each propagating mode will not be aliased to other modes. In the scope of the experimental setup described in the previous section and in the LOAPEX-like environment the number of propagating modes can be roughly estimated to be around 100. This estimation suggests that the spacing between hydrophones should be much less than 50 m in order to capture energy correctly in all propagating modes. This sampling condition is satisfied for low mode numbers, but not for modes with mode numbers greater than about 20. It will be shown in Sec. 5.3 that, surprisingly, this limitation does not lead to significant errors in the mode processing results.

A more serious shortcoming of the collected data is the presence of large gaps in the receiving array. Unfortunately, acoustical data from the middle segment of the DVLA was not recovered. Also data on some hydrophones is corrupted at some transmissions. Thus, there are four large gaps in the receiving array: from the ocean surface to the upper segment of the SVLA (0-350 m depth), between SVLA and DVLA (1750-2150m), between upper DVLA and lower DVLA (2850-3550 m) and near the bottom (4270 m to the bottom). These gaps lead to modal cross-talk and introduce errors in the mode processing results. It is also argued in Sec. 5.3 that largest errors are introduced when high intensity arrivals which usually correspond to turning points on the arrival time front are not captured by the receiving array. For these reasons, probably, the most significant error that is introduced in the mode processing analysis from the VLA geometry is the absence of hydrophones in the

upper ocean (from 0 m to 350 m in depth).

Another type of receiver array deficiency is the horizontal separation of SVLA and DVLA. These two segments were deployed approximately 5 km apart from each other. Therefore the transmission ranges corresponding to SVLA and DVLA receptions are slightly different. In order to implement the direct projection mode filtering technique it is required that the received signal is recorded at a single range. In the analysis presented in Sec. 5.4 it is assumed that the data was recorded at the same range, corresponding to SVLA range, at both SVLA and DVLA. The data recorded by DVLA is shifted in time to complement the time front structure recorded by SVLA. Of course, this shift leads to introduction of phase errors in the received signal. However, it is demonstrated in Sec. 5.3 that only small errors are introduced by this small time shift.

It is important to note that not only receiving array deficiencies influence the effectiveness of mode processing. An adequate knowledge of environment is crucial for correct interpretation of mode processing results. Although only the sound speed structure at the receiver location is required to perform the mode processing, it is desirable to have range-dependent sound speed structure in order to perform numerical simulations. In the LOAPEX environment the range dependence is weak, but has to be accounted for, especially at long transmission ranges. There are several other factors that also contribute to the error in the mode processing. These include mooring and source motion, both vertical and horizontal, lack of knowledge of exact propagation ranges and presence of ambient noise. The contribution from ambient noise can be reduced by coherently averaging several sequential transmissions. This

technique improves signal to noise ratio, but because of environmental variability the averaging time can not be too large. Additional difficulty arises from the fact that the data was not recorded continuously, but has gaps approximately every 5 minutes. Therefore for the data analysis that follows the averaging time was chosen to be 5 minutes.

Another important issue that needs to be addressed is an estimation of errors of modal group time spreads computed from the LOAPEX data. The simplest approach to this problem is to analyze several independent transmissions with the same transmission parameters and then compute means and variances of modal group time spreads. This task will be done, but has not yet been done. The LOAPEX data set is very extensive and much of it has not been analyzed yet.

## 5.3 Numerical simulations of receptions recorded by deficient receiving array

Before we present analysis of the LOAPEX data transmissions it is useful to investigate how the presence of deficiencies in receiving array affects mode processing results. One transmission range was chosen for numerical simulations that corresponds approximately to a nominally 1000 km-long (hereafter T1000) transmission. In this case the distance from the source to the SVLA receiver was 983 km and to the DVLA was 988 km. The environmental data is available for this range so the range-dependent sound speed profile was constructed using the actual CTD measurements. It is important to note that the sound speed data used for simulations includes

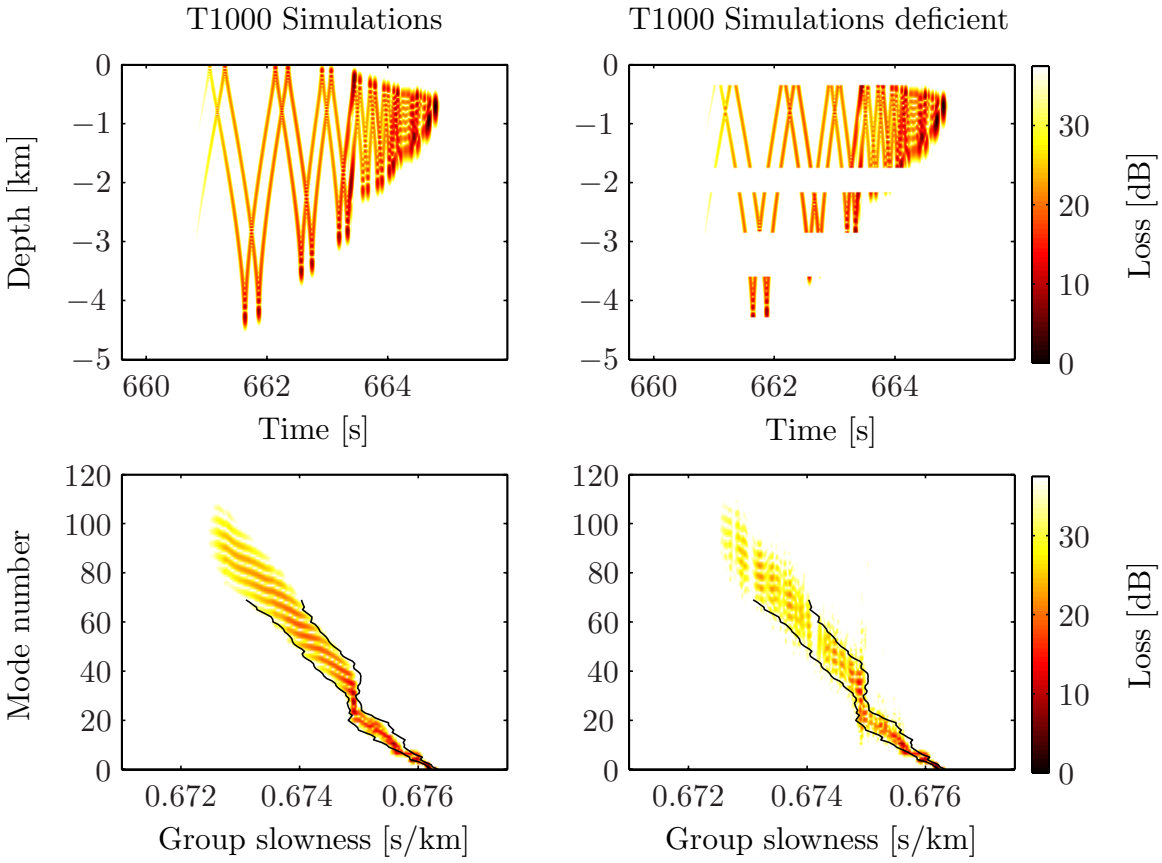


Figure 26. PE simulations for T1000 transmission range performed in the LOAPEX-like environment. Transient wavefields with dense receiving array (upper left panel) and sparse receiving array with gaps (upper right panel) and corresponding modal group time spread diagrams (lower panels) are shown. Black solid lines are theoretical estimates of modal group time spreads.

mesoscale variability but does not resolve any small scale features present, for example, due to internal waves. The simulations shown in this section were performed in the slowly-varying background sound speed profile without internal wave induced structure superimposed.

Figure 26 shows the comparison between PE simulations performed with the use of a dense receiving array (on the left) and a sparse receiving array with gaps (on the right). Time front on the upper left subplot and corresponding modal group time spread diagram (lower left subplot) were constructed with the assumptions that

receivers were spaced equidistantly in depth with approximately 13.7 m spacing and covered the entire water column. The two subplots on the right are time front and modal group time spread diagram constructed with the use of a deficient receiving array. In order to simulate the deficiency of LOAPEX array depth interpolation of the received signal would be necessary, which is not desirable because it leads to additional errors. Therefore, the spacing between hydrophones was chosen to be approximately 27.3 m and gaps were placed approximately at the same locations as were in the LOAPEX array. Though the deficiency of the receiving array was not as severe as the LOAPEX array, this simulation allows one to see how the presence of such deficiencies influence modal group time spread diagram. It is seen in the Fig. 26 that mode processing works reasonably well with the deficient array allowing one to estimate modal group time spreads with only small errors for almost all propagating modes. Despite significant modal cross-talk in the frequency domain, time domain mode processing is seen to work very well. Part of the explanation for this behavior is that the inverse Fourier transform tends to retain correct coherent contributions while cancelling random phase errors in the frequency domain mode filtered results. However, when high intensity arrivals are not being captured by the deficient array (this usually happens near turning points on the time front), this energy does not appear on the modal group time spread diagram, which leads to formation of vertical gaps on this diagram. Also sparse spacing of hydrophones leads to aliasing of energy from one mode number to another. The black solid curve on both modal group time spread diagrams is the same and is the asymptotic theoretical estimate obtained using

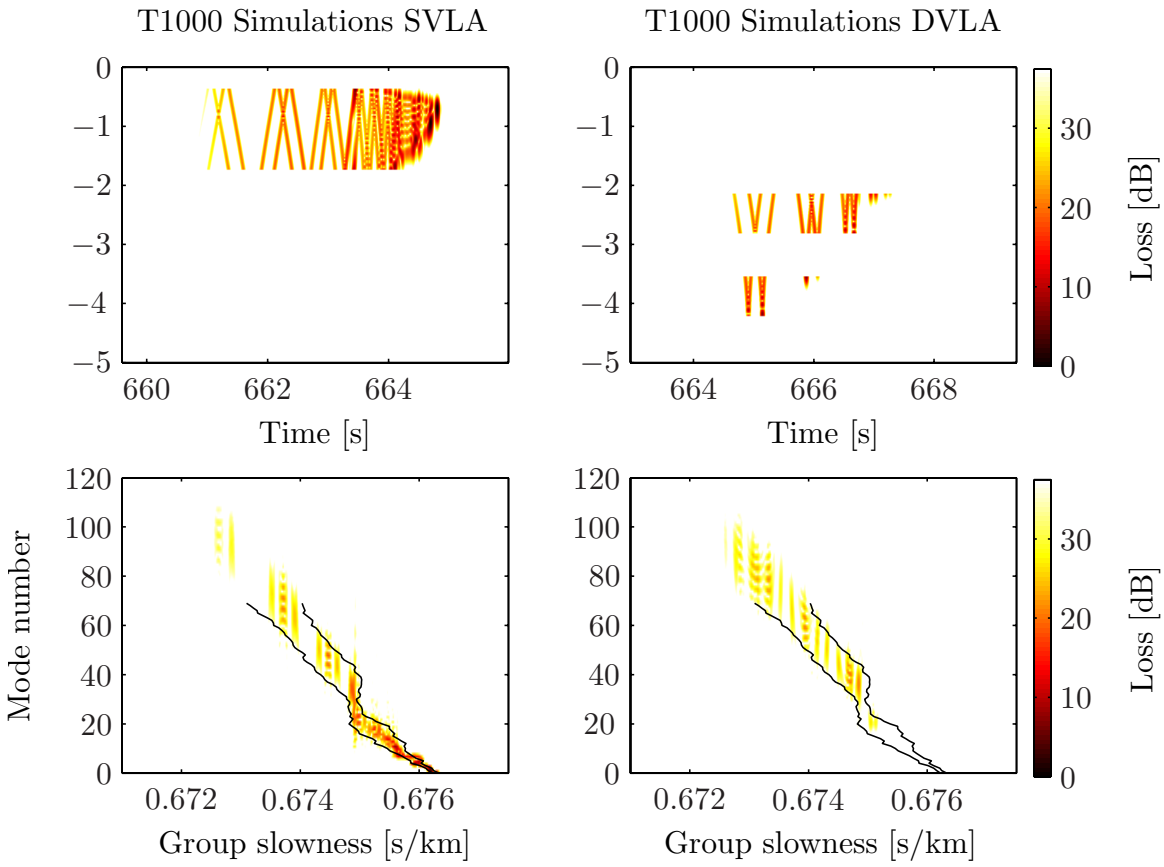


Figure 27. Simulated time-domain transient wavefields (upper panels) and corresponding modal group time spread diagrams (lower panels) for SVLA only receiving array (left panels) and DVLA only receiving array (right panels).

Eqs. (96), (99), (117) and (129).

Because the acoustical receptions were recorded on two separate moorings, SVLA and DVLA, which were approximately 5 km from each other, it is useful to understand how the mode processing results would change if only one VLA were present. The two left panels in Fig. 27 show the time front and corresponding modal group time spread diagram recorded on the SVLA only. This simulation shows that SVLA receiver allows estimation of modal group time spreads for modes up to approximately 20. The two subplots on the right in Fig. 27 are simulations with DVLA receiver only. Note the difference in time scale between left and right subplot which corresponds to horizontal

distance of 5 km between VLA segments. From the modal group time spread diagram for DVLA simulation we conclude that DVLA receiver does not resolve any energy for modes up to approximately 20, however, it provides additional information about modal group times spreads for modes with higher mode numbers. It is possible to perform the dynamical extrapolation of the DVLA reception in range by 5 km. In order to do this it is necessary to compute the modal amplitude coefficients (Eq. (92)), then multiply them by the appropriate expansion factor and then compute new intensity field using Eq. (91). If the distance between the DVLA and the SVLA is small compared to the propagation range, the amplitude of the signal will remain almost unchanged; only the phase will change. Therefore, the intensity diagram of modal group time spreads can be computed with the DVLA signal that contains small phase errors. The validity of this assertion is demonstrated with the simulation shown if Fig. 28. In this figure the two left panels are simulations performed with the distance to the receiver of 983 km. The two right panels are constructed in such a way that the signal on the SVLA is recorded at 983 km, and signal on the DVLA is recorded at 988 km, but then DVLA signal is shifted in time by a constant in order to approximately match the SVLA reception. Because of phase errors the time front branches do not line up perfectly, but modal group time spread diagrams are almost identical in both simulations. This technique will be used everywhere in the following

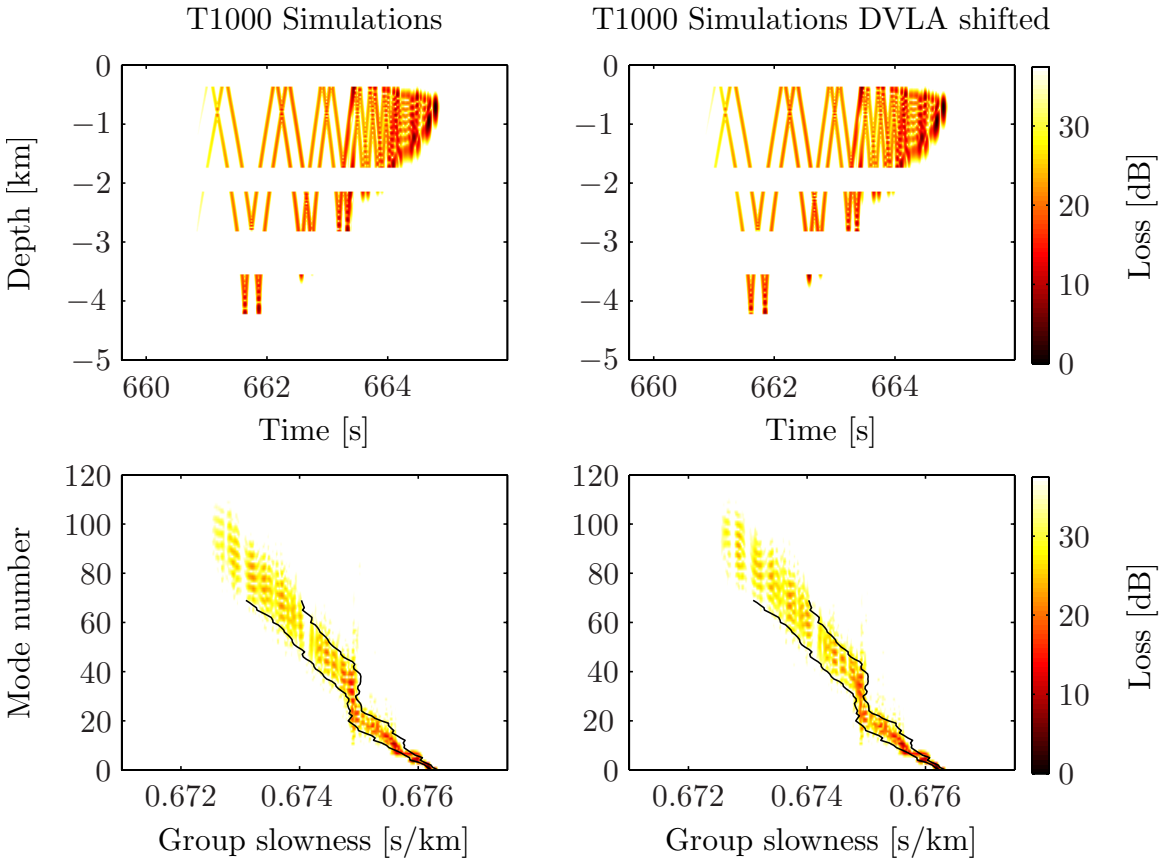


Figure 28. Simulated time-domain transient wavefields for T1000 transmission (upper panels) and corresponding modal group time spread diagrams (lower panels). Two left panels are produced under suumption that transmission range to SVLA and DVLA is the same. Two right panels are produced with the DVLA wavefield shifted in range in order to approximately match SVLA receptions.

section where we present the analysis of the LOAPEX data.

## 5.4 Modal group time spreads in the LOAPEX experiment

This section is devoted to the analysis of the LOAPEX data set and comparison with numerical simulations. This data set is very extensive and much of it has not been processed yet. In this work we present several examples of transmissions performed with the acoustic source deployed at 800 m with 75 Hz carrier frequency and transmission ranges up to 1000 km and with the source deployed at 350 m with 68.2 Hz

carrier frequency and transmission ranges up to 3200 km. There is a very important difference between these two types of transmissions. The deep source location (800 m) corresponds approximately to the depth of the sound channel axis. Therefore, such a source excites most acoustic modes in the given environment. The energy in each mode is scattered into neighboring modes along the propagation path, so in general some energy is present in all modes at the receiver location. The shallow source location (350 m) is essentially off-axial. Such a source does not excite modes with upper turning depths below 350 m. However, energy is scattered into modes with low mode numbers whose excitation grows with increasing range.

Numerical simulations were performed by solving the standard parabolic equation in the transformed environment as discussed in Sec. 4.4. A realistic internal-wave-induced sound speed perturbation $\delta c\,(z, r)$ was superimposed on the background sound speed profile in the simulations using the technique described in [47].

Figure 29 compares numerical simulations (left panels) with LOAPEX data (right panels) for 75 Hz carrier frequency source deployed at 800 m and at a transmission range corresponding to the T50 LOAPEX station. The black solid line on both modal group time spread diagrams is the theoretical estimate of modal group time spreads according to Eqs. (96), (99), (117) and (129). The agreement between theoretical predictions, numerical simulations and data processing results is seen to be good. Modal group time spreads are correctly estimated for almost all propagating modes. Among the three contributions the reciprocal bandwidth contribution is clearly the dominant. There are two features that need to be discussed, which are only present at T50 transmission range. First is the presence of bottom reflected arrivals on the

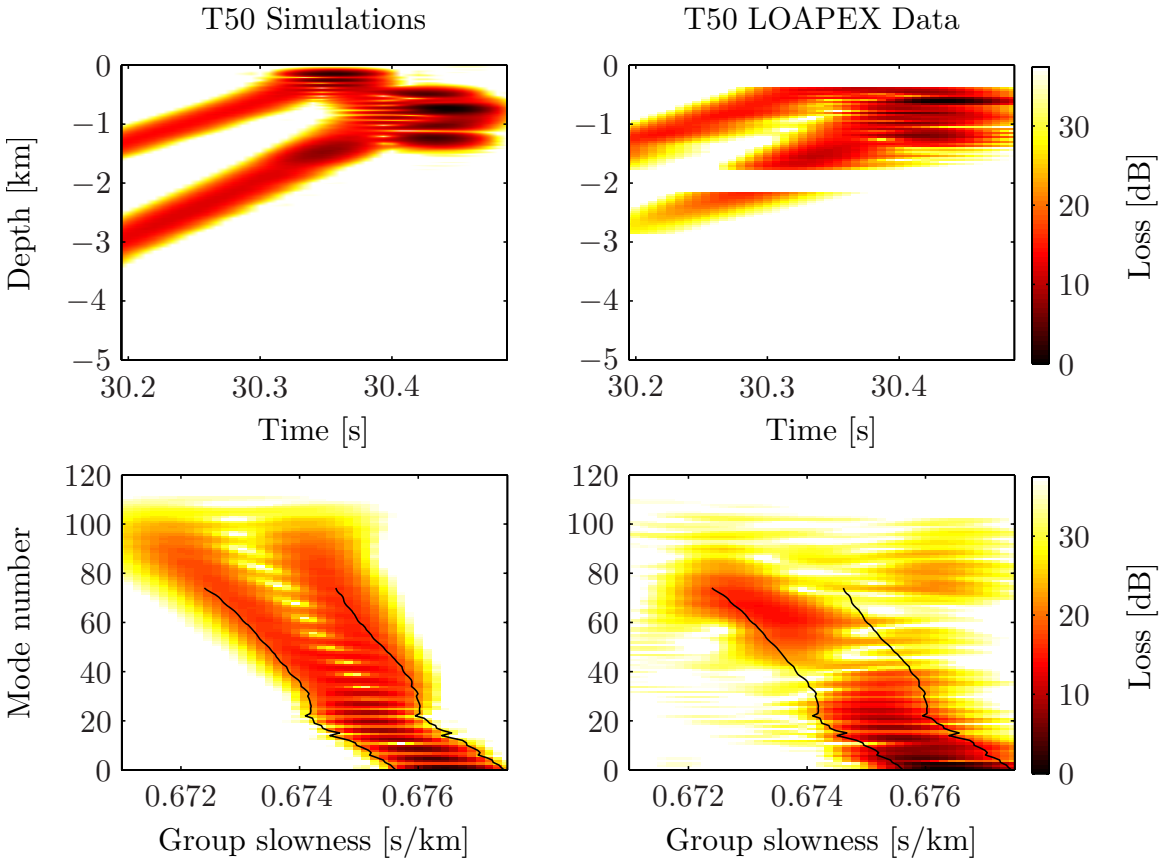


Figure 29. PE simulated time-domain transient wavefield for transmission T50 (upper left panel) for the axial source with $f_0 = 75$ Hz; LOAPEX time-domain data at T50 station (upper right panel); and corresponding modal group time spread diagrams (lower panels). Black lines are theoretical estimates of modal group time spreads.

LOAPEX data diagrams. The energy that has been reflected from the bottom is clearly visible on the data time front and was partially removed by a simple time-gating process prior to performing mode processing. Because this bottom reflected energy interferes with the main arrival there is no simple way to completely eliminate this energy and therefore it is clearly present on the modal group time spread diagram. Second, a bimodal distribution of energy in $(m, t)$-space is observed in the simulations, which leads to a slight disagreement between theoretical estimates of modal group time spreads and numerical simulations.

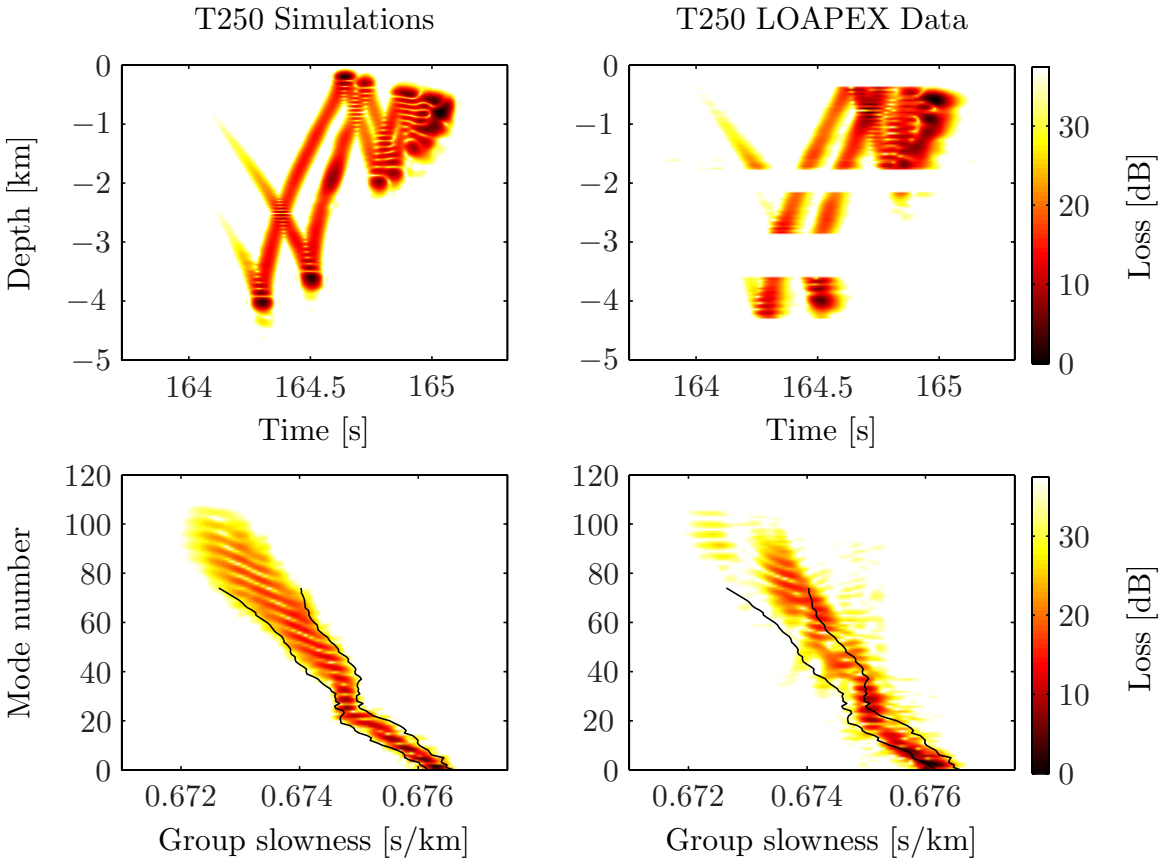


Figure 30. PE simulated time-domain transient wavefield for transmission T250 (upper left panel) for the axial source with $f_0 = 75$ Hz; LOAPEX time-domain data at T250 station (upper right panel); and corresponding modal group time spread diagrams (lower panels). Black lines are theoretical estimates of modal group time spreads.

Figure 30 shows similar simulations as shown in the previous figure but for T250 transmission range. In this figure the redistribution of energy in $(m, t)$-space is unimodal and the dominant contribution to the total modal group time spread is the deterministic dispersive contribution. Modal group time spreads are seen to be predicted correctly for almost all propagating modes. The mismatch between the modal group time spreads computed from data and theoretical prediction is probably primarily due to lack of knowledge of the environment along the propagation path at the time transmission took place. Note also, that mode processing was done with the

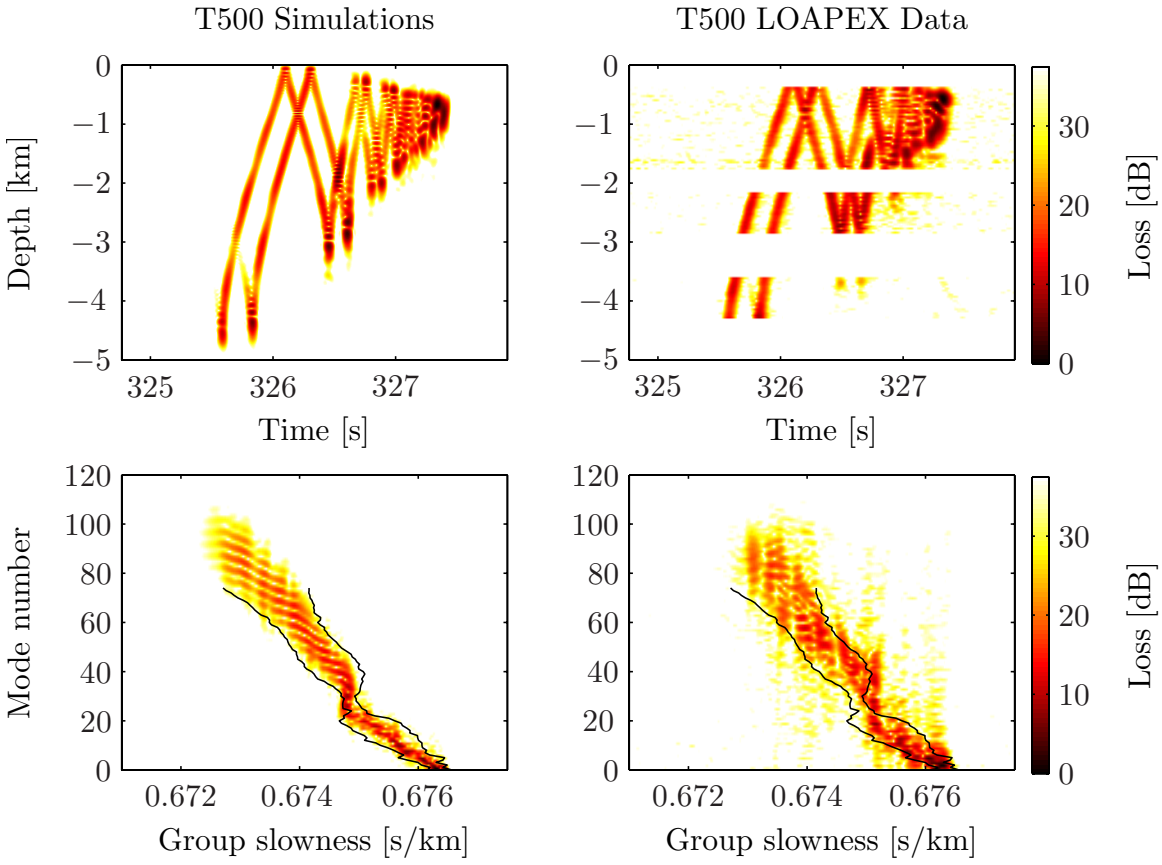


Figure 31. PE simulated time-domain transient wavefield for transmission T500 (upper left panel) for the axial source with $f_0 = 75$ Hz; LOAPEX time-domain data at T500 station (upper right panel); and corresponding modal group time spread diagrams (lower panels). Black lines are theoretical estimates of modal group time spreads.

use of the environment at the SVLA location which differs slightly from the range-averaged sound speed profile along the propagation path.

Figure 31 provides the comparison between simulations and data for T500 transmission range. Again, the overall agreement between theory, simulations and observations is reasonably good. Note, however, the presence of energy leakage in mode number in the data-based modal group time spread diagram. This happens because of modal cross-talk and, as discussed before, happens mostly at times when high intensity arrivals are not captured by the VLA.

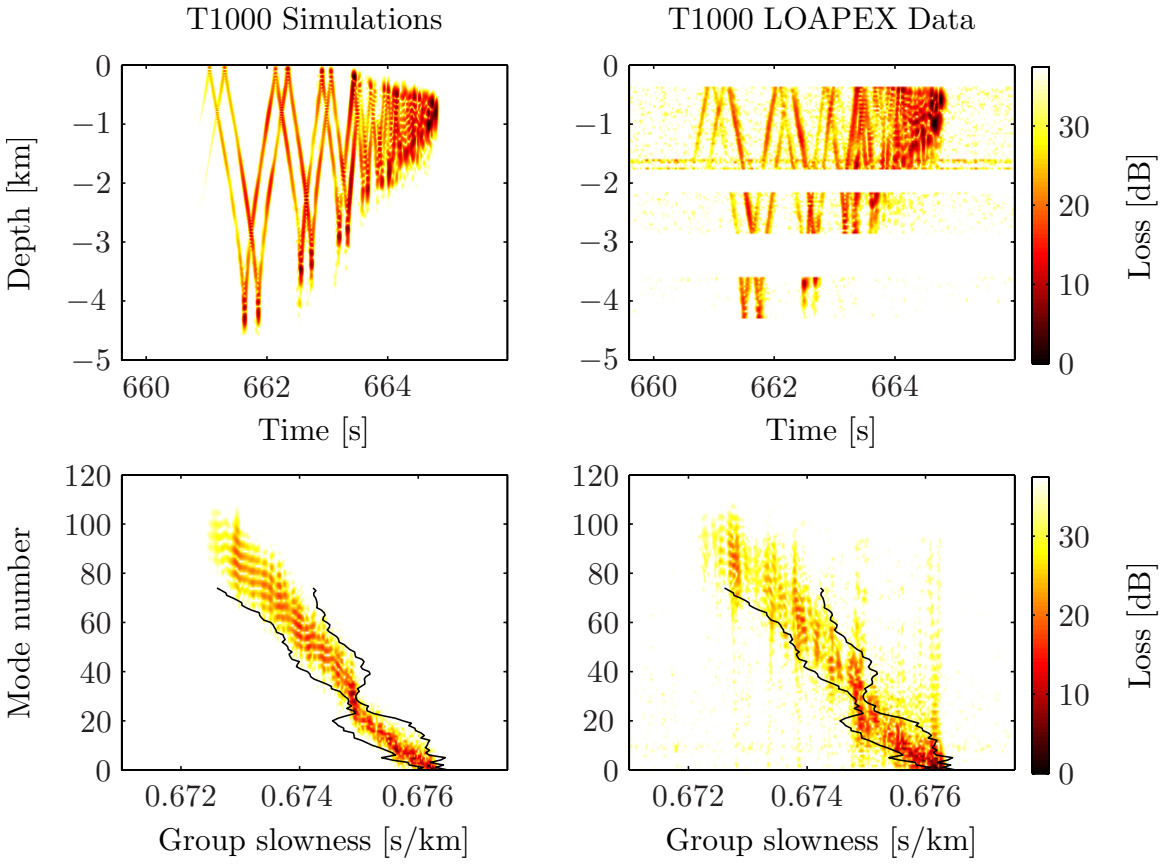


Figure 32. PE simulated time-domain transient wavefield for transmission T1000 (upper left panel) for the axial source with $f_0 = 75$ Hz; LOAPEX time-domain data at T1000 station (upper right panel); and corresponding modal group time spread diagrams (lower panels). Black lines are theoretical estimates of modal group time spreads.

Figure 32 shows numerical simulations and LOAPEX data at the T1000 transmission range. At approximately this range the scattering induced contribution to modal group time spreads becomes larger than the deterministic dispersive contribution for most mode numbers. Since $\Delta t_d \sim r$ and $\Delta t_s \sim r^{3/2}$, it is expected that $\Delta t_s$ is the dominant contribution at longer transmission ranges.

As in Sec. 4.7 we now consider estimates of $\Delta t_m(r)$ for $m$ =17, 25 and 56. Figure 33 is the same as Fig. 19 in Sec. 4.7, but with data-based estimates of $\Delta t_m(r)$ superimposed using red dots. The agreement between theoretical predictions,

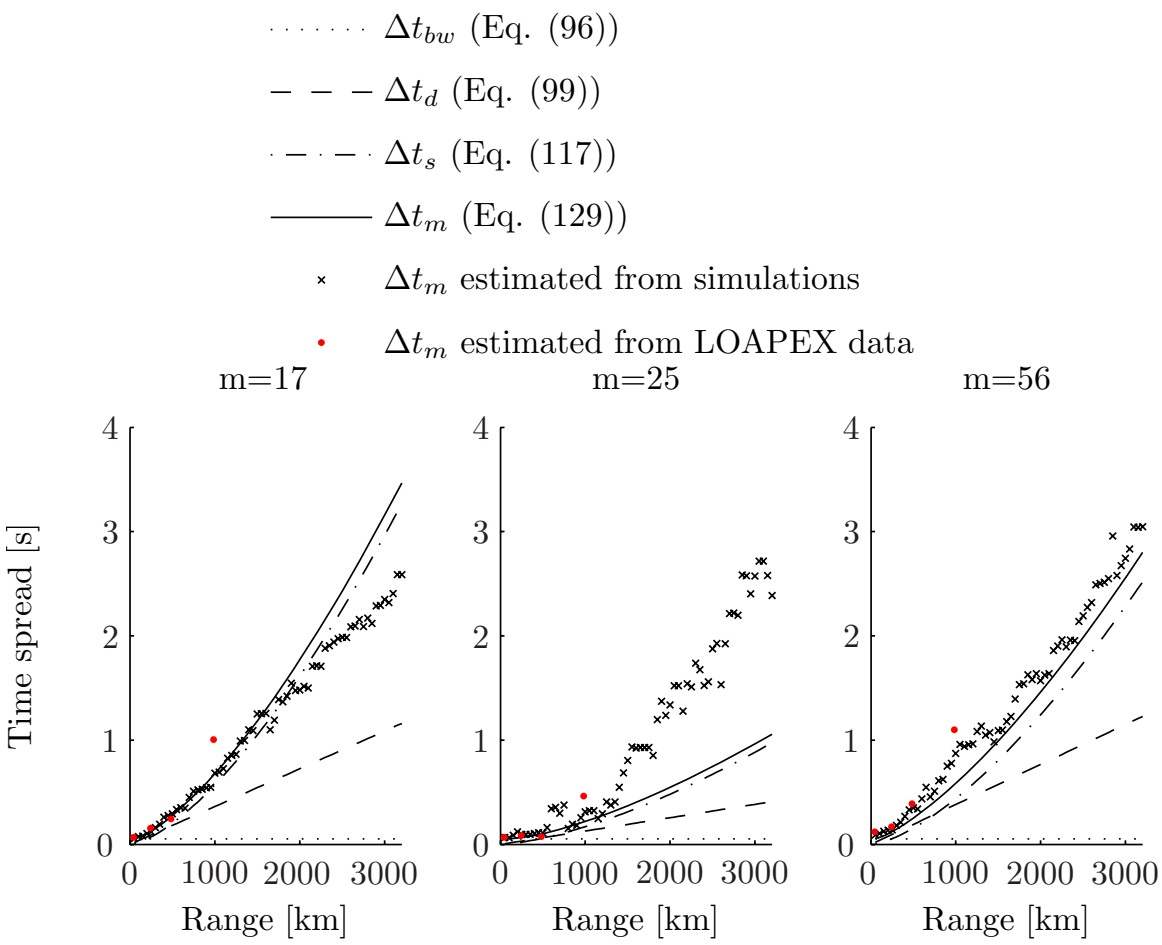


Figure 33. Predicted, simulated and measured estimates of modal group time spreads $\Delta t_m$ vs range for three values of $m$.

numerical simulations and data processing results is seen to be reasonably good. Also this figure supports the prediction that scattering induced contribution dominates for $r \gtrsim 1000$ km.

Figure 34 is also the same as in Sec. 4.7 (Fig. 20), but with data processing estimates superimposed at the two shorter ranges. The transmission ranges used for data processing were 45 km and 484 km instead of 50 km and 500 km respectively. This discrepancy leads to small errors in estimation of $\Delta t_m(r)$ relative to the data. A more significant source of errors in estimating $\Delta t_m(r)$ from the data comes from

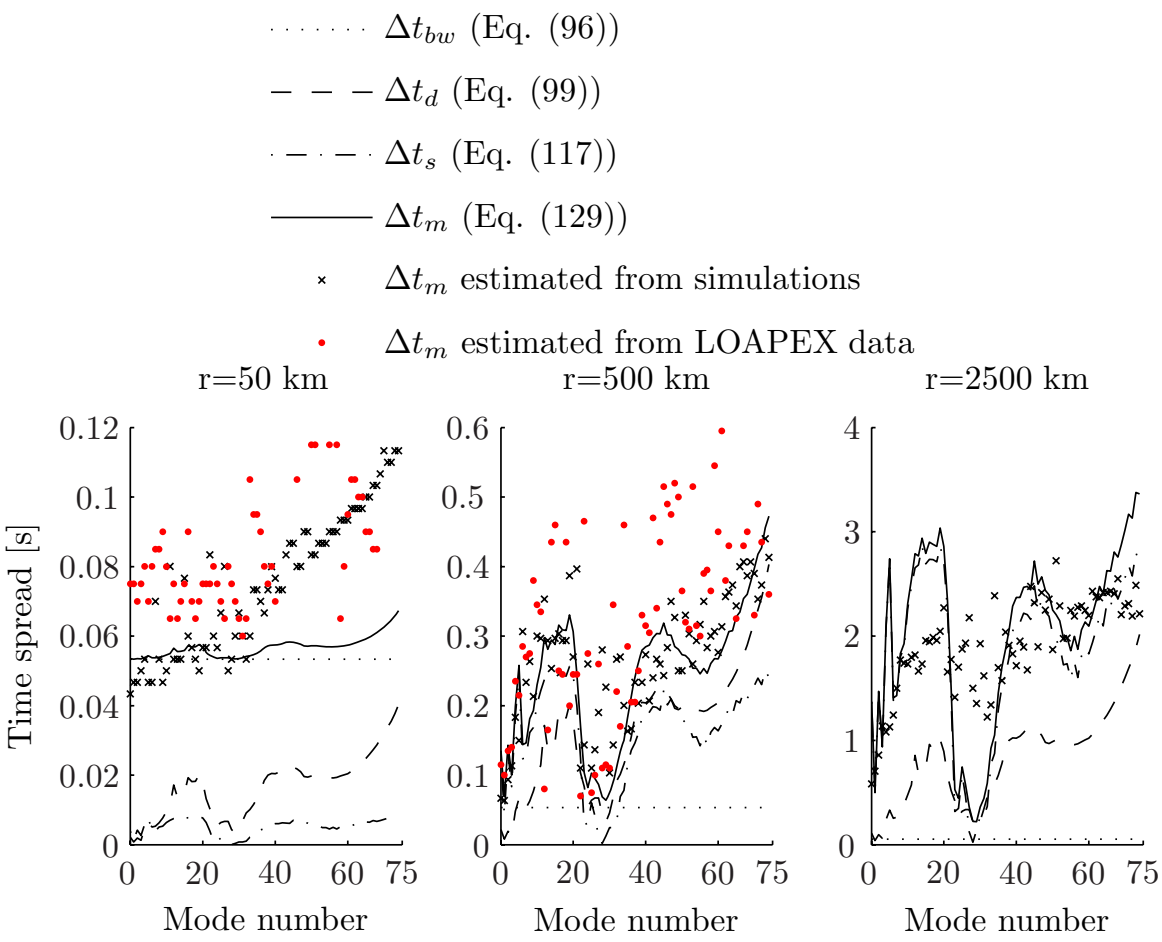


Figure 34. Predicted simulated and measured estimates of modal group time spreads $\Delta t_m$ vs mode number at $r = 50$ km, $r = 500$ km and $r = 2500$ km. Note that ranges $r = 50$ km and $r = 500$ km only approximately correspond to transmission ranges T50 and T500, and that no axial source data at ranges longer than 1000 km were collected. Note also that the time axes are different in the three subplots.

the difficulty of obtaining robust estimates of time spreads. Modal group time spread diagrams constructed from data are noisy, and contain energy leakage due to array deficiencies making distributions strongly nongaussian. Note also that all modal group time spreads diagrams are plotted in such a way that the dynamic scale on each plot is chosen relative to the maximum intensity over all mode numbers. To estimate $\Delta t_m(r)$ from the data it is necessary to compute the width of each modal distribution relative to its maximum intensity, which is different for each mode. Therefore, it is necessary

to amplify the intensity of each modal arrival (or equivalently choose different maxima of dynamic scale for each mode number) which unavoidably leads to amplification of noise. Also, at 50 km range, numerical simulations reveal bimodal distribution of energy in $(m, t)$. Estimates of $\Delta t_m(r)$ from the data under assumption that each modal arrival is Gaussian are therefore not expected to be accurate.

Now we will present the results of the LOAPEX data processing for transmissions performed with the off-axial acoustic source with 68.2 Hz carrier frequency. These transmissions were performed at all LOAPEX ranges (50 km to 3200 km). Unfortunately, no range-dependent environmental data is available beyond 1000 km range (except at the stations T1600, T2300 and T3200). Therefore, we have chosen to perform numerical simulations using the sound speed profile computed at the SVLA location (this profile is also used for mode processing) on which an internal-wave-induced perturbation [47] is superimposed. Slow variations of the background sound speed structure were neglected.

Figure 35 shows numerical simulations and LOAPEX data at the T50 transmission range with an off-axial acoustic source. Unlike the 75 Hz axial source transmissions, a bimodal distribution in $(m, t)$-space is not seen in the wavefields corresponding to the 68.2 Hz off-axis transmissions. This behavior can be also predicted directly form the time-front intensity plot in $(z, t)$-space. In the case of axial source transmission there are two well-separated arrivals at each depth (except the latest final arrival) and in the case of off-axial source there is only one. This behavior causes the difference in distributions of energy in $(m, t)$. As discussed previously, there is no energy in low mode numbers observed in the simulations. However, in the data relatively high

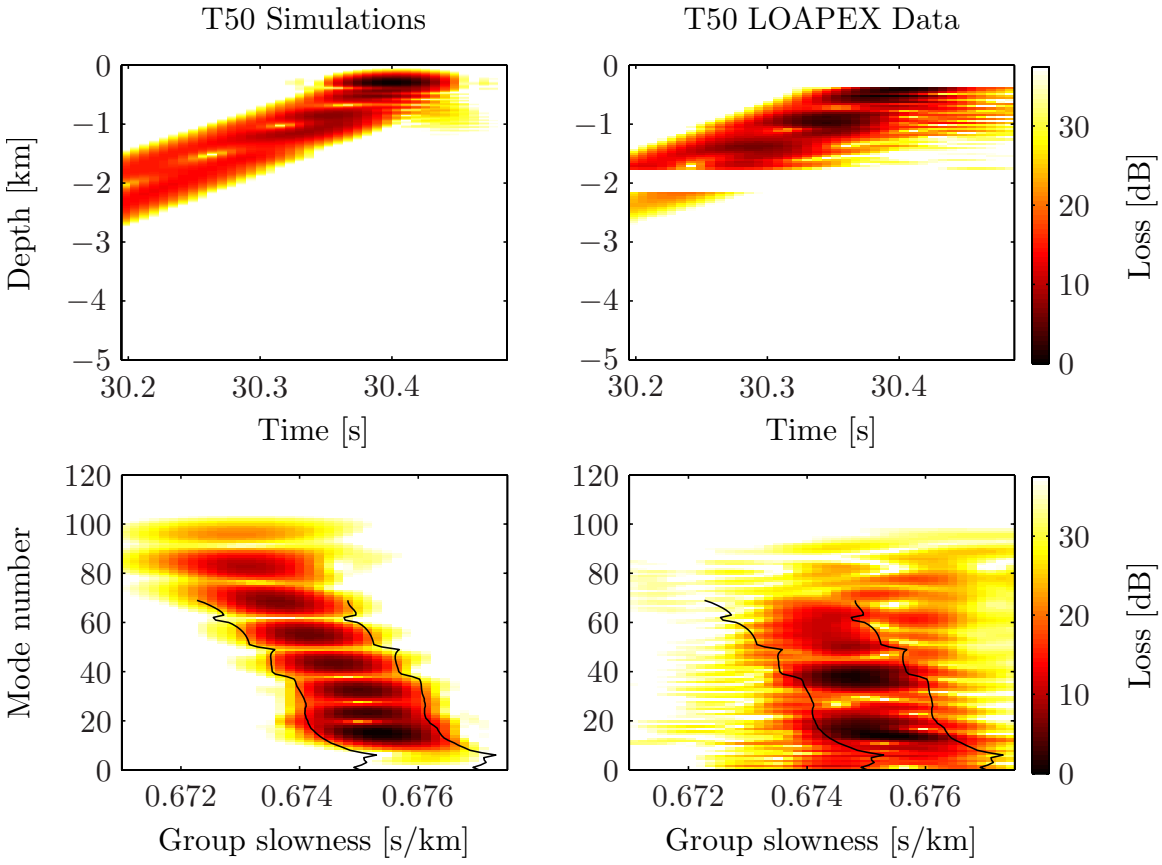


Figure 35. PE simulated time-domain transient wavefield for transmission T50 (upper left panel) for the off-axial source with $f_0 = 68.2$ Hz; LOAPEX time-domain data at T50 station (upper right panel); and corresponding modal group time spread diagrams (lower panels). Black lines are theoretical estimates of modal group time spreads.

intensity arrivals are present almost in all mode numbers. This is almost certainly due to the presence of bottom reflected energy that gives rise to spurious low mode number energy. As in the 75 Hz transmission we have tried to eliminate bottom arrivals, but because these arrivals interfere with the main arrival it is not possible to completely eliminate bottom reflected energy. Apart from these caveats, the agreement between simulations and data mode processed results is seen to be good.

Figure 36 represents numerical simulations and LOAPEX data for T250 transmission range. For this transmission, unlike the T50 transmissions, the reciprocal band-

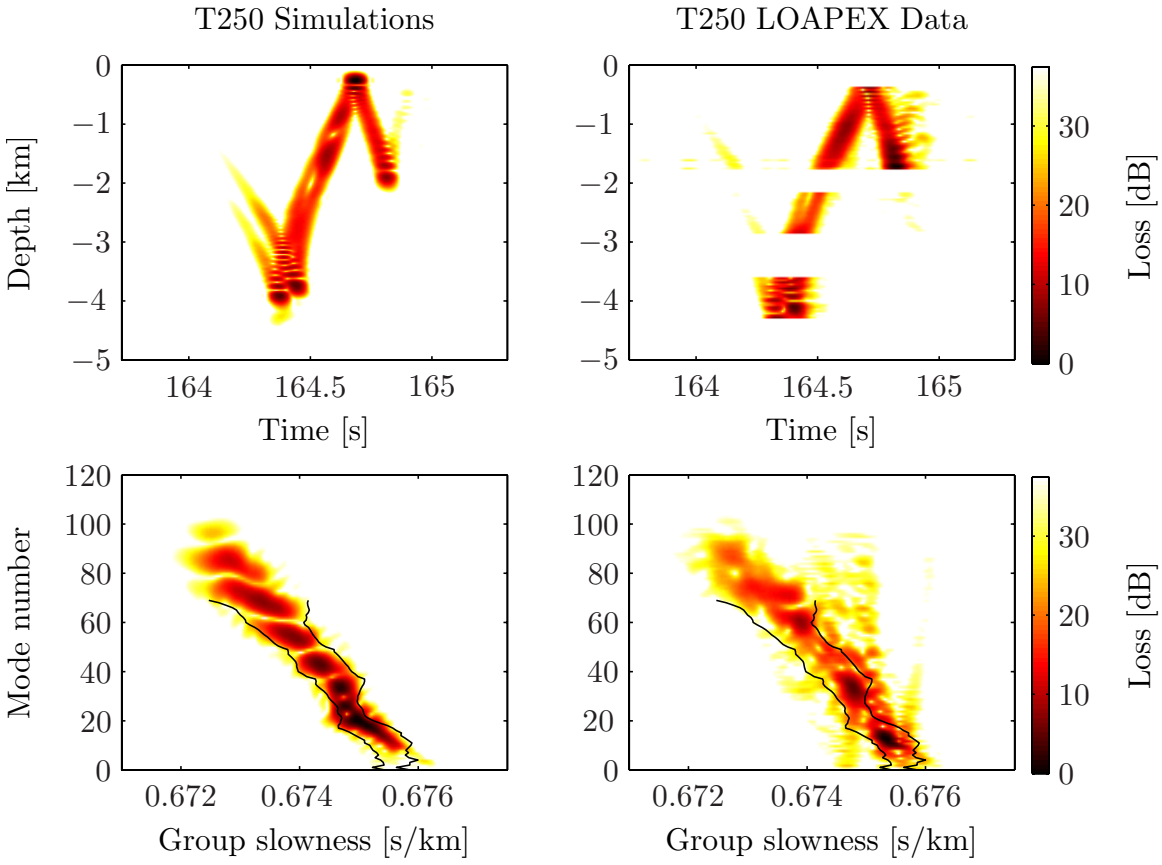


Figure 36. PE simulated time-domain transient wavefield for transmission T250 (upper left panel) for the off-axial source with $f_0 = 68.2$ Hz; LOAPEX time-domain data at T250 station (upper right panel); and corresponding modal group time spread diagrams (lower panels). Black lines are theoretical estimates of modal group time spreads.

width contribution $\Delta t_{bw}$ is not the dominant contribution. Therefore, the qualitative structure of the modal group time spread diagram changes slightly. As predicted, the range of 250 km is still not long enough for the energy to scatter in all low mode numbers, therefore we do not see any energy in the lowest modes. Note that the agreement between simulations and data for low mode numbers is much better than for the T50 transmissions because bottom arrivals are well attenuated at this range and do not interfere with purely refracted energy. The agrement between simulations and data processing results is now very good; even the high intensity regions on the

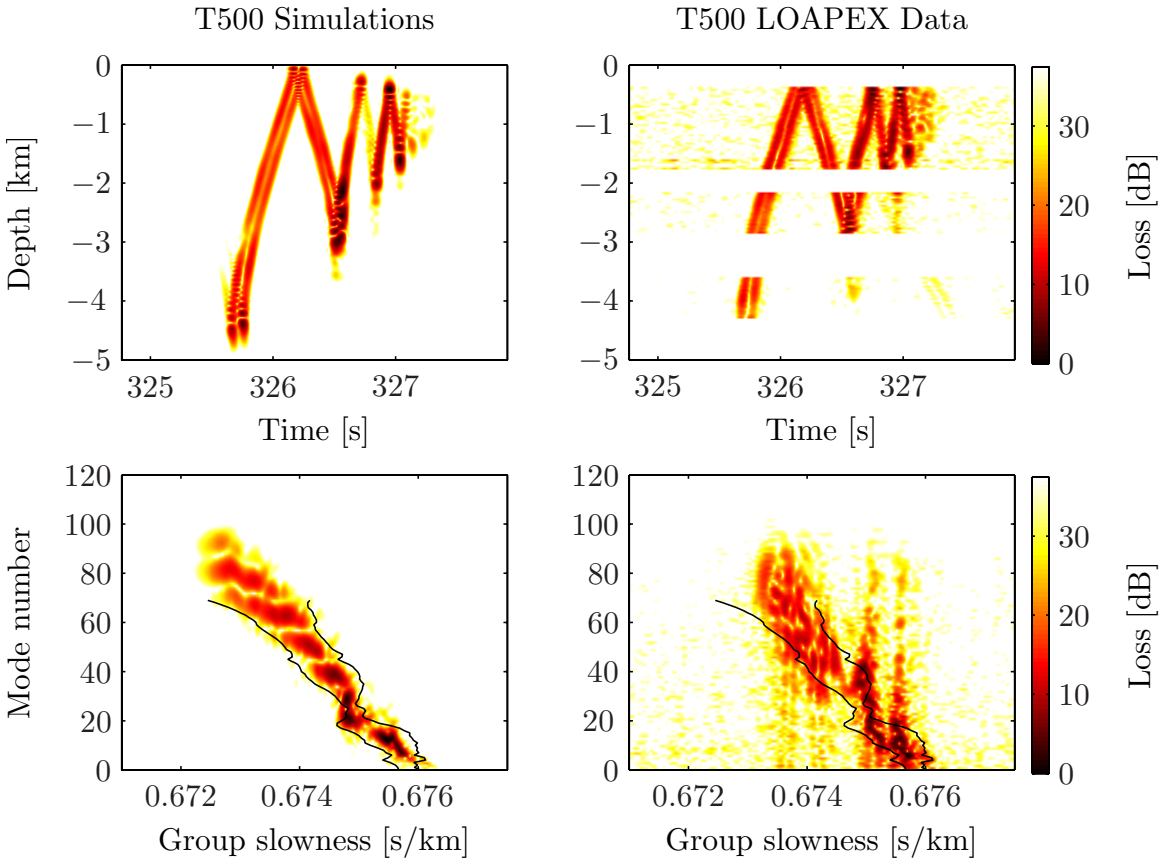


Figure 37. PE simulated time-domain transient wavefield for transmission T500 (upper left panel) for the off-axial source with $f_0 = 68.2$ Hz; LOAPEX time-domain data at T500 station (upper right panel); and corresponding modal group time spread diagrams (lower panels). Black lines are theoretical estimates of modal group time spreads.

modal group time spread diagrams are approximately at the same location. There are two regions on the data processed modal group time spread diagram that have significant modal energy leakage. One is due to the absence of near-surface hydrophones, and another is due to the gap between SVLA and DVLA. But those regions are easily identifiable on the diagram and except for this minor caveat the agreement is good.

Figure 37 shows numerical simulations and LOAPEX data for T500 transmission range. At this range the deterministic dispersive contribution is still dominant. Because of the structure of the arrival time front there are several high intensity arrivals

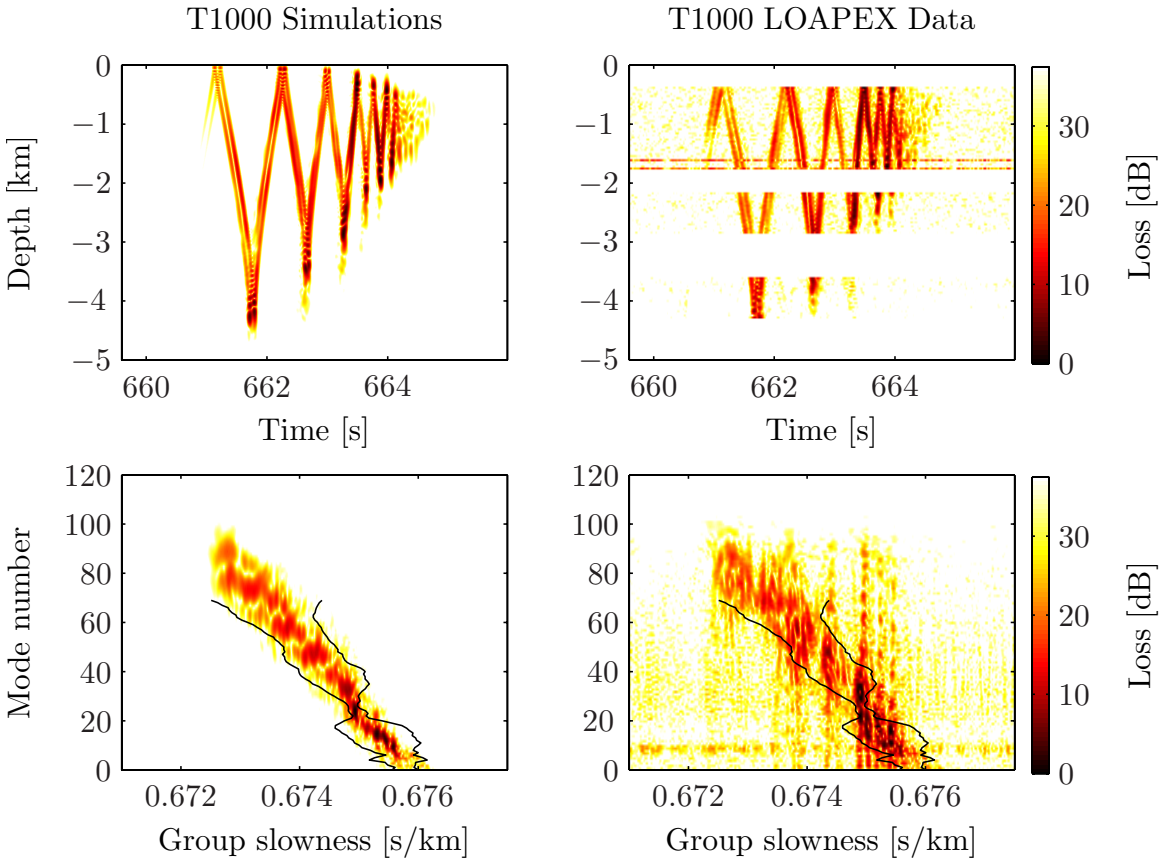


Figure 38. PE simulated time-domain transient wavefield for transmission T1000 (upper left panel) for the off-axial source with $f_0 = 68.2$ Hz; LOAPEX time-domain data at T1000 station (upper right panel); and corresponding modal group time spread diagrams (lower panels). Black lines are theoretical estimates of modal group time spreads.

that are not being capture by VLA, which lead to significant modal energy leakage on the modal group time spread diagram. Despite this observation, the agreement between simulations and data processed results is still good.

Figure 38 shows numerical simulations and LOAPEX data corresponding to the T1000 transmission range. At this transmission range there are two hydrophones on the lower SVLA segment that recorded bad data. (There are three bad hydrophones in 75 Hz transmission data, but the relative intensity of the noise recorded by those hydrophones with respect to intensity of the signal is weaker. Therefore, this defect

is more pronounced on the plot corresponding to 68.2 Hz transmission). Again there are several regions where high intensity arrivals are not captured by VLA. Another point to emphasize for this comparison is that there appears to be more energy in low mode numbers in the data processed results than is predicted in the simulations. This effect also persists at longer transmission ranges. The reason for this behavior is not completely understood. However, there are two probable reasons. First is the lack of knowledge of the precise background sound speed profile. Numerical simulations were performed in two range-dependent environments with internal waves perturbation superimposed: one using the range-independent SVLA sound speed profile and another using the range-dependent sound speed profile that accounts for mesoscale variability along the 1000 km path of the LOAPEX. These simulations suggest that the absence of mesoscale variability in the background sound speed structure could be the cause for the underestimation of scattering into low mode numbers. Another possible explanation, as discussed in Chapter 6, is inadequate description of the IW field, particularly the parameter $\mu$ that appears in Eq. (135).

Figure 39 compares numerical simulations and LOAPEX data for the T1600 transmission range. The agreement between numerical simulations and data processing results is seen to be good. But now we observe that theoretical predictions for modal group time spreads computed from Eq. (129) are too large for some mode numbers. This effect is also observed at longer transmission ranges. As discussed previously, the problem is likely a shortcoming of an approximation made in the theory; in the regions of rapid variations of $\beta(m, \sigma_0)$, some average value of $\beta$ should be used. But these results were constructed using the value of $\beta$ corresponding to the final mode

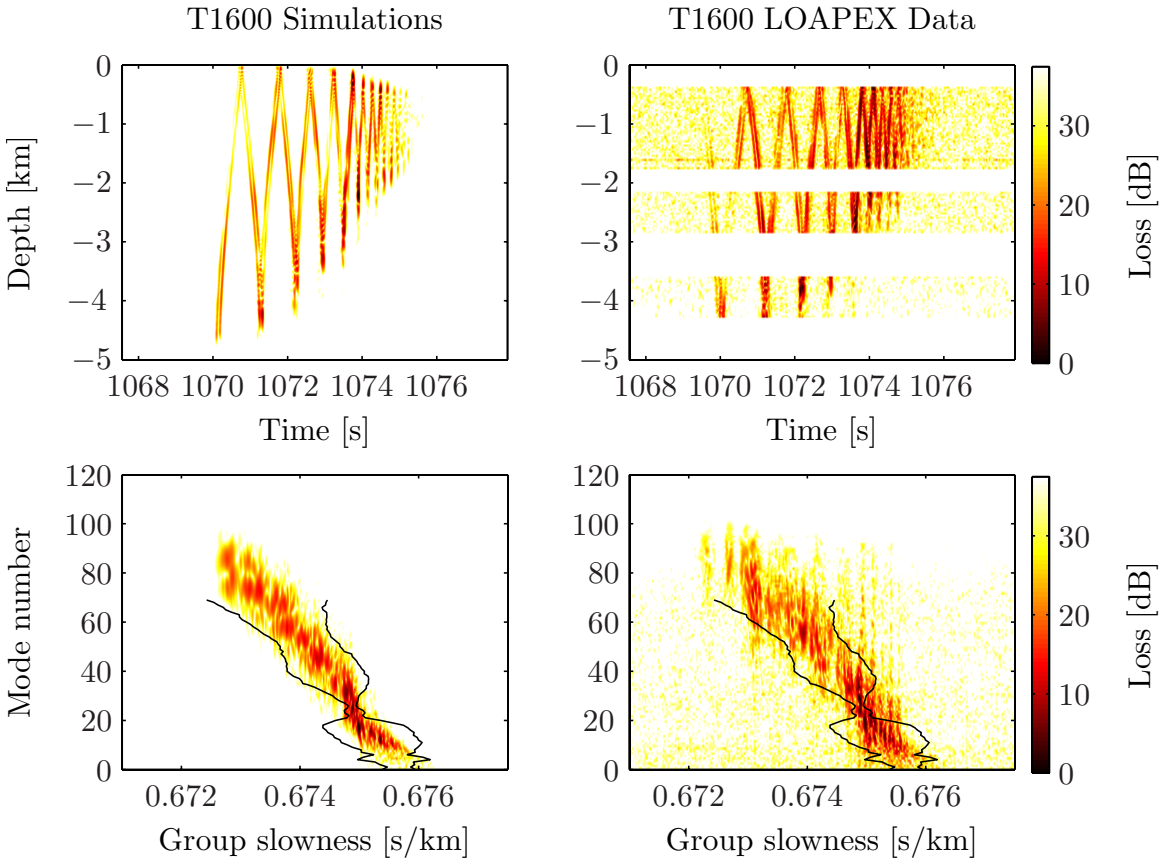


Figure 39. PE simulated time-domain transient wavefield for transmission T1600 (upper left panel) for the off-axial source with $f_0 = 68.2$ Hz; LOAPEX time-domain data at T1600 station (upper right panel); and corresponding modal group time spread diagrams (lower panels). Black lines are theoretical estimates of modal group time spreads.

number. If the absolute value of the final $\beta$ is larger than the absolute value of the average (which is the case), the estimated values of time spread will be larger than those observed. Since both deterministic and scattering induced contributions are proportional to $\beta$ and grow with range, this error increases with range.

Figure 40 shows numerical simulations and LOAPEX data for the T2300 transmission range. At this transmission range, the data recorded at the lower section of the SVLA is completely missing. With such a large gap in the receiving array, mode processing techniques should not be expected to provide meaningful results.

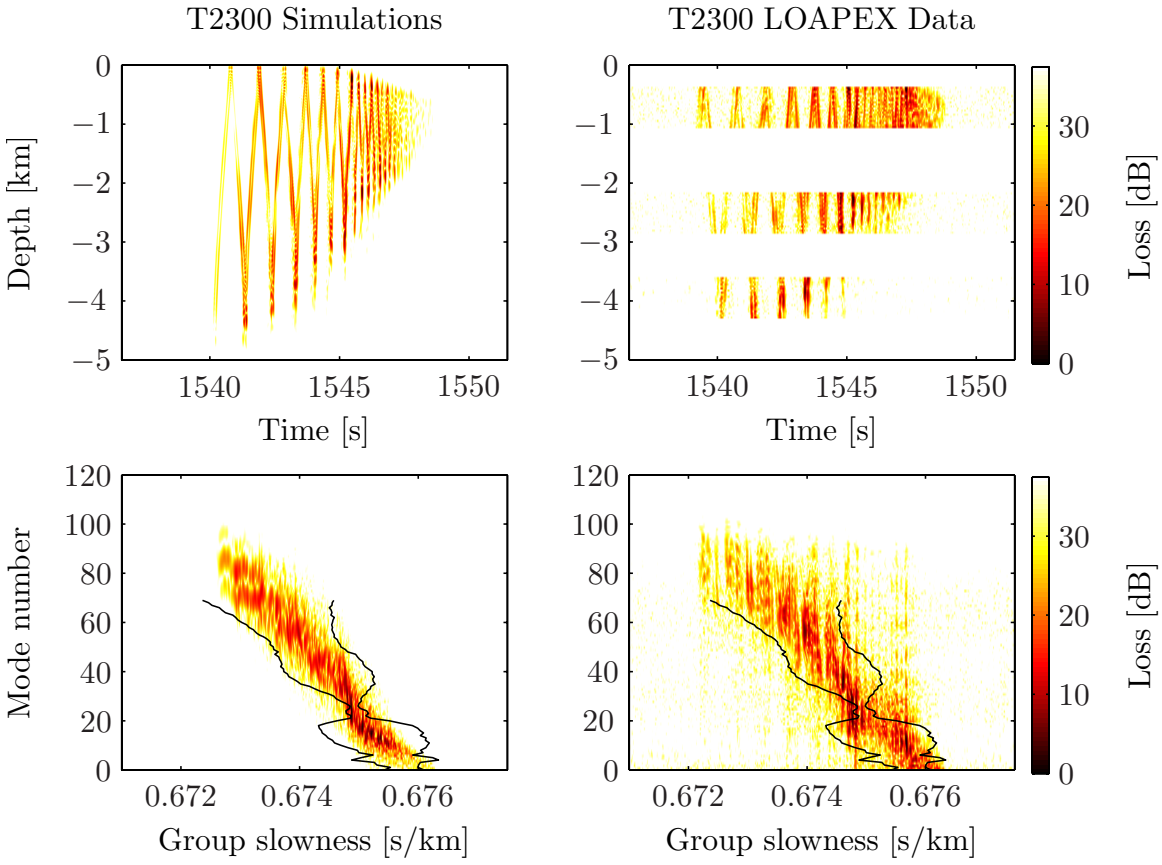


Figure 40. PE simulated time-domain transient wavefield for transmission T2300 (upper left panel) for the off-axial source with $f_0 = 68.2$ Hz; LOAPEX time-domain data at T2300 station (upper right panel); and corresponding modal group time spread diagrams (lower panels). Black lines are theoretical estimates of modal group time spreads.

However, it is seen that even with such a big deficiency in the receiving array, the mode processing results are fairly good.

Figure 41 shows numerical simulations and LOAPEX data for the T3200 transmission range. This is the longest transmission range that was used in the experiment. At this range the signal to noise ratio is low. Therefore both the time front plot and modal group time spread diagram are very noisy. As discussed earlier, the theoretical predictions significantly overestimate modal group time spreads for some mode numbers. However, the overall agreement between theory, numerical simulations and

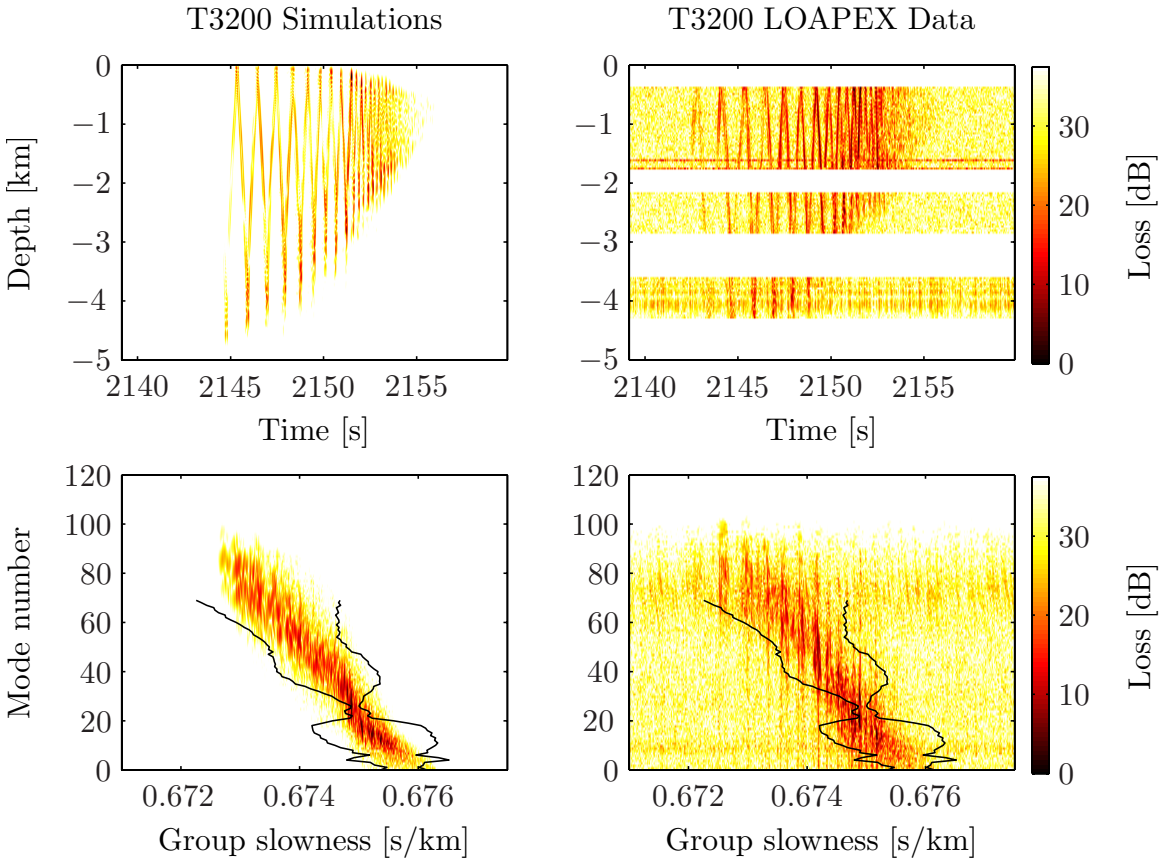


Figure 41. PE simulated time-domain transient wavefield for transmission T3200 (upper left panel) for the off-axial source with $f_0 = 68.2$ Hz; LOAPEX time-domain data at T3200 station (upper right panel); and corresponding modal group time spread diagrams (lower panels). Black lines are theoretical estimates of modal group time spreads.

data processing results is reasonably good.

We now consider the range evolution of modal group time spreads for fixed mode numbers. Figure 42 is the same as Fig. 23 in Sec. 4.8, but now $\Delta t_m(r)$ estimated from the LOAPEX data are also plotted with red dots for $m = 17$, 25 and 56. Agreement between simulated and data-based estimates of $\Delta t_m(r)$ is generally quite good, but as discussed previously, some systematic deviations between simulations and theory are observed. Recall that the data-based estimate from T2300 transmission range is unreliable because of the significant array deficiencies associated with that data set.

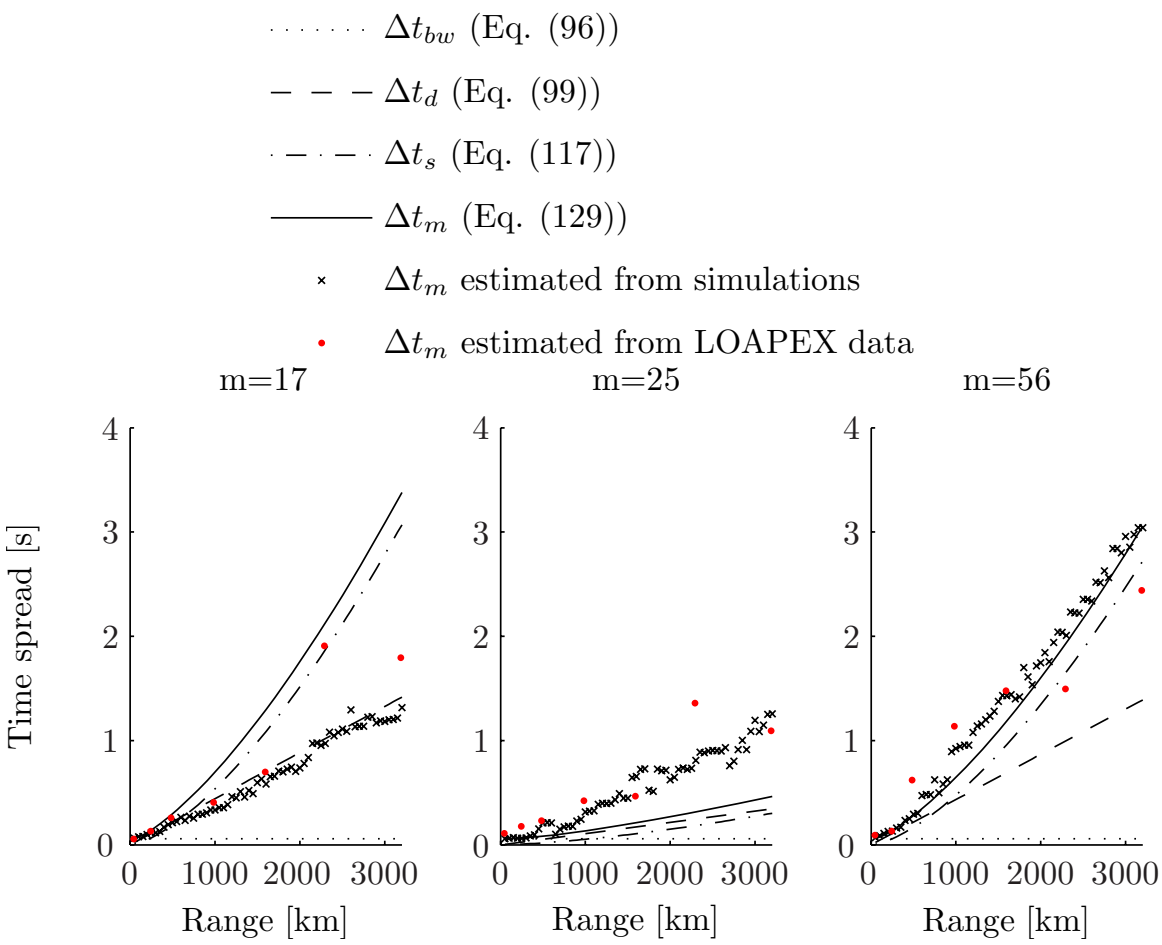


Figure 42. Predicted, simulated and measured estimates of modal group time spreads $\Delta t_m$ vs range for three values of $m$.

Figure 43 is also the same as Fig. 24 in Sec. 4.8, but with data processing estimates plotted at all three ranges. Note that transmission ranges for T50, T500 and T2300 were 45 km, 484 km and 2290 km, while the simulations were performed at ranges of 50 km, 500 km and 2500 km, respectively. This mismatch introduces some error. At all three ranges there is a difficulty of estimating modal group time spreads for low mode numbers due to inadequate signal to noise. Recall also that the presence of bottom reflected energy in the T50 data led to considerable uncertainty in the low mode number estimates of $\Delta t_m$ for these receptions. In spite of these caveats,

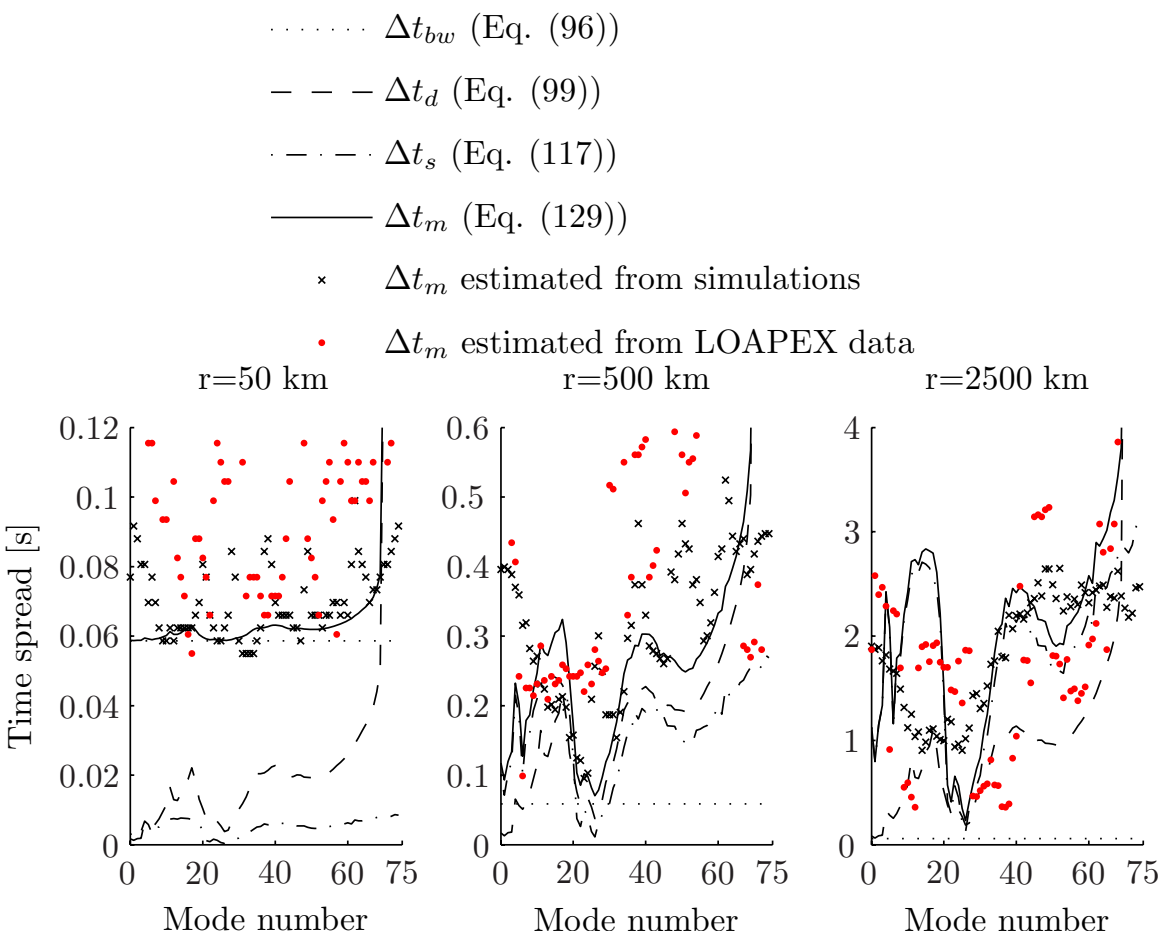


Figure 43. Predicted simulated and measured estimates of modal group time spreads $\Delta t_m$ vs mode number at $r = 50$ km, $r = 500$ km and $r = 2500$ km. Note that the time axes are different in the three subplots.

the agreement between theory, simulations and data seen in Fig. 43 is generally good.

# 6 Sound scattering by internal waves revisited

The work presented in this chapter was motivated by the observation that, using an off-axial source, less energy is scattered into the low mode numbers at long range in our simulations than in the measured LOAPEX wavefields. Figures 38-41 show time-domain fields and modal group time spread diagrams for off-axial source transmissions T1000-T3200. Comparison of modal group time spread diagrams computed for simulated data and actual LOAPEX data reveals that that the amount of energy scattered into low mode numbers as a function of range that is observed in the LOAPEX data is greater than in simulations. We refer to this effect as "anomalous scattering". It is expected that bottom interactions, mixed layer processes, mesoscale variability and other non-internal-wave mechanisms (for example, internal tides) play only a minor role in this process. It is now generally accepted that internal-wave-induced sound speed fluctuations is the dominant source of high frequency (with time scales less than approximately 1 day) variability of acoustic wavefields in the ocean [18, 51, 52]. In this chapter a possible explanation for the anomalous scattering of energy into the region close to the sound channel axis is presented.

## 6.1 Internal-wave-induced sound speed fluctuations

Internal waves have been studied by many investigators [14, 19, 21, 47, 53, 54, 55, 56, 57]. In this work we are not going to describe any details of the internal-wave-induced sound speed perturbation model. Here we only mention that the numerical model described in [47] is used for simulation of realizations of sound speed perturbations.

This model is based on the relation between sound speed perturbation $\delta c$ and internal-wave-induced vertical displacement $\xi$ of a fluid parcel

$$\delta c = \left(\frac{\partial c}{\partial z}\right)_\theta \xi \approx c\left(\frac{\mu}{g}\right) N^2 \xi, \tag{135}$$

where $\left(\frac{\partial c}{\partial z}\right)_\theta$ is the potential sound-speed gradient, $\mu$ is the acoustic fluctuation strength parameter, $g = 9.8$ m/s$^2$ is the gravitational acceleration, $c$ is sound speed, and $N$ is buoyancy frequency. Statistics of $\xi(x, y, z, t)$ are described by the empirical GM internal-wave spectrum [19, 54, 55] and depends on several parameters such as the number of internal wave modes $j_{\max}$, the maximum horizontal wavenumber in the spectrum $k_{\max}$, or equivalently, the minimum wavelength that is resolved by the model $\lambda_{\min}$, the reference buoyancy frequency $N_0$, the thermocline depth scale $b$ and some other empirical parameters. It is shown in the model [47] that internal-wave-induced vertical displacement scales like $N^{-1/2}$, i.e.

$$\xi_{rms} \sim \left(\frac{E}{N(z)}\right)^{1/2}, \tag{136}$$

where $E = 6.3 \times 10^{-5}$ is empirical dimensionless constant representing the strength of the internal wavefield. The sound speed perturbation $\delta c$ scales like $N^{3/2}$

$$\delta c \sim \mu E^{1/2} N(z)^{3/2}. \tag{137}$$

Thus, the sound speed perturbation is directly proportional to the acoustic fluctuation strength parameter $\mu$ and perturbation strength parameter $E^{1/2}$. Therefore, it is

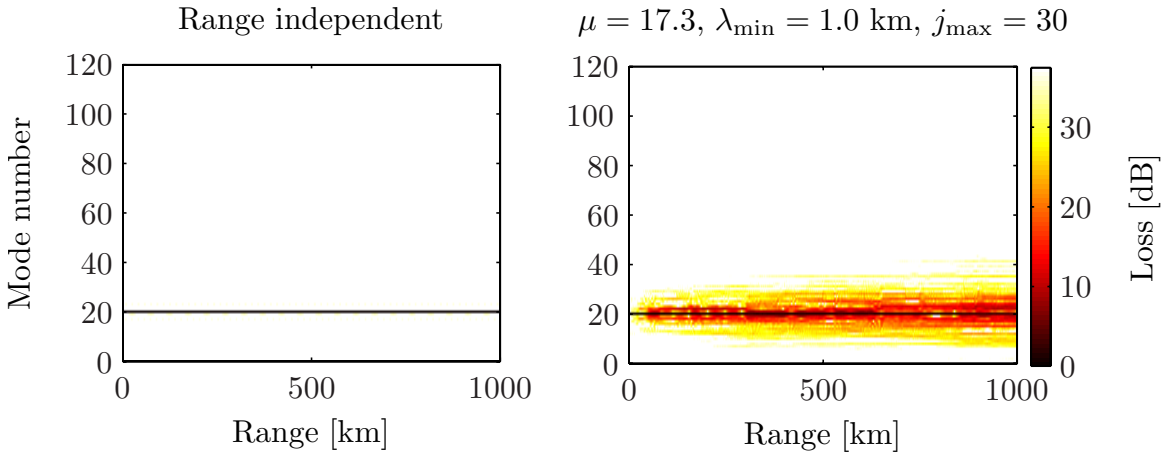


Figure 44. Single mode $m = 20$ starting field cw simulations in the range-independent environment (left panel) and in the range-dependent environment with internal-wave-induced perturbation produced with $\mu = 17.3$, $\lambda_{\min} = 1.0$ km and $j_{\max} = 30$ (right panel).

expected that $\delta c$ should be more sensitive to the variations of $\mu$, rather than variations in $E$. In Sec. 6.2 several hypotheses attempting to explain the anomalous scattering will be tested numerically.

## 6.2 Numerical simulations

For numerical simulations a single mode starting field corresponding to $m = 20$, at the frequency $f_0 = 68.2$ Hz in the LOAPEX-like environment was constructed. This mode has its upper turning depth close to 350 m and therefore it is strongly excited by the LOAPEX off-axial source.

The first numerical test was done in a range-independent environment (Fig. 44, left panel), which confirmed that the model correctly predicts that all energy that was initially excited in mode $m = 20$ stays in the same mode at all ranges. Then another cw computation was performed in the range-dependent environment with internal-wave-induced sound speed perturbation superimposed on the background

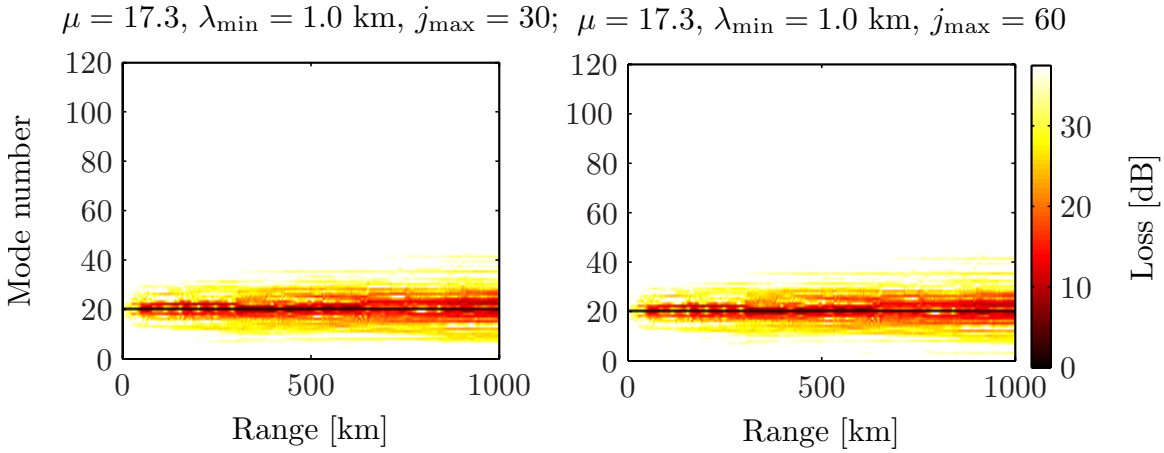


Figure 45. Single mode $m = 20$ starting field cw simulations in the range-dependent environments with internal-wave-induced perturbation produced with $\mu = 17.3$, $\lambda_{\min} = 1.0$ km and $j_{\max} = 30$ (left panel) and $\mu = 17.3$, $\lambda_{\min} = 1.0$ km and $j_{\max} = 60$ (right panel).

sound speed structure with constant $\mu = 17.3$, the cutoff wavelength $\lambda_{\min} = 1$ km and internal wave field composed of 30 modes ($j_{\max} = 30$). The distribution of energy as a function of range and mode number is shown in Fig. 44 on the right panel.

Figure 45 compares similar cw computations with $j_{\max} = 30$ (left panel) and $j_{\max} = 60$ (right panel). It is concluded that the number of internal wave modes used in the model almost does not affect the amount of energy being scattered provided that the choice of parameter $j_{\max}$ is not too small. Figure 45 leads us to conclude that the cause of anomalous diffusion is not our choice of too small a value of $j_{\max}$.

Another numerical test was performed with two different values of the wavenumber cutoff in the spectrum of internal waves model. Figure 46 shows two different simulation results produced for two different choices of $\lambda_{\min}$, $\lambda_{\min} = 1.0$ km (left panel) and $\lambda_{\min} = 0.1$ km (right panel). This figure suggests that this parameter also does not affect the amount of scattered energy provided a sensible choice of $\lambda_{\min}$ is made.

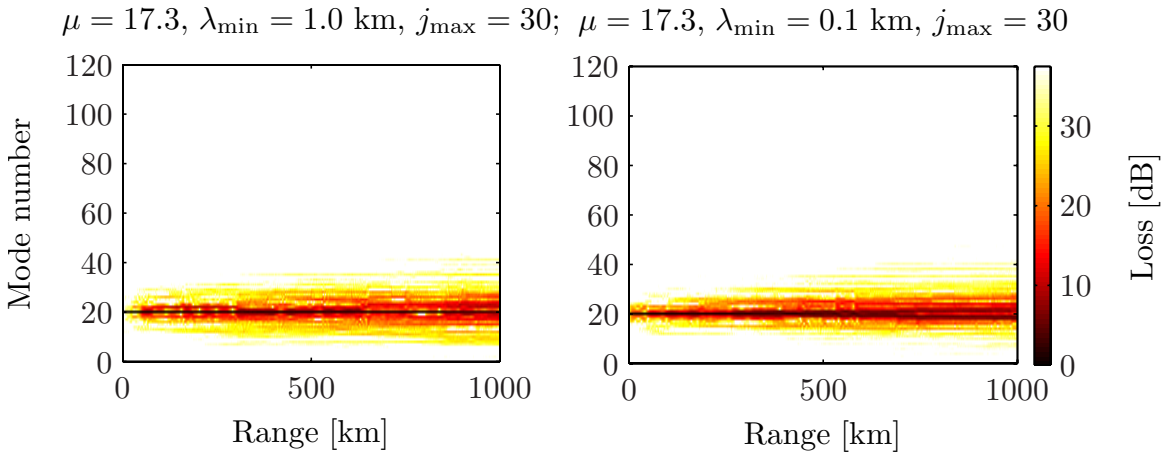


Figure 46. Single mode $m = 20$ starting field cw simulations in the range-dependent environments with internal-wave-induced perturbation produced with $\mu = 17.3$, $\lambda_{\min} = 1.0$ km and $j_{\max} = 30$ (left panel) and $\mu = 17.3$, $\lambda_{\min} = 0.1$ km and $j_{\max} = 30$ (right panel).

After these tests were performed it was decided to investigate whether our assumption that $\mu$ in Eq. (135) is constant accurately approximates realistic ocean conditions. In the work by Noble and Flatté [53] this parameter was computed for different water masses and was shown to vary significantly from $\mu = 5$ in the North Pacific to $\mu = 34$ in North Atlantic. In the North Pacific ocean, where the LOAPEX experiment was conducted, this parameter was estimated at three different depths and the values are $\mu = 19$ at 275 m depth, $\mu = 21$ at 550 m depth and $\mu = 7$ at 850 m depth. It was decided to compute this parameter using hydrographic data measured along the LOAPEX track. By definition

$$\mu = -\frac{\rho}{c}\frac{\partial c_\theta}{\partial \rho_\theta}. \tag{138}$$

Variations in density $\rho$ and sound speed $c$ are small, so to an excellent approximation, both can be replaced by their depth averages. In order to compute the depth depen-

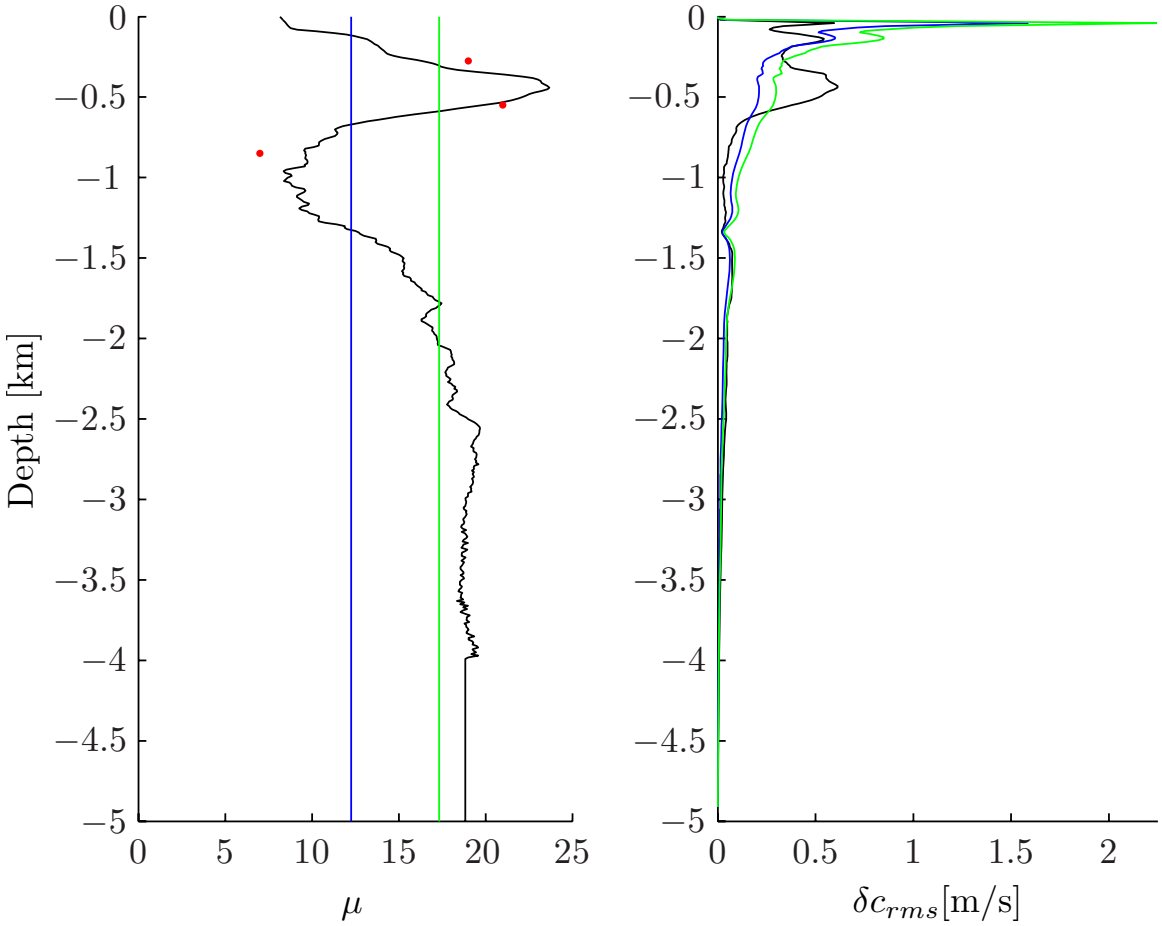


Figure 47. Three different profiles $\mu(z)$ (left panel) and corresponding rms sound speed perturbations produced by the internal-wave model (right panel). Red dots are values of $\mu$ given by Noble and Flatté [53] for the North Pacific ocean water mass.

dence of the parameter $\mu$, it is required to compute $c_\theta(z)$ and $\rho_\theta(z)$. The details of this computation are discussed in the Appendix. Many computational steps described there can be found in Ref. [58]. The sound speed $c(z)$ was computed using nine-term equation for sound speed in the oceans introduced by Mackenzie [59]. Figure 47 shows three different profiles of $\mu(z)$ and the corresponding rms sound speed perturbation $\delta c_{rms}(z)$ produced with the internal wave model. The two choices of $\mu(z) = \text{const}$ (blue and green lines) correspond to $\mu = 12.25$ and $\mu = 17.3$, respectively. The black line corresponds to $\mu(z)$ computed from LOAPEX environmental data. Three red

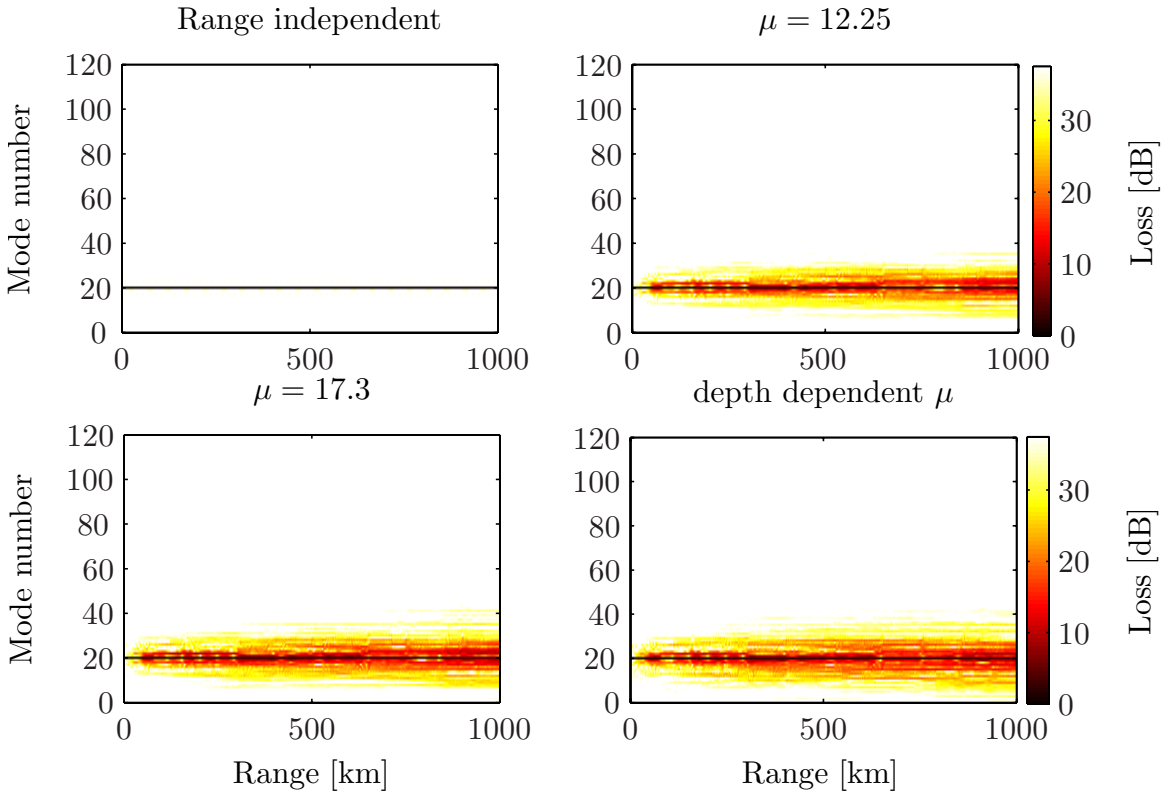


Figure 48. Single mode $m = 20$ starting field cw simulations in the range-independent environment (upper left panel) and in the range-dependent environments with $\mu = 12.25$, $\mu = 17.3$ and depth-dependent $\mu(z)$ computed from environmental data.

dots are values given in [53]. It is seen from the right panel of Fig. 47 that $\delta c_{rms}(z)$ differs significantly for the depth-dependent $\mu(z)$ vs constant $\mu$. There is significantly more energy contained in the produced sound speed perturbation field around 500 m depth, which leads to stronger scattering of energy among modes with upper turning depth around 500 m.

Figure 48 shows cw simulations performed with a single mode ($m = 20$) starting field for four different choices of $\mu(z)$. The upper left panel is range-independent case (which is equivalent to $\mu = 0$); the upper right panel corresponds to $\mu = 12.25$; the lower left panel corresponds to $\mu = 17.3$; and the lower right panel corresponds to the depth-dependent $\mu(z)$. It is seen that simulation corresponding to the depth-

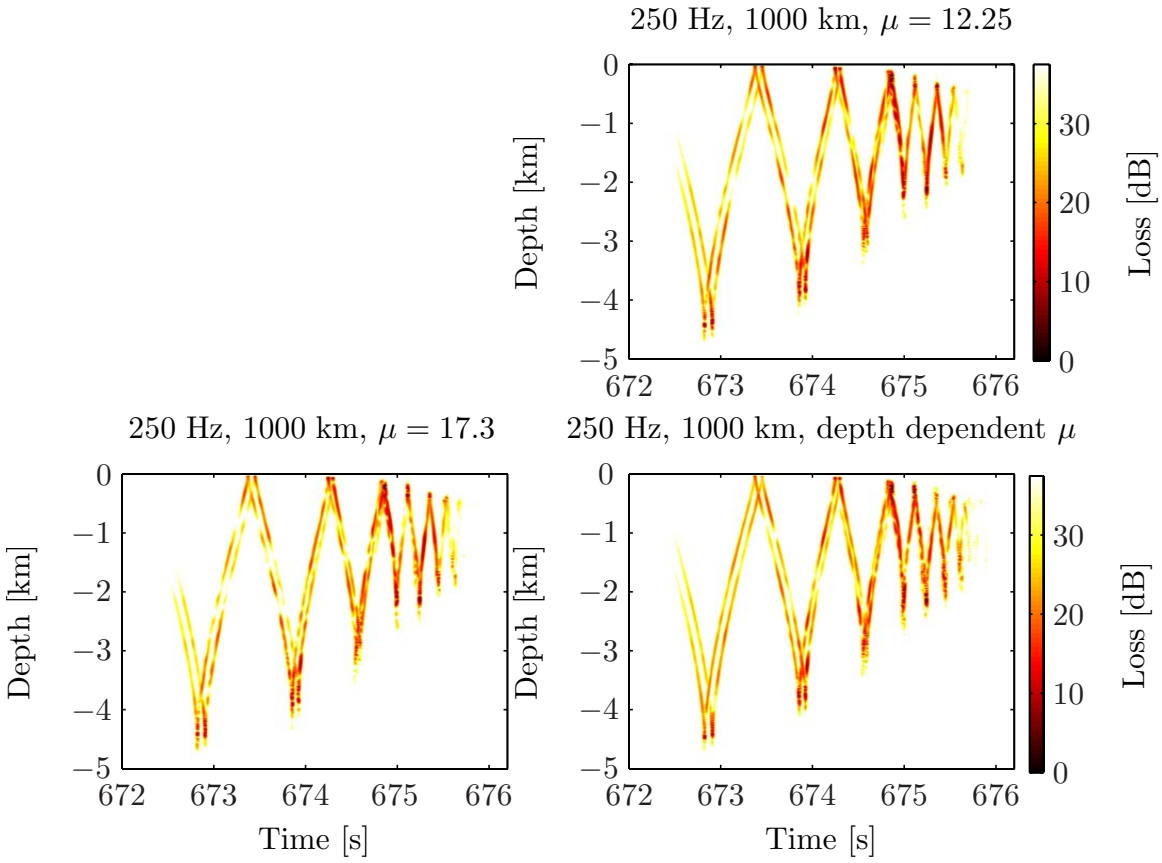


Figure 49. PE simulations performed in range-dependent environments with $\mu = 12.25$, $\mu = 17.3$ and depth-dependent $\mu(z)$. The central frequency of the source is $f_0 = 250$ Hz in these simulations.

dependent $\mu(z)$ produces more scattering into mode numbers with $m < 20$ than the others. Note that the total integrated energy of the perturbation field corresponding to the depth-dependent $\mu(z)$ is equivalent to the energy corresponding to the field computed with $\mu = 12.25$, and the choice of $\mu = 17.3$ produces a perturbation field that has twice the total integrated energy as the other fields.

In order to illustrate this effect more clearly, higher frequency simulations (with a source frequency of $f_0 = 250$ Hz) were performed. Figure 49 shows three time-domain acoustic fields corresponding to transmission range of 1000 km with the same three choices of $\mu(z)$: $\mu = 12.25$ (upper right panel); $\mu = 17.3$ (lower left panel); and

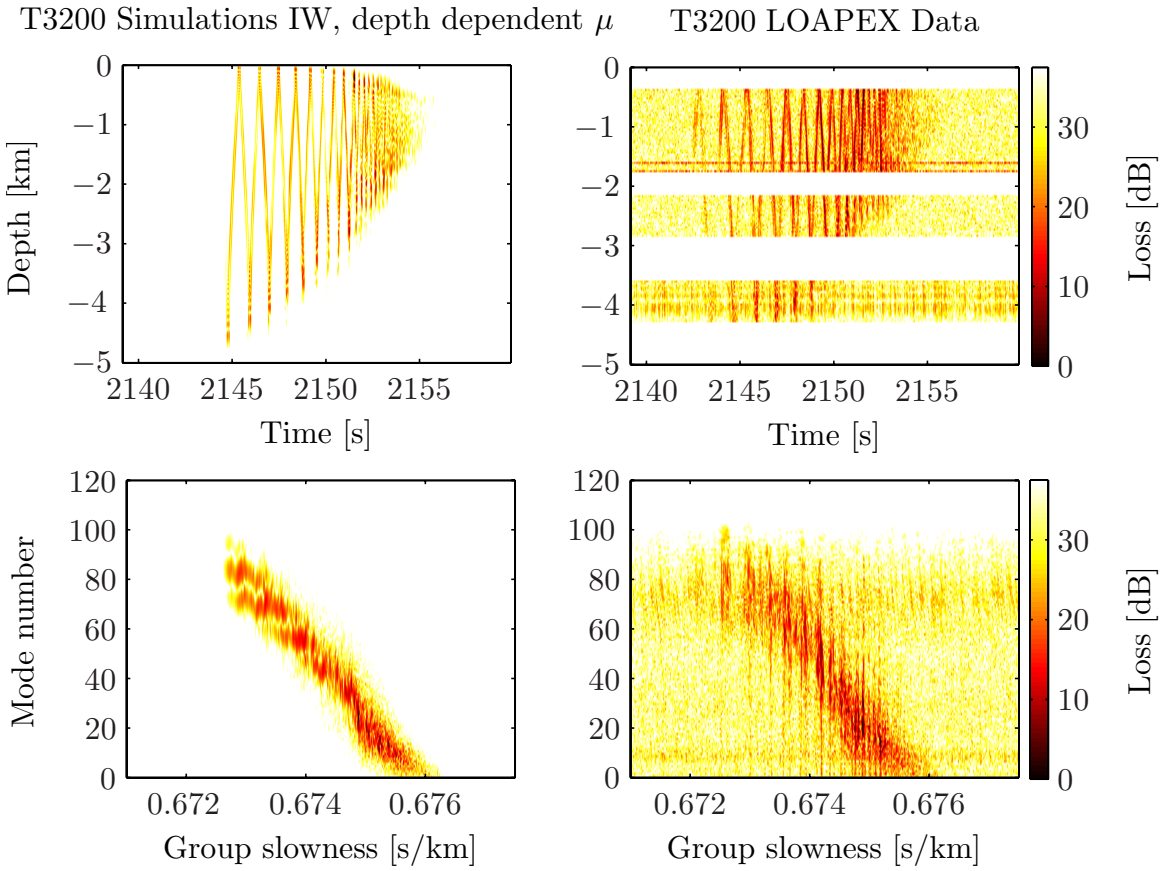


Figure 50. PE simulated time-domain transient wavefield for transmission T2300 (upper left panel) for the off-axial source with $f_0 = 68.2$ Hz in the environment constructed with the use of depth-dependent $\mu(z)$, LOAPEX recorded time-domain data at T2300 station (upper right panel) and corresponding modal group time spread diagrams. Black lines are theoretical estimates of modal group time spreads.

the depth-dependent $\mu(z)$ (lower right panel). The "anomalous scattering" into low mode numbers in these plots appear as an extra time-front branch. This extra branch is most clearly seen in the plot corresponding to the depth-dependent $\mu(z)$.

Figure 50 compares simulations performed with the depth-dependent $\mu(z)$ shown if Fig. 47 and LOAPEX data corresponding to the T3200 station transmission range. The amount of energy being scattered into low mode numbers shown in the simulations has increased relative to the constant $\mu = 17.3$ calculation (shown in Fig. 41). The amount of scattered energy observed in the LOAPEX data still remains slightly

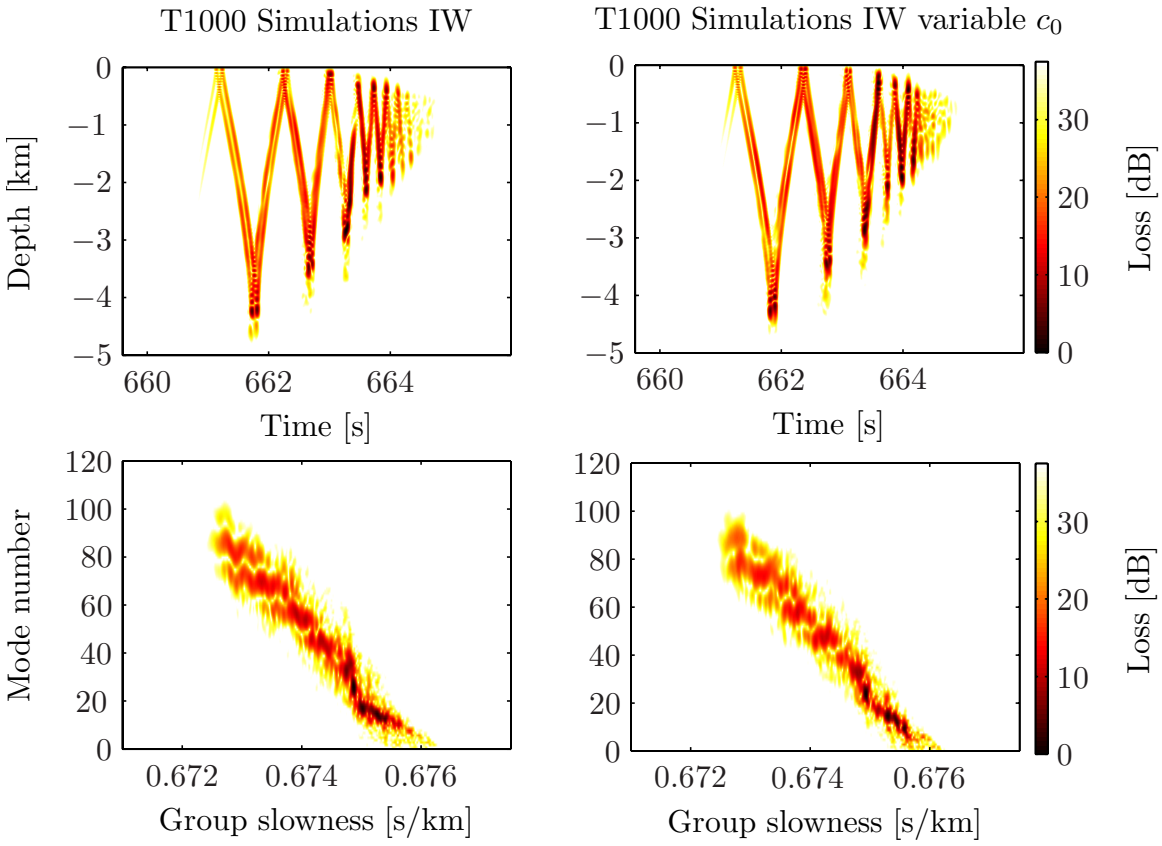


Figure 51. PE simulated time-domain transient wavefields for transmission T1000 (upper panels) for the off-axial source with $f_0 = 68.2$ Hz with range-independent background sound speed structure (left panel), and slowly-varying background sound speed structure computed from environmental data (right panel). Corresponding modal group time spread diagrams are shown in two lower subplots.

larger than predicted by the simulations. In spite of this slight underprediction of scattered energy, the simulations shown strongly suggest that correctly computing $\mu(z)$ from hydrographic data correctly accounts for most of the "anomalous scattering" that was identified earlier.

Another scattering mechanism that may contribute to "anomalous scattering" is the presence of mesoscale variability in the background sound speed profile. Figure 51 compares two different simulations performed with range-independent background sound speed structure (left panels) and slowly-varying range-dependent sound speed

computed from the environmental data along the LOAPEX track (right panels). This figure shows that slightly more scattering into low mode numbers is observed when the slow background sound speed structure variability is present.

The conclusion from this analysis is that the depth dependence of $\mu(z)$ is important and should not be neglected. It was observed that at 75 Hz wavefields show very little sensitivity to a reasonable choices of wavelength cutoff parameter $\lambda_{\min}$ and number of internal wave modes used $j_{\max}$. The combination of weak mesoscale variability and internal-wave-induced sound speed fluctuations with realistic $\mu(z)$ may account for the observed scattering in the LOAPEX data.

# 7 Discussion and summary

In this work a theory of modal group time spreads in weakly range-dependent deep ocean environments has been developed. The purpose of the work described here is to provide a theoretical framework for a mode-based interpretation of low-frequency broadband measurements on a vertical array at multiple ranges in the deep ocean and test obtained theoretical results and numerical simulations results against recent measurements. It was assumed that the environment consists of a range-independent background, on which a small-scale perturbation is superimposed. The perturbation, due, for example, to internal waves, was assumed to be sufficiently weak that mode coupling is predominantly local in mode number and can be approximately modelled as a diffusive process. The extension to a diffusive process in the presence of a reflecting boundary which is appropriate for analysis of low mode numbers was also briefly discussed. It has been shown that there are three contributions to modal group time spreads: the reciprocal bandwidth $\Delta t_{bw} = (\Delta f)^{-1}$, a deterministic dispersive contribution $\Delta t_d \sim I(f_0, m)\,\beta(m, \sigma_0)\, r\Delta f$, and a scattering-induced contribution $\Delta t_s \sim \beta(m, \sigma_0)\, r^{3/2}$. It was argued, but not shown rigorously, that these three contributions combine in quadrature; this dependence was shown to be in good agreement with simulations. Under most experimental circumstances the transmission range is sufficiently large for the term $\Delta t_{bw}$ to be negligible. Because both $\Delta t_d$ and $\Delta t_s$ are proportional to $\beta(m, \sigma_0)$ it might be difficult to experimentally distinguish these contributions from each other. Note, however, that $\Delta t_s$ is expected to dominate at long range, and that at any range $\Delta t_d$ can be reduced by reducing $\Delta f$

(by band-pass filtering recorded pressure time histories). The observation that both $\Delta t_d$ and $\Delta t_s$ are proportional to $\beta(m, \sigma_0)$ is noteworthy inasmuch as these quantities constitute two among many properties of both deterministic and scattering-induced contributions to wavefields that are controlled by $\beta(m, \sigma)$ or its ray counterpart $\alpha(I)$ [29]. This list includes travel time dispersion [29], ray amplitudes at long-range [29], scattered ray amplitudes / ray stability [25], both constrained and unconstrained scattered ray travel time spreads [26, 30], both spatial and temporal spreads of narrow beams with and without scattering [60], and both diffractive (Fresnel zone width) and scattering-induced contributions to the effective width of a ray [48]. The combination of all of these results as well as simulations presented in this work shows rather conclusively that in nearly stratified environments wavefield structure and stability is largely controlled by $\beta(m, \sigma)$ (or its ray counterpart $\alpha(I)$).

A significant part of this work has been devoted to full-wave numerical simulations. Some of these simulations were done in the canonical environment C0 or slightly modified canonical sound speed profile C17. Those numerical results support and illustrate the theory that has been developed. It has been shown that even simple asymptotic modal theory can be utilized to correctly predict the modal group time spreads produced using full-wave numerical simulations or measured experimentally. Other numerical simulations were performed in the LOAPEX-like environment with parameters chosen to be as similar as possible to the LOAPEX experiment. These simulations play an important role in interpreting experimental results. Also these simulations provide valuable information about possible limitations of the data analysis used and suggest different ways to improve this analysis.

Experimental acoustic data was collected during the 2004 LOAPEX experiment [11]. The data set is very extensive and much of it is still to be processed. Part of these data were analyzed and results of the mode processing are presented in this work. Two types of transmissions were analyzed: 1) transmissions with 75 Hz central frequency of the acoustic source deployed at 800 m depth (near the sound channel axis) performed for ranges up to 1000 km; and 2) transmissions with 68.2 Hz central frequency acoustic source deployed at 350 m depth (far from sound channel axis) performed for ranges up to 3200 km. Some fundamental differences in the receptions corresponding to different transmission types are discussed. It is shown that mode processing applied to the LOAPEX data allows estimation of modal group time spreads for almost all propagating modes for all transmission ranges. These estimations are shown to be in good agreement with theoretical predictions and estimations based on numerical modelling.

Different challenges associated with processing of the experimental data has been discussed in this work. Special attention has been paid to the study of the influence of receiving array deficiencies on the effectiveness of the mode processing. A justification for the use of a "pseudo-array", in which the SVLA and DVLA measurements were treated as if they were collected on the same array (after a suitable time shift is applied), for mode processing was given. The use of both arrays together for mode processing allows one to significantly improve the estimates for modal group time spreads for modes which are poorly sampled by one of arrays. The influence of other deficiencies such as sparse sampling in vertical direction has also been discussed.

In an attempt to provide an explanation for what we have described as "anomalous

scattering" we have revisited the problem of modelling internal-wave-induced sound speed fluctuations. It was argued that the widely used simple assumption that the potential sound speed gradient is proportional to $N(z)^2$ is often inadequate.

Several extensions to the results presented here will be explored in conjunction with analysis of the LOAPEX measurements. First, the preliminary data analysis results presented here need to be completed. More receptions need to be processed and statistics of modal group time spread estimates need to be quantified. Second, the dependence of the effective action diffusivity $B$ on mode number (or action) is worthy of a more thorough and systematic investigation than has been provided here. The third possible extension involves simplifying the $\beta$-weighted sum (128) to get an improved estimate of $\delta t_s$, and in turn $\Delta t_s$. This problem is analogous to a weighted random walk process. In the presence of strong local variations in $\beta(I)$, this task may prove to be very difficult.

For the analysis of experimental data it is desirable to explore the use of different mode processing techniques, other than direct projection. One of these methods is the so-called optimal modal beamforming [61], which is based on a generalized least-squares mode beamformer, capable of incorporating physical space–time constraints on the propagation of sound. Another possible approach is to use a short-time Fourier transform [12, 13] framework, which is based on separation of the signal into a set of subbands and estimation of modal time series in each band. The results are time-varying mode spectra that can be used to examine the frequency-dependent structure in the signals. It is important to emphasize that our focus is on transient wavefields – some processing algorithms are expected to be better suited to a time-domain analysis.

It is not clear whether signal processing techniques that are optimal in some sense for cw wavefields are also the best option for transient wavefields.

Another very important extension of the data analysis is to quantify the temporal coherence of the LOAPEX transmissions as a function of range and attempt to develop a theoretical framework to explain the observations. This is a very challenging problem but may nevertheless be important. The LOAPEX measurements may give important new insight into this process because measurements were made at many ranges.

# Appendix: Calculation of the acoustic fluctuations strength parameter $\mu$

In this Appendix it is discussed how to compute the acoustic fluctuation strength parameter $\mu$ from CTD (conductivity–temperature–depth) data. We assume that environmental properties of seawater are given in the form of temperature and salinity as functions of pressure. The fractional changes in sound speed caused by internal waves is

$$\frac{\delta c}{c} = \left(\frac{1}{c}\frac{\partial c_\theta}{\partial z}\right)\xi. \tag{A1}$$

In order to express the sound speed fluctuations in terms of water mass quantities and the buoyancy frequency, we replace the gradient in potential sound speed by a gradient in potential density:

$$\frac{\delta c}{c} = \left(\frac{\rho}{c}\frac{\partial c_\theta}{\partial \rho_\theta}\right)\left(\frac{1}{\rho}\frac{\partial \rho_\theta}{\partial z}\right)\xi. \tag{A2}$$

Now the potential density gradient can be expressed in terms of the buoyancy frequency:

$$N^2(z) = -\frac{g}{\rho}\frac{\partial \rho_\theta}{\partial z} \tag{A3}$$

Internal-wave-induced sound speed perturbations $\delta c$ are proportional to internal-wave induced vertical displacements $\xi$ of a fluid parcel,

$$\delta c = \left(\frac{\partial c_\theta}{\partial z}\right)\xi \approx c\left(\frac{\mu}{g}\right)N(z)^2\,\xi. \tag{A4}$$

Here $\partial c_\theta/\partial z$ is the potential sound speed gradient, $N^2(z)$ is the squared buoyancy frequency, $g = 9.8$ m/s$^2$, $c$ is the sound speed, and $\mu$ is a dimensionless acoustic fluctuation strength parameter, which is related to the potential density and potential sound speed as

$$\mu = -\frac{\rho}{c}\frac{\partial c_\theta}{\partial \rho_\theta} \tag{A5}$$

Because variations of $\rho$ and $c$ in the ocean are small these quantities in Eqs. (A4) and (A5) can be replaced by constant average values. Most of the expressions presented below can be found in Ref. [58]. All numerical expressions assume that temperature is given in degrees Celsius, salinity is in parts per thousand and pressure is in decibars. Our objective is to compute $\mu$ as a function of depth. This process can be described in the following steps:

1) Pressure to depth conversion.

Saunders and Fofonoff [62] developed an accurate formula for pressure to depth conversion. The hydrostatic equation is integrated in the form

$$\int_p^z g\,dz = \left(g_0(\phi) + \frac{1}{2}\gamma z\right)z = \int_0^p V\,dp = \int_0^p V(0,35,p)\,dp + \Delta D \tag{A6}$$

where $g_0(\phi)$ is gravity at the ocean surface, a function of latitude $\phi$, $\gamma$ is the mean vertical gradient of gravity, $V$ is specific volume and $\Delta D$ is geopotential anomaly

determined by

$$\Delta D = \int_0^p \delta dp \tag{A7}$$

where

$$\delta = V(T, S, p) - V(0, 35, p) \tag{A8}$$

is specific anomaly.

The equation of state EOS80 [58] has the form

$$V(0, 35, p) = V(0, 35, 0)\left(1 - \frac{p}{k + Ap + Bp^2}\right) \tag{A9}$$

which can be integrated exactly

$$\begin{aligned} \int_0^p V(35, 0, p)\, dp &= V(35, 0, 0)\,[p - \frac{1}{2B}(\ln\left(1 + Ap/k + Bp^2/k\right) + \\ &\quad \frac{A}{R}\ln\frac{(2Bp + A - R)/(A - R)}{(2Bp + A + R)/(A + R)})] \end{aligned} \tag{A10}$$

where $R^2 = A^2 - 4Bk$, $k = 21582.27$, $A = 3.35941$, $B = 5.032 \times 10^{-5}$ and $V(0, 35, 0) = 9.72662 \times 10^{-4}$.

Because the exact formula is not convenient for applications, a least squares polynomial of fourth order in pressure was fitted to a table of values computed from the exact formula:

$$\int_0^p V(35, 0, p)\, dp \approx C_1 p + C_2 p^2 + C_3 p^3 + C_4 p^4 \tag{A11}$$

where $C_1 = 9.72659$, $C_2 = -2.2512 \times 10^{-5}$, $C_3 = 2.279 \times 10^{-10}$, $C_4 = -1.82 \times 10^{-15}$.

The complete formula has the form

$$z = \frac{C_1 p + C_2 p^2 + C_3 p^3 + C_4 p^4}{g(\phi) + \frac{1}{2}\gamma' p} + \frac{\Delta D}{9.8} \tag{A12}$$

with $\gamma' = 2.184 \times 10^{-6}$ m/s$^2$/decibar, and $g(\phi) = 9.780318(1.0 + 5.2788 \times 10^{-3} \sin^2 \phi + 2.36 \times 10^{-5} \sin^4 \phi)$. It is argued in [58] that the geopotential anomaly correction often can be neglected.

2) Sound speed computation.

Sound speed is computed using nine-term equation for sound speed in the ocean introduced by Mackenzie [59]. The result is

$$\begin{aligned} c(T,S,z) &= 1448.96 + 4.591T - 5.304 \times 10^{-2} T^2 + 2.374 \times 10^{-4} T^3 \\ &\quad + 1.340(S-35) + 1.630 \times 10^{-2} z + 1.675 \times 10^{-7} z^2 \\ &\quad - 1.025 \times 10^{-2} T(S-35) - 7.139 \times 10^{-13} T z^3 \end{aligned} \tag{A13}$$

where $T$ is temperature in degrees Celsius, $S$ is salinity in parts per thousand, and $z$ is depth in meters increasing downwards with $z = 0$ at the ocean surface.

3) Secant bulk modulus computation.

The secant bulk modulus $K$ of seawater is given by [63]

$$K(T,S,p) = K(T,S,0) + Ap + Bp^2, \tag{A14}$$

where

$$K(T,S,0) = K_w + \left(f_0 + f_1 T + f_2 T^2 + f_3 T^3\right) S + \left(g_0 + g_1 T + g_2 T^2\right) S^{3/2} \quad \text{(A15)}$$

with $f_0 = 54.6746$, $f_1 = -0.603459$, $f_2 = 1.09987 \times 10^{-2}$, $f_3 = -6.1670 \times 10^{-5}$, $g_0 = 7.944 \times 10^{-2}$, $g_1 = 1.6483 \times 10^{-2}$, $g_2 = -5.3009 \times 10^{-4}$.

$A = A_w + (i_0 + i_1 T + i_2 T^2) S + j_0 S^{3/2}$, where $i_0 = 2.2838 \times 10^{-3}$, $i_1 = -1.0981 \times 10^{-5}$, $i_2 = -1.6078 \times 10^{-6}$, $j_0 = 1.91075 \times 10^{-4}$.

$B = B_w + (m_0 + m_1 T + m_2 T^2) S$, where $m_0 = -9.9348 \times 10^{-7}$, $m_1 = 2.0816 \times 10^{-8}$, $m_2 = 9.1697 \times 10^{-10}$.

The pure water terms of the secant bulk modulus are given by

$K_w = e_0 + e_1 T + e_2 T^2 + e_3 T^3 + e_4 T^4$, where $e_0 = 19652.21$, $e_1 = 148.4206$, $e_2 = -2.327105$, $e_3 = 1.360477 \times 10^{-2}$, $e_4 = -5.155288 \times 10^{-5}$.

$A_w = h_0 + h_1 T + h_2 T^2 + h_3 T^3$, where $h_0 = 3.239908$, $h_1 = 1.43713 \times 10^{-3}$, $h_2 = 1.16092 \times 10^{-4}$, $h_3 = -5.77905 \times 10^{-7}$.

$B_w = k_0 + k_1 T + k_2 T^2$, $k_0 = 8.50935$, $k_1 = -6.12293 \times 10^{-6}$, $k_2 = 5.2787 \times 10^{-8}$.

4) Density of seawater computation [63].

The density of seawater as a function or temperature, salinity and pressure can be computed using the following expression:

$$\rho(T,S,p) = \rho(T,S,0) / (1 - p/K(T,S,p)), \quad \text{(A16)}$$

where

$$\rho\left(T,S,0\right)=\rho_w+\left(b_0+b_1T+b_2T^2+b_3T^3+b_4T^4\right)S+\left(c_0+c_1T+c_2T^2\right)S^{3/2}+d_0S^2 \tag{A17}$$

with $b_0=8.24493\times10^{-1}$, $b_1=-4.0899\times10^{-3}$, $b_2=7.6438\times10^{-5}$, $b_3=-8.2467\times10^{-7}$, $b_4=5.3875\times10^{-9}$, $c_0=-5.72466\times10^{-3}$, $c_1=1.0227\times10^{-4}$, $c_2=-1.6546\times10^{-6}$, $d_0=4.8314\times10^{-4}$.

The density of reference pure water is given by [64]

$$\rho_w=a_0+a_1T+a_2T^2+a_3T^3+a_4T^4+a_5T^5, \tag{A18}$$

where $a_0=999.842594$, $a_1=6.793952\times10^{-2}$, $a_2=-9.095290\times10^{-3}$, $a_3=1.001685\times10^{-4}$, $a_4=-1.120083\times10^{-6}$, $a_5=6.536332\times10^{-9}$.

5) Adiabatic lapse rate computation [65].

The adiabatic lapse rate $\Gamma\left(T,S,p\right)$ (°C/decibar) is defined as the change of temperature per unit pressure for an adiabatic change of pressure of a parcel of seawater. It is assumed that no heat or salt is exchanged with the surroundings so that the pressure change is both adiabatic and isentropic. From thermodynamic considerations, the adiabatic lapse rate $\Gamma$, a function of temperature, salinity and pressure can be expressed as $\Gamma\left(T,S,p\right)=\frac{1}{C_p}T\partial V/\partial T$, where $V$ is specific volume ($V=1/\rho$), $T$ is absolute temperature, $\partial V/\partial T(\mathrm{m}^3/(\mathrm{kg}\ ^\circ\mathrm{C}))$ is thermal expansion and $C_p$ (J/(kg °C)) is the specific heat of seawater at constant pressure. Following [65], the adiabatic

lapse rate can be computed using the following formula:

$$\begin{aligned}\Gamma(T,S,p) &= a_0 + a_1T + a_2T^2 + a_3T^3 + (b_0 + b_1T)(S-35) \\ &\quad + \left(c_0 + c_1T + c_2T^2 + c_3T^3 + (d_0 + d_1T)(S-35)\right)p \\ &\quad + \left(e_0 + e_1T + e_2T^2\right)p^2,\end{aligned} \tag{A19}$$

where $a_0 = 3.5803 \times 10^{-5}$, $a_1 = 8.5258 \times 10^{-6}$, $a_2 = -6.8360 \times 10^{-8}$, $a_3 = 6.6228 \times 10^{-10}$, $b_0 = 1.8932 \times 10^{-6}$, $b_1 = -4.2393 \times 10^{-8}$, $c_0 = 1.8741 \times 10^{-8}$, $c_1 = -6.7795 \times 10^{-10}$, $c_2 = 8.7330 \times 10^{-12}$, $c_3 = -5.4481 \times 10^{-14}$, $d_0 = -1.1351 \times 10^{-10}$, $d_1 = 2.7759 \times 10^{-12}$, $e_0 = -4.6206 \times 10^{-13}$, $e_1 = 1.8676 \times 10^{-14}$, $e_2 = -2.1687 \times 10^{-16}$.

6) Potential temperature computation [66].

Potential temperature is defined as the temperature an element of seawater would have if it were raised adiabatically with no change of salinity to a reference pressure $p_r$ that may be greater or less than the initial pressure $p$. The potential temperature $\Theta$ can be computed from the adiabatic lapse rate $\Gamma$,

$$\Theta(T,S,p,p_r) = T + \int_p^{p_r} \Gamma(T,S,p')\,dp' \tag{A20}$$

by integration along an adiabat. The potential temperature $\Theta(S,T,p,p_r)$ at reference pressure $p_r$ can be computed with sufficient precision using a 4-th order Runge-Kutta integration algorithm [66]. However, it has been shown [58] that to a good approximation the integration step $\Delta p$ can be chosen to be $\Delta p = p_r - p$. Then potential temperature is computed using the following simple formulas: $\Delta\Theta_1 = \Delta p\Gamma(T,S,p)$, $\Theta_1 =$

$T + \frac{1}{2}\Delta\Theta_1$, $\Delta\Theta_2 = \Delta p \Gamma\left(\Theta_1, S, p + \frac{1}{2}\Delta p\right)$, $\Theta_2 = \Theta_1 + \left(1 - 1/\sqrt{2}\right)(\Delta\Theta_2 - q_1)$, $\Delta\Theta_3 = \Delta p \Gamma\left(\Theta_2, S, p + \frac{1}{2}\Delta p\right)$, $\Theta_3 = \Theta_2 + \left(1 + 1/\sqrt{2}\right)(\Delta\Theta_3 - q_2)$, $\Delta\Theta_4 = \Delta p \Gamma\left(\Theta_3, S, p + \Delta p\right)$, $\Theta_4 = \Theta_3 + \frac{1}{6}(\Delta\Theta_4 - 2q_3)$, where $q_1 = \Delta\Theta_1$, $q_2 = \left(2 - \sqrt{2}\right)\Delta\Theta_2 + \left(-2 + 3/\sqrt{2}\right) q_1$, $q_3 = \left(2 + \sqrt{2}\right)\Delta\Theta_3 + \left(-2 - 3/\sqrt{2}\right) q_2$, and

$$\Theta\left(T, S, p, p_r\right) = \Theta_4. \tag{A21}$$

7) Potential density and potential sound speed computation.

Now after potential temperature is computed it is straightforward to compute potential density and potential sound speed of seawater. To compute potential density it is necessary to replace temperature $T$ with the potential temperature $\Theta$ and pressure $p$ with reference pressure $p_r$ in Eq. (A16) and the equation for potential density is

$$\rho_\theta\left(\Theta, S, p_r\right) = \rho\left(\Theta, S, p_r\right). \tag{A22}$$

Similarly, the equation for potential sound speed is

$$c_\theta\left(\Theta, S, p_r\right) = c\left(\Theta, S, z_r\right). \tag{A23}$$

It is convenient to choose $p_r = 0$ and $z_r = 0$ that corresponds to the ocean surface level.

After all these calculations have been done, the acoustic fluctuations strength parameter $\mu$ is computed by substituting potential density and potential sound speed given by Eqs. (A22) and (A23) into Eq. (A5).

# References


[1] L. M. Brekhovskikh. *Waves in layered media*. Academic Press, New York, 1960.

[2] C. L. Pekeris. Theory of propagation of explosive sound in shallow water. *Geol. Soc. Am. Mem.*, 27, 1948.

[3] F. B. Jensen and M. C. Ferla. SNAP: The SACLANTCEN normal-mode acoustic propagation model. Technical report, SACLANT Undersea Research Center, La Spezia, Italy, 1979.

[4] M. B. Porter. The KRAKEN normal mode program. Technical report, SACLANT Undersea Research Centre, La Spezia, Italy, 1979.

[5] E. K. Westwood, C. T. Tindle, and N. R. Chapman. A normal mode model for acousto-elastic ocean environment. *J. Acoust. Soc. Am.*, 100:3631–3645, 1996.

[6] A. D. Pierce. Extension of the method of normal modes to sound propagation in an almost-stratified medium. *J. Acoust. Soc. Am.*, 37:19–27, 1965.

[7] S. R. Rutherford and K. E. Hawker. Consistent coupled mode theory of sound propagation for a class of nonseparable problems. *J. Acoust. Soc. Am.*, 70:554–564, 1981.

[8] I. J. Thompson. Mixing of normal modes in a range-dependent model ocean. *J. Acoust. Soc. Am.*, 69:1280–1289, 1981.

[9] R. B. Evans. A coupled mode solution for acoustic propagation in a waveguide with stepwise depth variations of a penetrable bottom. *J. Acoust. Soc. Am.*, 74:188–195, 1983.

[10] L. B. Dozier and F. D. Tappert. Statistics of normal mode amplitudes in a random ocean. i. theory. *J. Acoust. Soc. Am.*, 63:353–365, 1978.

[11] J. A. Mercer, R. K. Andrew, B. M. Howe, and J. A. Colosi. Cruise report: Long-range ocean acoustic propagation experiment (LOAPEX). Technical report, Applied Physics Laboratory, University of Washington, 2005.

[12] K. E. Wage, A. B. Baggeroer, and J. C. Preisig. Modal analysis of broadband acoustic receptions at 3515-km range in the North Pacific using short-time Fourier techniques. *J. Acoust. Soc. Am.*, 113:801–817, 2003.

[13] K. E. Wage, M. A. Dzieciuch, P. F. Worcester, B. M. Howe, and J. A. Mercer. Mode coherence at megameter ranges in the North Pacific Ocean. *J. Acoust. Soc. Am.*, 117:1565–1581, 2005.

[14] J. A. Colosi and S. M. Flatté. Mode coupling by internal waves for multimegameter acoustic propagation in the ocean. *J. Acoust. Soc. Am.*, 100:3607–3620, 1996.

[15] L. A. Chernov. *Wave propagation in a random medium.* McGraw-Hill Book Company, New York, 1960.

[16] V. I. Tatarskii. *The effects of the turbulent atmosphere on wave propagation.* Israel Program for Scientific Translation, Jerusalem, 1971.

[17] I. Tolstoy and C. S. Clay. *Ocean acoustics. Theory and experiment in underwater sound.* McGraw-Hill Book Company, New York, 1966.

[18] S. Flatté, R. Dashen, W. Munk, K. Watson, and F. Zachariasen. *Sound Transmission Through a Fluctuating Ocean.* Mechanics and Applied Mathematics. Cambridge University, 1979.

[19] C. Garrett and W. H. Munk. Space-time scales of internal waves. *Geophys. Fluid Dyn.*, 2:225–264, 1972.

[20] R. Leung and H. A. DeFerrari. $\phi$ and $\lambda$ computations for real and canonical ocean. *J. Acoust. Soc. Am.*, 67:169–176, 1980.

[21] J. A. Colosi, E. K. Scheer, S. M. Flatté, B. D. Cornuelle, M. A. Dzieciuch, W. H. Munk, P. F. Worcester, B. M. Howe, J. A. Mercer, R. C. Spindel, K. Metzger, and T. Birdsall. Comparison of measured and predicted acoustic fluctuations for a 3250-km propagation experiment in the eastern North Pacific Ocean. *J. Acoust. Soc. Am.*, 105:3202–3218, 1999.

[22] A. L. Virovlyansky, A. Yu. Kazarova, and L. Ya. Lyubavin. Ray-based description of normal mode amplitudes in a range-dependent waveguide. *Wave motion*, 42:317–334, 2005.

[23] D. M. Milder. Ray and wave invariants for SOFAR channel propagation. *J. Acoust. Soc. Am.*, 46:1259–1263, 1969.

[24] M. G. Brown, J. A. Colosi, S. Tomsovic, A. L. Virovlyansky, M. Wolfson, and G. M. Zaslavsky. Ray dynamics in long-range deep ocean sound propagation. *J. Acoust. Soc. Am.*, 113:2533–2547, 2003.

[25] F. J. Beron-Vera and M. G. Brown. Ray stability in weakly range-dependent sound channels. *J. Acoust. Soc. Am.*, 114:123–130, 2003.

[26] F. J. Beron-Vera and M. G. Brown. Travel time stability in weakly range-dependent sound channels. *J. Acoust. Soc. Am.*, 115:1,068–1,077, 2004.

[27] S. D. Chuprov. Interference structure of a sound field in a layered ocean. *Ocean Acoustics, Current State*, pages 71–91, 1982.

[28] G. A. Grachev. Theory of acoustic field invariants in layered waveguides. *Acoust. Phys.*, 39:33–35, 1993.

[29] M. G. Brown, F. J. Beron-Vera, I. Rypina, and I. A. Udovydchenkov. Rays, modes, wavefield structure, and wavefield stability. *J. Acoust. Soc. Am.*, 117:1607–1610, 2005.

[30] A. L. Virovlyansky. Ray travel times at long range in acoustic waveguides. *J. Acoust. Soc. Am.*, 113:2523–2532, 2003.

[31] D. S. Ahluwalia and J. B. Keller. Exact and asymptotic representations of the sound field in a stratified ocean. In *Wave propagaion and underwater acoustics*. Springer, 1977.

[32] A. L. Virovlyansky, V. V. Kurin, N. V. Pronchatov-Rubtsov, and S. I. Simdyankin. Fresnel zones for modes. *J. Acoust. Soc. Am.*, 101:163–173, 1997.

[33] M. Born and E. Wolf. *Principles of optics*. Pergamon, Oxford, 1968.

[34] M. G. Brown, J. Viechnicki, and F. D. Tappert. On the measurement of modal group time delays in the deep ocean. *J. Acoust. Soc. Am.*, 100:2093–2102, 1996.

[35] W. H. Munk and C. Wunsch. Ocean acoustic tomography: Rays and modes. *Rev. Geophys. Space Phys.*, 21:777–793, 1983.

[36] W. H. Munk. Sound channel in an exponentially stratified ocean with application to SOFAR. *J. Acoust. Soc. Am.*, 55:220–226, 1974.

[37] R. A. Koch, C. Penland, P. J. Vidmar, and K. E. Hawker. On the calculation of normal mode group velocity and attenuation. *J. Acoust. Soc. Am.*, 73:820–825, 1983.

[38] D. M. F. Chapman and D. D. Ellis. The group velocity of normal modes. *J. Acoust. Soc. Am.*, 74:973–979, 1983.

[39] I. I. Rypina, I. A. Udovydchenkov, and M. G. Brown. A transformation of the environment eliminates parabolic equation phase errors. *J. Acoust. Soc. Am.*, 120:1295–1304, 2006.

[40] H. K. Brock, R. N. Buchal, and C. W. Spofford. Modifying the sound-speed profile to improve the accuracy of the parabolic-equation technique. *J. Acoust. Soc. Am.*, 82:543–552, 1977.

[41] E. L. Murphy and J. A. Davis. Modified ray theory for bounded media. *J. Acoust. Soc. Am.*, 56:1747–1760, 1974.

[42] A. L. Virovlyansky, A. Yu. Kazarova, and L. Ya. Lyubavin. Statistical description of chaotic rays in a deep water acoustic waveguide. *J. Acoust. Soc. Am.*, 121:2542–2552, 2007.

[43] A. L. Virovlyansky. *Ray theory of long-range sound propagation in the ocean*. Institute of Applied Physics, Nizhny Novgorod, 2006.

[44] A. L. Virovlyansky, A. Yu. Kazarova, and L. Ya. Lyubavin. Modal structure of the field under conditions of wave chaos. In *Ocean Acoustics. Proceedings of the 11-th L. M. Brekhovskikh's conference. Moscow, CEOS*, pages 40–43, 2006.

[45] A. L. Virovlyansky. Statistical description of ray chaos in an underwater acoustic waveguide. *Acoust. Phys.*, 51:71–80, 2005.

[46] F. Beichelt. *Stochastic Processes in Science, Engineering and Finance*. Chapman & Hall/CRC, 2006.

[47] J. A. Colosi and M. G. Brown. Efficient numerical simulation of stochastic internal-wave-induced sound speed perturbation fields. *J. Acoust. Soc. Am.*, 103:2232–2235, 1998.

[48] I. I. Rypina and M. G. Brown. On the width of a ray. *J. Acoust. Soc. Am.*, 122:1440–1448, 2007.

[49] S. W. Golomb. *Shift-Register Sequences*. Holden-Day, San Francisco, 1967.

[50] J. A. Mercer and B.M. Howe. Long-range ocean acoustic propagation experiment LOAPEX. Technical report, Applied Physics Laboratory, University of Washington, 2004.

[51] W. H. Munk and F. Zachariasen. Sound propagation through a fluctuating stratified ocean: Theory and observation. *J. Acoust. Soc. Am.*, 59:818–838, 1976.

[52] S. M. Flatté and F. D. Tappert. Calculation of the effects of internal waves on oceanic sound transmission. *J. Acoust. Soc. Am.*, 58:1151–1159, 1975.

[53] K. J. Noble and S. M. Flatté. Predicting acoustic effects of internal waves from the basic climatology of the world ocean. *J. Acoust. Soc. Am.*, 107:747–757, 2000.

[54] C. Garrett and W. H. Munk. Space-time scales of internal waves: A progress report. *J. Geophys. Res.*, 80:291–298, 1975.

[55] C. Garrett and W. H. Munk. Internal waves in the ocean. *Annu. Rev. Fluid Mech.*, 11:339–369, 1979.

[56] J. A. Colosi, S. M. Flatté, and C. Bracher. Internal-wave effects on 1000-km oceanic acoustic pulse propagation: Simulation and comparison with experiment. *J. Acoust. Soc. Am.*, 96:452–468, 1994.

[57] M. A. Wolfson and J. L. Spiesberger. Full wave simulation of the forward scattering of sound in a structured ocean: A comparison with observations. *J. Acoust. Soc. Am.*, 106:1293–1306, 1999.

[58] N. Fofonoff and R. C. Millard, J. Algorithms for computation of fundamental properties of seawater. Technical report, UNESCO technical papers in Marine Science, 1983.

[59] K. V. Mackenzie. Nine-term equation for sound speed in the oceans. *J. Acoust. Soc. Am.*, 70:807–812, 1981.

[60] F. J. Beron-Vera and M. G. Brown. Underwater acoustic beam dynamics. in preparation. 2007.

[61] C.-S. Chiu, C. W. Miller, and J. F. Lynch. Optimal modal beamforming of bandpass signals using an undersized sparse vertical hydrophone array: theory and a shallow-water experiment. *IEEE Journal of Oceanic Engineering*, 22:522–533, 1997.

[62] P. M. Saunders and N. P. Fofonoff. Conversion of pressure to depth in the ocean. *Deep-Sea Res.*, 23:109–111, 1976.

[63] F. J. Millero and A. Poisson. Summary of data treatment for the UNESCO one atmosphere equation of state for seawater. *Deep-Sea Res.*, 28A:625–629, 1981.

[64] H. Craig. Standard for reporting concentrations of Deuterium and Oxygen-18 in natural waters. *Science*, 133:1833–1934, 1961.

[65] H. L. Bryden. New polynomials for thermal expansion, adiabatic temperature gradient and potential temperature of sea water. *Deep-Sea Res.*, 20:401–408, 1973.

[66] N. P. Fofonoff. Computation of potential temperature of seawater for an arbitrary reference pressure. *Deep-Sea Res.*, 24:489–491, 1977.